On the Control of a Seawater-Hydraulic Wind Farm with the Delft Offshore Turbine

S.C.M. van Didden

Master of Science Thesis

TU Delft Delft University of Technology

Delft Center for Systems and Control

On the Control of a Seawater-Hydraulic Wind Farm with the Delft Offshore Turbine

Master of Science Thesis

For the degree of Master of Science in Systems and Control at Delft University of Technology

S.C.M. van Didden

April 30, 2019

Faculty of Mechanical, Maritime and Materials Engineering (3mE) · Delft University of Technology

The work in this thesis was supported by Delft Offshore Turbine B.V. Their cooperation is hereby gratefully acknowledged.

Delft University of Technology
Department of
Delft Center for Systems and Control (dcsc)

The undersigned hereby certify that they have read and recommend to the Faculty of Mechanical, Maritime and Materials Engineering (3mE) for acceptance a thesis entitled

On the Control of a Seawater-Hydraulic Wind Farm with the Delft Offshore Turbine

by

S.C.M. van Didden

in partial fulfillment of the requirements for the degree of

Master of Science Systems and Control

Dated: April 30, 2019

Supervisor(s):

prof.dr.ir. J.W. van Wingerden

ir. S.P. Mulders

Reader(s):

dr.ir. E.M. Lourens

ir. R. Jorritsma

Abstract

Offshore wind energy is a promising prospect to meet the ever-growing demand for energy. Its reputation is, however, sullied by high costs not yet competitive with conventional energy resources. The Delft Offshore Turbine (DOT) attempts to radically reduce the Levelized Cost of Energy (LCOE) of offshore wind by utilising a seawater-hydrostatic transmission from individual wind turbines to a central power station, where power is generated collectively.

Recent theoretical research on the DOT employed variable displacement pumps in the wind turbines interconnected through a collective pipeline. A variable displacement pump does not yet commercially exist and leaves the implementation of a fixed-displacement pump more viable in the near future. Recent practical research implemented a fixed-displacement pump with an individual pipeline. To benefit from the economy of scale however, a collective pipeline is preferred.

The DOT wind farm considered in this thesis incorporates fixed-displacement pumps interconnected through a collective pipeline. The difficulty herein arises from the combination of an equal hydraulic torque but varying aerodynamic torque throughout the wind farm. The combined effect results in the inability to control individual rotor speeds, which inevitably leads to suboptimal individual rotor efficiency.

This research explores a novel control strategy that obtains the best suboptimal performance when the wind turbines are controlled through a collective pressure. First, the static maximum power production of such a wind farm is determined, which then forms the basis of the new control strategy. Thereafter, the subsystem controllers that facilitate the implementation of the control strategy are designed and verified in a numerical model, including a stability analysis.

A numerical simulation compares the DOT wind farm and the derived control strategy with a conventional wind farm employing NREL 5-MW reference turbines in dynamic wind conditions. The power production of the DOT wind farm fluctuates around 70% of the conventional wind farm, which is consistent with the derived maximum power production. To reduce the LCOE, the DOT wind farm has to provide at least an equivalent cost reduction over the lifetime of the wind farm.

A lab-scale test set-up is built to reveal discrepancies between the derived model and the physical world. A partial validation is obtained through the design and tuning of two subsystem controllers of the set-up: a feed pressure and Pelton controller. Most notably, the data-driven optimization of the Pelton controller led to the discovery of a poor mechanical efficiency in the Pelton turbine compared with its theoretical conception. The implementation of Extremum Seeking Control (ESC) increased the power production from -27W to 473W by correcting the control parameter.

Table of Contents

Acknowledgements

First and foremost, I would like to thank my supervisor Sebastiaan Mulders. His dedication and critical attitude have had a significant influence on this work. Furthermore, my thanks go out to Jan-Willem van Wingerden for taking the time for intermediate feedback sessions that have helped me on my way.

Also, I would like to thank the department of DCSC for supporting the foundation of the study association Kalman. Thanks to all Kalman board members, who have worked with me towards business events, social activities or the improvement of the study program of Systems & Control.

I would like to thank DOT for offering this graduation project and Reinder for his supervision. Moreover, my thanks to all employees of DOT and De Oude Bibliotheek, who in one way or another contributed to the work in this thesis. Particularly, the tremendous help of Deborah, Roberto and Alejo in the final phases of the development of the lab-scale test set-up are greatly appreciated.

Furthermore, my gratitude to Jorg, Rene and Peter from Elsto Drives & Controls for their expertise and guidance during the design and fabrication of the electrical cabinet. Thanks to Sjaak from Fluiconnecto, who helped greatly with the hydraulic connections and lines.

Special thanks go out to my fellow graduate researcher, Roy. His companionship in pursuing the design, procurement and installation of the lab-scale test set-up has been invaluable.

My gratitude goes out to all friends that have been a part of my journey in Delft. Without them, I would have graduated years earlier. Although there are too many to name, I am grateful for the privilege of sharing those years with you.

Lastly, I want to thank my parents and brother. A wise man once said 'nothing's better left unsaid', yet this is: your unconditional love and support mean everything to me.

Delft, University of Technology — S.C.M. van Didden
April 30, 2019

Chapter 1

Introduction

The world demand for energy has been ever-growing over the last decades. The finite extraction of fossil fuels and rising social awareness for global warming - underlined by the *Paris Climate Agreement* in 2015 - have led to the rapid development of renewable energy sources to meet this energy demand [1][2]. A promising prospect as a renewable energy source is found in wind energy. With the ambition to accommodate 24% of Europe's energy demand with wind energy by 2030, the European Union accentuates the enormous potential of wind energy [3]. Due to the scarcity of empty land suitable for onshore wind turbines, this directly translates to a vast appeal for offshore wind farms with power ratings on gigawatt scale, as derived from the exponential growth of the cumulative installed offshore capacity in Figure 1-1.

Regardless of the vast potential, the Levelized Cost of Energy (LCOE) has not yet proven to be competitive to that of conventional energy resources. Even though cost reduction has

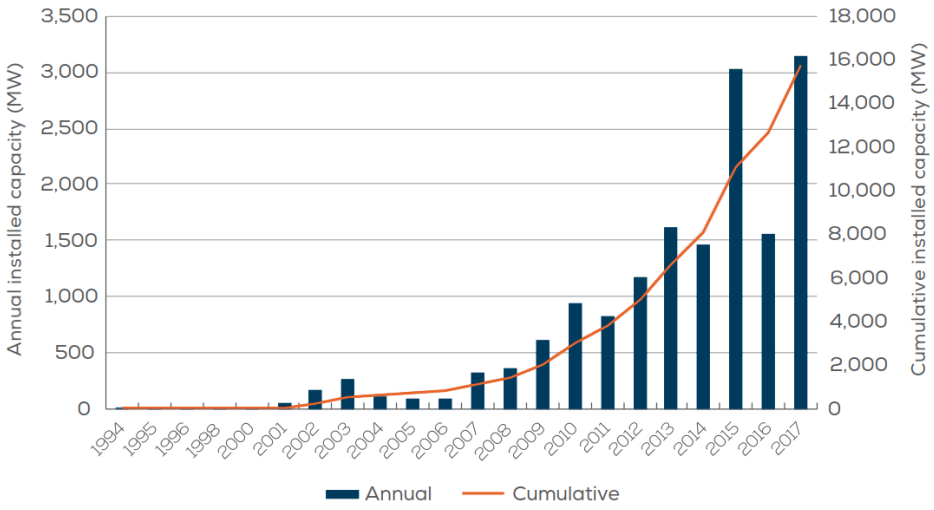

Figure 1-1: The exponential grow in cumulative installed capacity in Europe indicates the vast appeal for offshore wind energy [2].

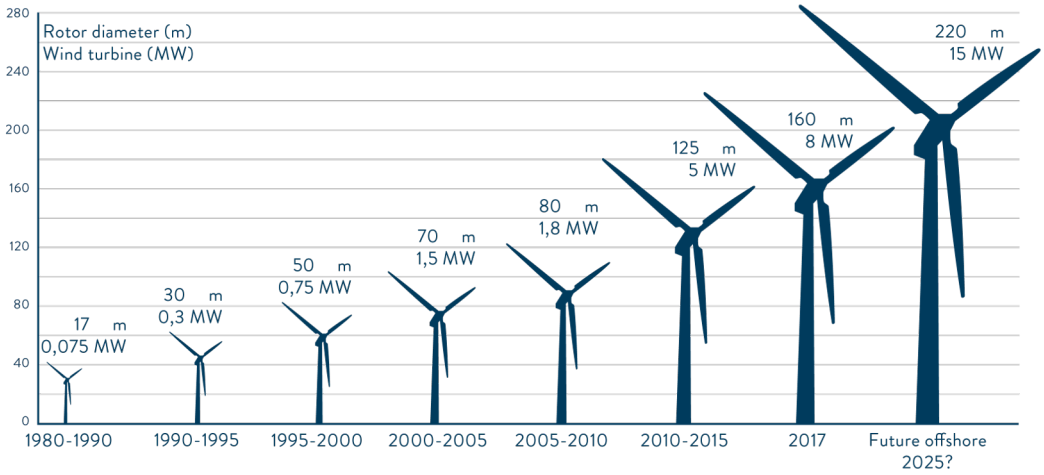

Figure 1-2: Both rotor diameter and power rating of individual wind turbines increase in an effort to decrease the LCOE of offshore wind energy [7].

been an influential trend in the wind industry since the late 1970s, offshore wind farms have not been cost-effective without subsidies [4]. In 2014, a further reduction of 40% of the total costs has been determined to adequately secure the future of offshore wind [5].

A common method to reduce the LCOE has been to upscale the nominal power rating of individual wind turbines as shown in Figure 1-2 [6][7]. Efforts to decrease the LCOE of offshore wind farms have not been in vain, resulting in the first tenders for subsidy-free offshore wind farms, which are scheduled to be build in 2022 [8]. Even so, further reduction of costs is imperative to render offshore wind farms economically feasible and propel the future of offshore wind energy.

A significant reduction can still be found in maintenance, accounting for 15-20% of the total costs, as the offshore wind industry struggles with the sheer number of maintenance-critical components in the nacelle [9][10][11]. The main cause of early-fatigue damage is often traced back to the direct coupling of the drivetrain to the rotor, imposing the subjection to dynamical loads induced by turbulent wind fluctuations. In particular the gearbox, often a high-weight component, has been identified as the primary contributor to maintenance costs [12].

An alternative is presented by hydraulic systems, famed for their effectiveness under harsh conditions in many industries. Even in the wind industry hydraulics are favored for auxiliary systems [4][5][13]. Back in the eighties, the benefits were already pointed out: the improvement of torsional dynamics by added damping and absence of possible axis-misalignment can substantially increase the expected lifetime [14][15]. Furthermore, the high power density of hydraulics facilitates a weight reduction of the head mass, reducing structural costs of the wind turbine [16][17].

1-1 Related research

The attractiveness of hydraulic transmissions in the wind industry has led to several concepts, of which a selection is illustrated in Figure 1-3 [5][18]. Virtually all of these concepts pursue the utilization of a variable ratio transmission to facilitate a synchronous generator and

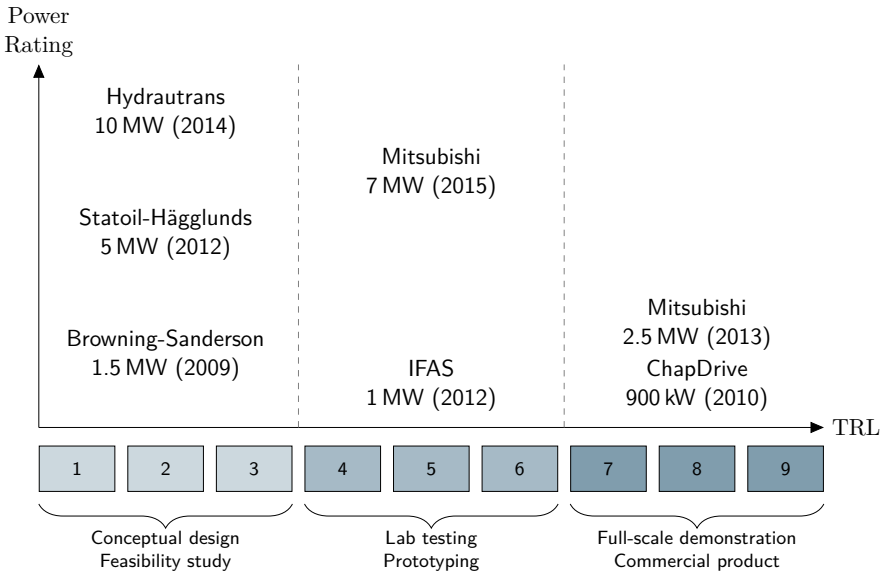

Figure 1-3: The development of hydraulic transmissions in the wind industry mapped based on their power rating and TRL.

consequentially avoid power electronics. The concepts of Statoil-Hägglunds and IFAS obtain this by modular activation of components, allowing discrete switching between fixed ratios [19][20]. Rather than activating entire components, the concept of (Artemis-)Mitsubishi can digitally activate pistons in the pump [21]. In this manner, the pump varies its volumetric displacement step-wise. The concepts of ChapDrive, Browning-Sanderson, and Hydrautrans exploit the same principle as Artemis-Mitsubishi, but rather implement components with the ability to vary the volumetric displacement continuously [22][23][24].

Aside from the desire for a synchronous generator, several other trends are derived from Figure 1-3. Firstly, the desire for an increasing nominal power rating is seen and corresponds to an ambition to compete with conventional concepts. Despite this ambition, the nominal power rating decreases for higher TRL for practical reasons. Still, a trend over the years is the enhanced TRL of the concepts. While the majority of the research was committed to the conceptual phase and only a few concepts have been proven effective with lab tests or a demonstration, it indicates the viability of hydraulic transmissions in wind turbines.

1-2 The Delft Offshore Turbine

A mindset throughout the wind industry can be found to generate electricity in individual wind turbines [6][25]. This paradigm is also present in all the concepts above. While this distributed form of electricity generation may benefit the independence of the wind turbine, it excludes the (economic) benefits of scalability. The use of a hydraulic transmission introduces new possibilities by allowing to combine the fluid power of multiple wind turbines and enable collective power generation as illustrated in Figure 1-4.

Hydraulic transmissions with conventional hydraulic fluids require a closed-loop system and thus the availability of a significant volume of mineral oil to facilitate a power transfer of

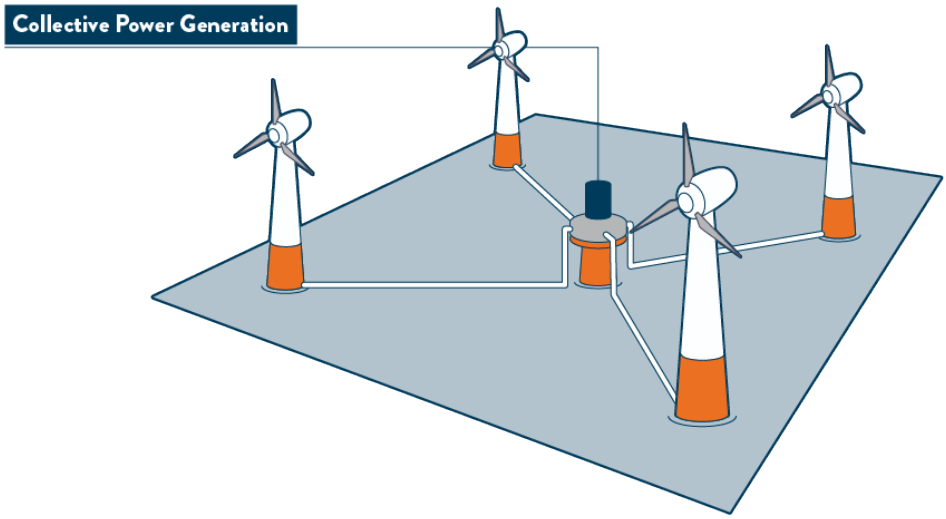

Figure 1-4: The DOT allows to combine hydraulic power of the wind turbines through a pipeline network to a Pelton turbine for centralized electricity generation.

several megawatts [4][5]. Moreover, it imminently introduces exposure to risks of contamination spills and fire hazards. The DOT takes a distinctively different approach by employing a vast available offshore resource, seawater, and a Pelton turbine, to generate electricity, in an open-loop configuration. Using seawater as medium additionally enables to reap the benefits of Ocean Thermal Energy Conversion (OTEC) and Reverse Osmosis (RO) [26][27].

A full-scale test, the DOT500, was erected at the Maasvlakte II in 2016 and the Princess Amalia Wind Farm in 2018, as shown in Figure 1-5a. A control strategy using only the rotor speed as input was derived and demonstrated the ability to obtain optimal wind capture of the wind turbine by controlling the rotor speed. The optimal rotor speed was in turn obtained

(a) **(b)**

Figure 1-5: The full-scale test DOT500 showed ability to control the rotor speed and obtain optimal tip-speed ratio through spear valve control. Pictures of the DOT500 at (a) the Maasvlakte II, The Netherlands, and (b) the Princess Amalia wind farm in the North Sea.

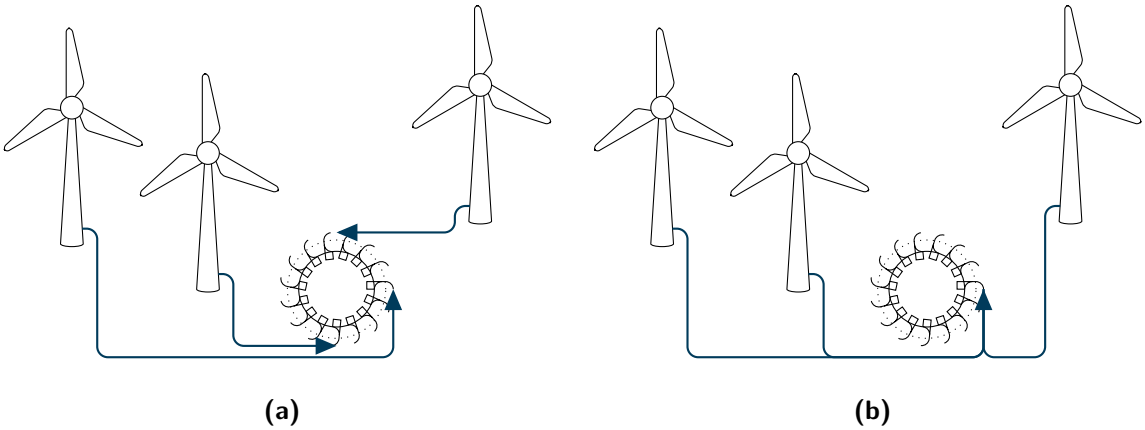

Figure 1-6: An illustration of the possible interconnection between wind turbines of a seawater-hydraulic wind farm with a fixed-displacement pump in the nacelle of the wind turbines. The hydraulic power from the wind turbines feeds to the Pelton turbine trough (a) individual pipelines or (b) a collective pipeline.

through the hydraulic pressure by controlling the spear position at the Pelton turbine [28]. A favorable degree of damping was found as a result of a combination of rotor inertia and fluid capacitance [4][16]. Furthermore, the reduced number of components and high power density of hydraulics prognosticate a top head mass reduction of 20% to 40% [4]. Furthermore, the use of pipelines and a centrally-located generator reduce the costs of electrical infrastructure and copper usage [29][30]. Altogether, the DOT is believed to reduce installation, structural and maintenance costs [16][31].

With a functional wind turbine at hand, the expansion to an array of multiple turbines is imperative in the development towards the commercial deployment of the DOT-concept. The interconnection between wind turbines renders two possible configurations, sketched in Figure 1-6: individual or collective pipeline. To benefit from the economy of scale, the configuration with a collective pipeline is of particular interest.

A simulation of a seawater-hydraulic wind farm connected through a collective pipeline has been performed with variable displacement pumps [32]. A variable displacement pump is however not yet available for seawater at competitive power ratings and leaves the implementation of a fixed-displacement pump more viable in the near future. To date, the incorporation of fixed-displacement pumps and a collective pipeline in a seawater-hydraulic wind farm remains an uncharted area of research.

1-3 Problem statement & research goal

The use of a fixed-displacement pump imposes a limitation on the control strategy as the hydraulic torque applied to the rotor is dictated by the pressure in the pipeline. Considering a collective pipeline, the main ramification arises when varying wind speeds are encountered across the wind turbines, be it by wake effects or the wind field itself. This translates to a problem where all wind turbines have varying aerodynamic torque available but share a collective hydraulic torque, resulting in the potential acceleration of individual wind turbines.

Pitch control can forcefully reduce the rotor efficiency to maintain a collective aerodynamic torque [33]. A preferred alternative is to depreciate the wind capture by allowing wind turbines to accelerate and thereby increase the tip-speed ratio. Although the rotor efficiency decreases for the increased tip-speed ratio, the generated hydraulic power still increases as a result of higher flow. By either means, suboptimal wind capture throughout the wind farm is imminent when employing a collective pipeline.

Altogether, this formulates the following research question:

> *What is the optimal control strategy for a seawater-hydraulic wind farm with fixed-displacement pumps interconnected through a collective hydraulic network to a centralized power station?*

For convenience, the wind farm specified above is further referenced to as the DOT wind farm. To answer the research question, several concise sub-goals are stated:

1. Define the optimal performance of the DOT wind farm and derive a control strategy;
2. Develop a numerical model to reflect the characteristics and dynamics of the DOT wind farm and to verify the derived control strategy;
3. Make a comparison of performance between the DOT wind farm and a wind farm employing the NREL 5-MW reference turbine.
4. Develop a lab-scale test set-up and perform hardware-in-the-loop simulations to indicate possible discrepancies between the derived model and the physical world. In doing so, it is able to validate the control strategy in a practical and dynamic environment;

1-4 Report structure

With the aforementioned objective in mind, this thesis is organized in eight chapters as shown in Figure 1-7. The first three chapters are meant to give sufficient background into seawater-hydraulic wind farms. Chapter 2 starts with a brief description of the most recent research, the state-of-the-art of the DOT, with the focus on implemented control techniques. Chapter 3 lays out the governing principles of the systems in the DOT wind farm. Chapter 4 describes the derivation of an initial control strategy for the DOT wind farm based on the knowledge of preceding chapters.

Chapter 5 explains how the theoretical, full-scale components are designed and approached in a numerical model. Furthermore, the subsystem controllers that facilitate the validation of the control strategy are derived. Chapter 6 describes the numerical simulations that are performed on the numerical model and discusses the simulation results.

Chapter 7 elaborates on the lab-scale test set-up and its physical components. Moreover, several subsystem controllers are derived and optimized.

Chapter 8 completes this thesis with a conclusion on the research question and a brief outlook with recommendations for the future of the DOT.

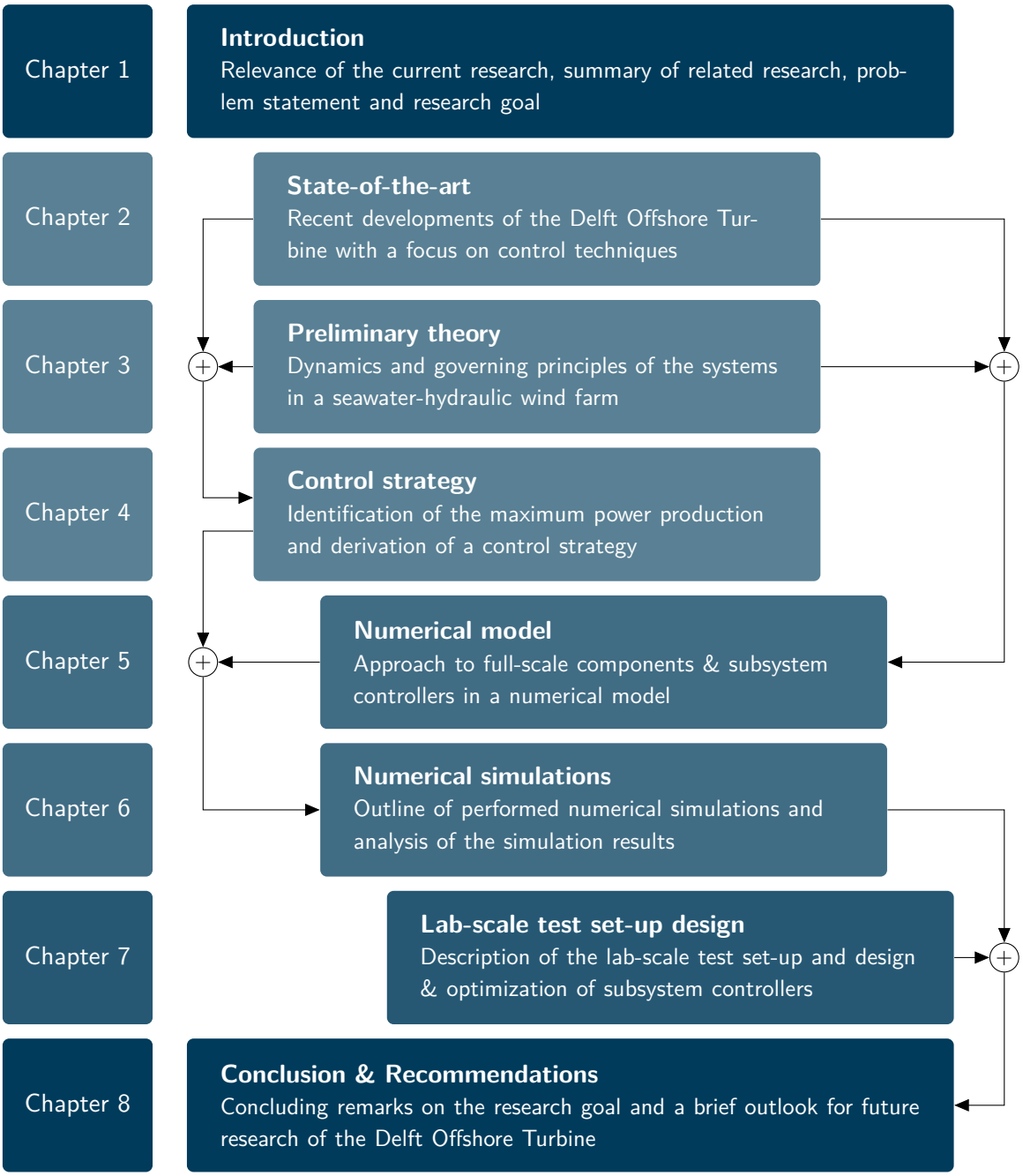

Figure 1-7: An outline of this thesis

Chapter 2

State of the Art

As mentioned in Chapter 1, the Technology Readiness Level (TRL) of hydraulic transmissions in the wind industry has progressed over the years. This chapter aims to elaborate on the latest developments related to the Delft Offshore Turbine (DOT). In particular, the control strategies and methods are outlined and evaluated.

This chapter consists of three brief sections. Section 2-1 focuses on the most recent practical research on the DOT500 as shown in Figure 2-1. Section 2-2 elaborates on recent theoretical research considering a wind farm simulation with variable displacement pumps. Section 2-3 concludes this chapter and outlines the useful elements of previous work for application in the current research.

Figure 2-1: Aerial view of the DOT500 on the Maasvlakte II, The Netherlands. The DOT500 proved the ability to control the rotor speed of the wind turbine through the line pressure [28].

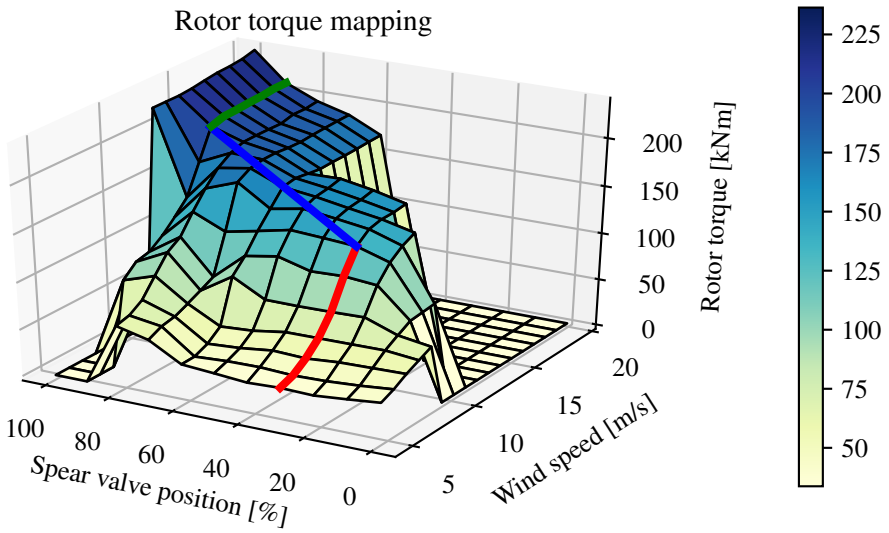

Figure 2-2: The control strategy of the DOT500 [28]. The red and blue lines indicate below-rated passive and active spear control respectively. The green line shows above-rated pitch control with passive spear control.

2-1 A prototype hydraulic wind turbine: the DOT500

The DOT500 was a prototype hydraulic wind turbine, erected at the Maasvlakte II, The Netherlands, in 2016 as shown in Figure 2-1 [28]. The DOT500 included an intermediate oil loop between the rotor and the water pump to facilitate implementation with off-the-shelf components.

A control strategy was derived using the rotor torque mapping shown in Figure 2-2 [28]. Ultimately, the control strategy was able to track the optimal system torque, similar to the strategy of conventional wind turbines, based on the rotor speed. For the lower wind speeds in below-rated conditions[1], it was shown that the flow resulting from the rotor speed systematically increased the line pressure. As illustrated by the red line in Figure 2-2, initially no spear actuation is required to follow the rotor torque envelope, referred to as passive spear control [4].

As the wind speed increases and the rotor speed approaches its rated value, the spear position is actively controlled. This strategy is comparable to conventional torque control in the transition region [6][28]. Rather than the generator torque, the spear position is actively manipulated to regulate the rotor speed. This strategy is represented by the blue line in Figure 2-2, referred to as active spear control.

In above-rated conditions, both the pressure and angular speed have reached their maximum. The spear position is held constant to provide the rated system torque, while the angular speed is maintained through conventional pitch control [34]. This region is indicated by the green line in Figure 2-2.

[1]Rated conditions refer to the rated wind speed, or equivalent rated wind power, of the wind turbine. Below- and above-rated refer to conditions below or above this value respectively.

Since the Pelton turbine is physically decoupled from the rest of the system, its control is done irrespective of the above-defined control strategy. The rotational Pelton wheel speed is controlled to provide optimal capture of the hydro-kinetic power. This is implemented through an analytical relation between the line pressure and the desired Pelton runner wheel speed [35].

2-2 Wind farm simulations with variable displacement pumps

A model and analysis of a seawater-hydraulic wind farm employing variable displacement pumps are made in 2017 [5][32]. A variable displacement pump is a positive displacement pump in which the volumetric displacement can be controlled. As such, this pump is able to operate at a wide range of given differential pressures across the pump by accordingly varying the volumetric displacement. Consequently, the wind turbine can operate irrespective of the available shaft torque. Due to this independence, the control design is decoupled into four control systems [5][29][36]:

- **Aerodynamic torque control**
  This system controls the collective pitch of the rotor blades as described by the NREL 5-MW reference wind turbine [34]. It uses a constant optimal fine-pitch angle for below-rated operation and uses collective pitch control for limiting loads and power output for above-rated conditions. The rotor speed is used as input for the system, while the measured pitch is used for gain-scheduling the pitch controller.

- **Hydraulic torque control**
  A hydraulic torque controller derived to obtain a certain system torque on the low-speed rotor shaft, by controlling the pump volumetric displacement. Its strategy tracks the optimal system torque that conventionally is obtained by generator torque control in below-rated conditions [34].

- **Line pressure control**
  The spear valve position is used to regulate the pressure in the line. The control strategy aims for a constant, rated line pressure that minimizes kinematic losses in the pipelines.

- **Pelton speed control**
  The speed of the Pelton runner wheel is determined by the line pressure to yield optimal Pelton efficiency [35]. Subsequently, the optimal speed is regulated by controlling the applied generator torque.

2-3 Applicability of previous work to the current research

Some of the aforementioned work in earlier research provides useful elements or methods for the research in this thesis. This section aims to evaluate the aspects of previous work with respect to control. Here, the focus lies on the applicability for a wind farm with fixed-displacement pumps and a collective pipeline.

The use of fixed-displacement pumps omits the feat of decoupling the hydraulic torque and line pressure, as seen in the theoretical wind farm simulation [5]. Instead, the line pressure dictates the hydraulic torque, as encountered in the DOT500 [28].

The initial, beneficial behavior to control the line pressure by passive spear control found in the work of the DOT500, may not persist when employing a collective pipeline [28]. The varying aerodynamic torque but collective hydraulic torque results in different rotor speeds and thereby a fluctuating flow. The variation in flow imminently leads to a different pressure, unless the flow is counteracted by active adjustment of the spear position [37][38].

The active spear control strategy of the DOT500 is limited to the combination of a wind turbine and a spear position, as it maps the wind speed of a single wind turbine to an optimal spear position. Henceforth, this control strategy can only be implemented directly when using individual pipelines in the wind farm. The underlying concept of this strategy can nevertheless prove a viable solution for a collective pipeline if multiple wind speeds are translated to an optimal line pressure.

All aforementioned concepts in this chapter entail below-rated line pressure control to some extent. While the control strategy to determine the line pressure is not re-implemented, the means of subsystem control is useful. The wind farm model with variable displacement pumps uses a cascade controller compensation with PI-control (feedforward-feedback-control) [5], based on a controller comparison laid out in [36]. The combined control scheme shows swift but accurate pressure tracking.

The combination of above-rated passive spear control and conventional pitch control can be used as well [34]. Although above-rated pitch control primarily aims at preventing excessive loads, it also ensures the rated rotor speed is adhered to. As explained in Chapter 1, the individual rotor speed is not controlled and is allowed to accelerate. The extension of pitch control to below-rated conditions then is a necessity to safeguard the maximum rotor speed in below-rated conditions.

Both variable- and fixed-displacement concepts ensure maximum Pelton efficiency by determining the optimal speed from the line pressure based on an analytical relation [35]. Due to the working principle of the Pelton turbine, the Pelton control is decoupled from the other controls and is applied irrespective of the region of operation [5]. In the current research, the analytical relation is employed in a feedforward control scheme as well.

All control-related elements are summarized in the following Table:

Control of	**Applicable**	**Not applicable**
Aerodynamic torque	Conventional pitch control	
Hydraulic torque	Line pressure control	Variable displacement control
Line pressure	Active spear valve control → Controller scheme	Passive spear valve control → Control strategy
Pelton speed	Pelton feedforward control	

Chapter 3

Preliminary Theory

The Delft Offshore Turbine (DOT) uses seawater-hydraulics as power transmission, bringing forth the key feature of this concept: the opportunity of collective power generation through a hydraulic network, as illustrated in Figure 3-1. Figure 3-2 shows the sequence of energy conversion and transmission in the DOT wind farm. The aerodynamic energy is captured by the wind turbine rotor, driving the rotor shaft. The mechanical power in the rotor shaft is used to drive a hydraulic pump, where seawater is pressurized. A hydraulic network transports the hydrostatic energy to the spear valves of the Pelton turbine. In the nozzle of the spear valve, the hydrostatic energy is transitioned to hydrodynamic energy. The momentum of the fluid is captured by the buckets on the Pelton runner wheel, which directly drives the electrical generator. Lastly, the electrical generator converts mechanical energy into electric energy.

The objective of this chapter is to describe the main components that facilitate the aforementioned energy conversion and transmission. The wind energy and rotor dynamics are described in Section 3-1. Following the respective order of energy conversion, Section 3-2 explains the hydraulic pump. Section 3-3 describes the effects of the transmission by the

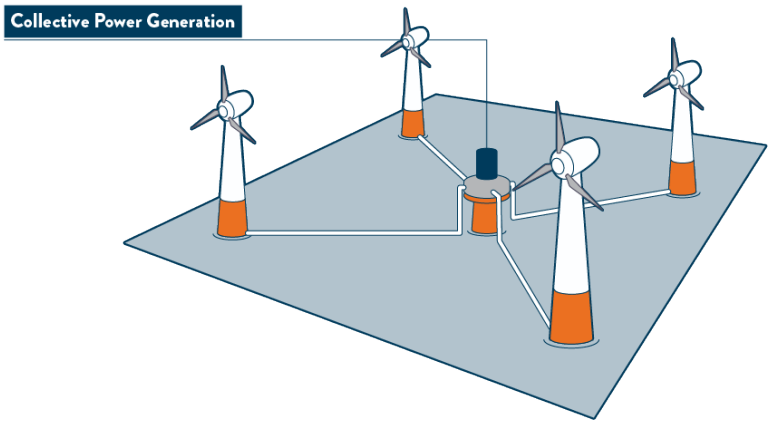

Figure 3-1: The DOT allows collective power generation through a hydraulic network [4][5].

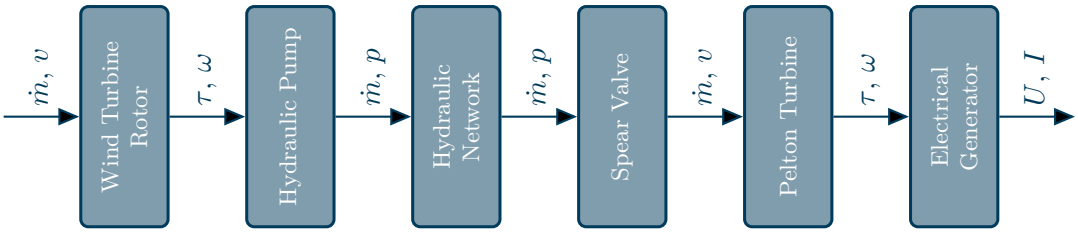

Figure 3-2: The sequence of energy conversion and transmission in a DOT wind farm.

hydraulic network. Section 3-4 elaborates on the principles governing the spear valve, followed by the Pelton turbine in Section 3-5. Finally, Section 3-6 describes the dynamics of the electrical generator.

3-1 Rotor dynamics

The purpose of a wind turbine is to extract energy from the wind and convert it to electrical energy that can be supplied to the grid. In most commercial wind turbines, the wind is extracted by three rotor blades with pitch capabilities.

The most prominent variable in wind energy reflects the rotor energy capture efficiency, and is defined as the ratio between captured energy in the rotor P_r and available wind energy P_w:

$$C_\mathrm{p} = \frac{P_\mathrm{r}}{P_\mathrm{w}}. \tag{3-1}$$

Actuator disk theory shows that the power coefficient C_p is bounded by the Lanchester-Betz-Joukowsky limit [39][40]. Betz's law states that no turbine can extract more than 59.3% of the kinetic energy from the air flow. The concept of the actuator disk theory is illustrated in Figure 3-3. Practically, wind turbine rotors reach up to 80% of the Betz limit [6][39].

The wind power P_w from Eq. (3-1) is given by the kinetic energy of the wind

$$P_\mathrm{w} = \frac{1}{2}\dot{m}_\mathrm{w} V_\mathrm{w}^2, \tag{3-2}$$

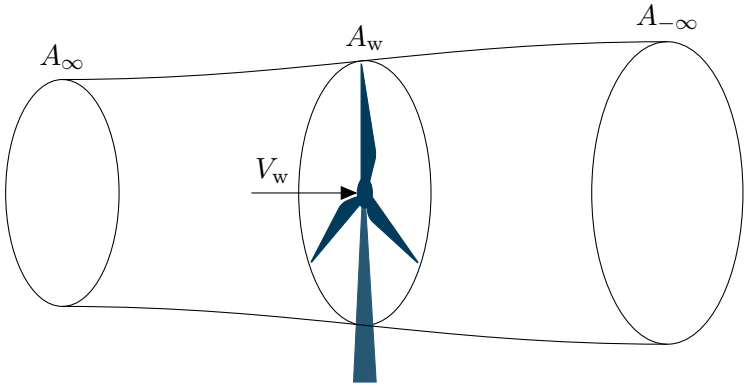

Figure 3-3: The airflow through a wind turbine, as considered in actuator disk theory.

where $\dot{m}_w$ is the mass flow rate of the wind and V_w is the mean free-stream wind speed through the disk. It is assumed that the wind passes through a transversal area A_w with a relatively uniform speed, such that the mean speed can be considered. The transversal area is a circular disk, described by the tip of the blades, as illustrated in Figure 3-3. By substitution of the mass flow $\dot{m}_w = \rho_w A_w V_w$ and the frontal area of the wind turbine $A_w = \pi R_r^2$ the following relation is obtained:

$$P_w = \frac{1}{2}\rho_w \pi R_r^2 V_w^3, \tag{3-3}$$

where ρ_w is the air density and R_r is the rotor radius. Subsequently, the rotor power is given by

$$P_r = \tau_r \omega_r, \tag{3-4}$$

where τ_r is the aerodynamic torque and ω_r is the rotor speed. The torque resulting from the aerodynamic force induced by the wind is referred to as the aerodynamic torque [39][41]

$$\tau_r = \frac{1}{2}\rho_w \pi R_r^3 V_w^2 C_\tau(\beta, \lambda), \tag{3-5}$$

where C_τ is the torque coefficient. The torque coefficient is a function of the blade pitch angle β and the Tip Speed Ratio (TSR)

$$\lambda = \frac{V_{tip}}{V_w} = \frac{\omega_r R_r}{V_w}, \tag{3-6}$$

where V_{tip} is the speed of the tip of the wind turbine rotor blades. For simplicity, a collective blade pitch is considered. Lastly, combining Eq. (3-1)-Eq. (3-6) results in

$$C_p(\beta, \lambda) = \lambda C_\tau(\beta, \lambda). \tag{3-7}$$

Often, the torque coefficient is determined based on experimental data. Some typical power and torque coefficient curves are shown in Figure 3-4

3-2 Hydraulic pump

The captured wind energy is mechanically transmitted to the hydraulic pump, which converts the mechanical energy to hydraulic energy. For an inviscid and incompressible flow, hydraulic energy can be expressed by the components of Bernoulli's equation: kinetic, potential and internal energy of the fluid [13][42]. To reduce kinetic energy losses in pipelines, a low-velocity, high-pressure flow is desired. In order to achieve high pressures, the most effective pump is a positive displacement pump as it is able to operate more efficiently at high pressures compared to other pumps [43][44].

In theory, the principles governing a positive displacement pump are fairly simple. Per cycle a fixed volume is trapped and displaced into a separate confined space [44]. This creates a flow irrespective of the feed or discharge pressure [43]. Under absence of friction and leakage, the flow of an ideal positive displacement pump is

$$Q_{h,i} = D_h \omega_h, \tag{3-8}$$

where D_h is the volumetric displacement and ω_h is the rotational speed of the pump. Neglecting the elasticity of the driving shaft, the rotational speed of the pump ω_h equals the

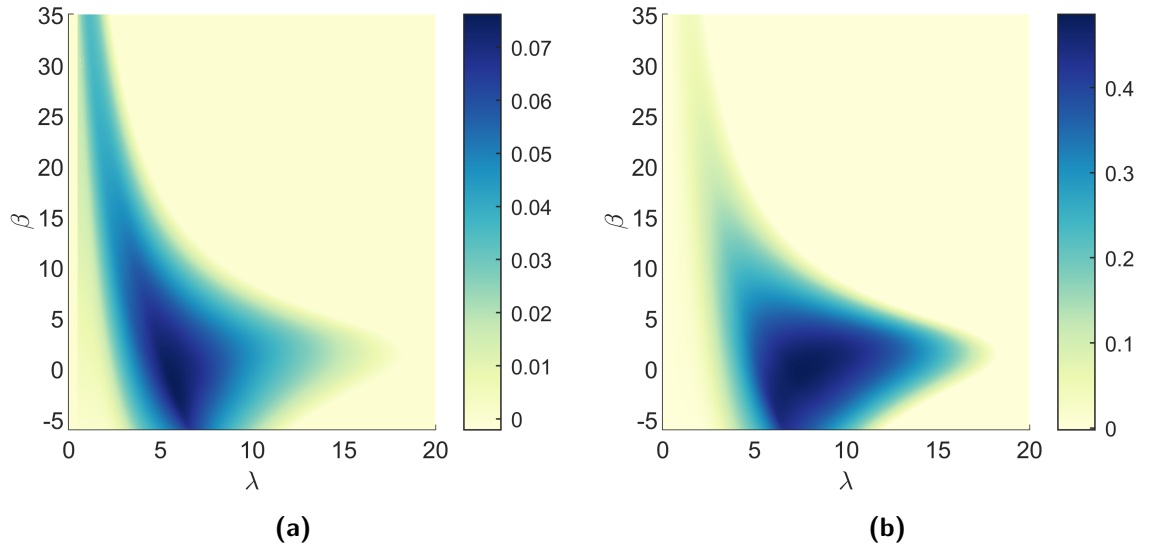

Figure 3-4: Typical (a) torque and (b) power coefficient curves for a variable speed, variable pitch wind turbine [34][39]. The tip-speed ratio λ [-] is shown on the x-axis and the blade pitch angle β [°] on the y-axis.

rotor speed ω_r. Following the same logic, the moment of inertia of the pump should be added to the effective moment of inertia of the rotor.

Due to clearances in the pump, the fluid will partially slip back in the pump [45][46][47]. The actual flow rate is then be described by

$$Q_h = D_h \omega_r - C_p \Delta p_h, \tag{3-9}$$

where C_p is the laminar leakage coefficient. The approach disregards flow losses as result of inlet restrictions that deny complete filling of the pump's chambers.

In an ideal pump, the driving power is fully transformed to hydrostatic power. Therefore, the ideal hydraulic driving torque is

$$\tau_{h,i} = \frac{Q_{h,i} \Delta p_{h,i}}{\omega_r} = D_h \Delta p_{h,i}. \tag{3-10}$$

Several mechanical losses in the pump attribute to an elevated hydraulic driving torque, which effectively becomes

$$\tau_h = D_h \Delta p_h + \tau_d + \tau_f + \tau_{seal}, \tag{3-11}$$

where τ_d, τ_f and τ_{seal} reflect the mechanical torques from damping-, frictional- and seal components. The damping torque τ_d is a result of the viscous forces from the moving surfaces and viscosity of the fluid and is proportional to the rotational speed [45]. Subsequently, the frictional torque τ_f is a resultant torque by virtue of the pressure on the geometry of the pump. This yields the hydraulic driving torque

$$\tau_h = (1 + C_f) D_h \Delta p_h + \xi_d D_h \omega_r + T_{seal}. \tag{3-12}$$

where C_d is the viscous damping coefficient, μ is the dynamic viscosity of the displaced fluid and C_f is the Coulomb frictional coefficient. For simplicity, a constant Coulomb frictional coefficient is used for quasi-static analysis [4].

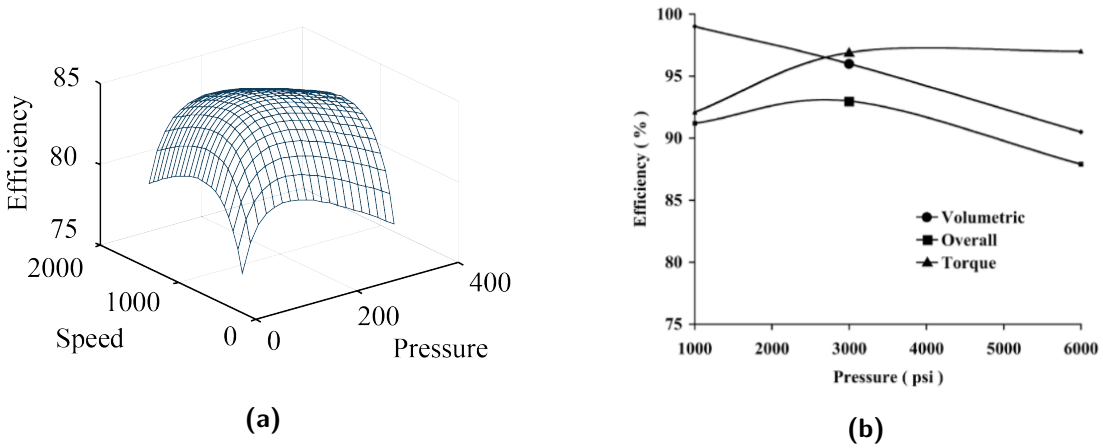

Figure 3-5: The overall efficiency of a positive displacement pump (a) depends on both speed and differential pressure [45][48]. The composition of the overall efficiency (b), consisting of mechanical and volumetric efficiency, is given for a fixed pump speed [49].

The mechanical efficiency is defined as the ratio of the actual and ideal torque [13]. The seal torque is often negligible, allowing simplification to the elegant form [45]

$$\eta_{\mathrm{m}} = \left(1 + \frac{\xi_{\mathrm{d}}\omega_{\mathrm{r}}}{\Delta p_{\mathrm{h}}} + C_{\mathrm{f}}\right)^{-1}. \tag{3-13}$$

A typical graph of the volumetric, mechanical and combined efficiencies is shown in Figure 3-5a and 3-5b.

3-3 Hydraulic network

The main perk of the DOT-concept - centralized electricity generation through seawater in open-loop - is facilitated by a hydraulic network that transports the hydrostatic energy from the individual wind turbines to a generator platform. As found in literature, a great consideration when employing a hydraulic network is its subjection to water hammer effects [44][50]. A model that accurately reflects these effects is therefore important for the control design.

The dynamics of a pipe flow are modeled using a lumped parameter approach, resulting in ordinary differential equations that accurately show transient and frequency responses [51][52]. A second-order differential analogous to a mass-spring-damper system is considered to model the dynamic pipe flow [4][50]. This model makes use of three basic elements: hydraulic induction, - resistance and - capacitance. Some of these elements are in turn dependent on the type of flow, defined by the Reynolds number.

3-3-1 Reynolds number

There exist two distinct types of flow and are illustrated in Figure 3-6: laminar and turbulent [37]. Between these distinct regimes, a combination of these extrema is present as given

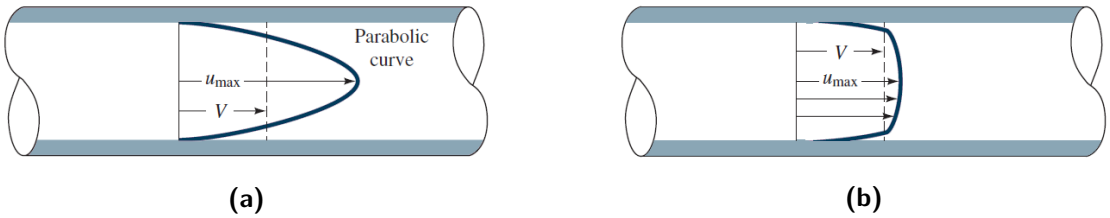

Figure 3-6: Velocity profiles of (a) laminar and (b) turbulent flows through a pipeline [37]. The laminar velocity profile shows a parabolic curve, whereas the turbulent flow shows an equal velocity.

in Figure 3-7: laminar, critical, transition and turbulent. As shown, the type of flow is determined by the Reynolds number

$$Re = \frac{4\rho_f Q}{\pi \mu D_p} \tag{3-14}$$

where ρ_f is the fluid's density, Q the flow, μ the dynamic viscosity and D_p the circular pipe diameter.

Turbulent Flows in the DOT

To show that the flow will always be turbulent for the application of the DOT, consider the following simple calculation for illustration. The purpose of a DOT wind turbine is to compete with conventional wind turbines and is therefore likely to have similar power ratings. Consider the seawater properties in Table 3-1 and a pipe diameter $d_p = 1\,\text{m}$ for the following calculations at cut-in and nominal power:

Cut-in Power	*Nominal Power*
$P = 100\,\text{kW}$	$P = 5\,\text{MW}$
$\Delta p = 500\,\text{bar}$	$\Delta p = 500\,\text{bar}$
$Q = P/\Delta p = 0.001\,\text{m}^3/\text{s}$	$Q = P/\Delta p = 0.001\,\text{m}^3/\text{s}$
$Re = 4\rho Q/\pi\mu D = 1.04 \cdot 10^4$	$Re = 4\rho Q/\pi\mu D = 1.10 \cdot 10^5$

From Figure 3-7, it can then be concluded that both flows are turbulent for these parameters. Subsequently, it can also be seen that a higher power rating, lower operating pressure or smaller pipe diameter would only further strengthen this reasoning and as such will result in turbulent flow for the DOT.

Salinity	S	35	[‰]
Density	ρ_f	1026	[kg/m^3]
Dynamic viscosity	μ	$1.23 \cdot 10^{-3}$	[N s/m^2]
Internal surface roughness	ϵ	0.05	[mm]
Effective bulk modulus	E_f	$2.33 \cdot 10^9$	[N/m^2]

Table 3-1: Pipe and seawater properties at 15° C [37][53]

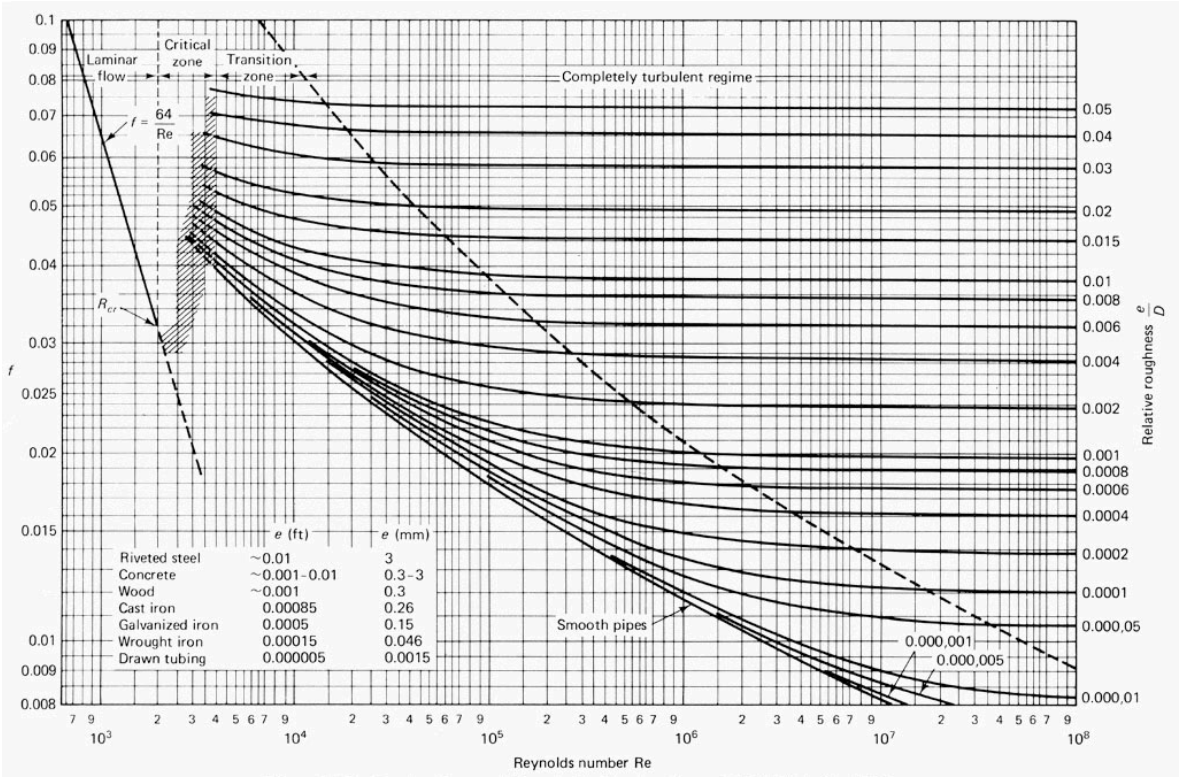

Figure 3-7: Moody's Chart maps the Reynolds number Re and relative roughness ϵ/D to the frictional coefficient f for a circular pipe [37][54]. The distinct laminar and turbulent flows are shown on the left and right respectively. The critical and transition region in-between show a combination of aforementioned distinct flows.

3-3-2 Hydraulic induction

The hydraulic induction is analogous to the mass of a mass-spring-damper system and signifies the resistance to acceleration of the fluid. For a pipeline, the hydraulic induction L_{H} is defined as the fluid inertia in the control volume

$$L_{\mathrm{H}} = I_{\mathrm{f}} = \rho_{\mathrm{f}} \frac{L_{\mathrm{c}}}{A_{\mathrm{p}}} = \frac{4\rho_{\mathrm{f}} L_{\mathrm{c}}}{\pi D_{\mathrm{p}}^2}. \tag{3-15}$$

where L_c is the length of the control volume. In this derivation, the assumption is made that the fluid in the control volume has a uniform speed [51]. While laminar flows show a decreasing speed towards the pipe walls (Figure 3-6), this is an accurate assumption for turbulent flows and thus for the DOT [37].

3-3-3 Hydraulic resistance

The hydraulic resistance is similar to classical mechanical friction as it symbolizes the resistance to velocity. In hydraulic fluid power systems, this relates to the pressure loss over the flow and is given by the Darcy-Weisbach formula [50][51]

$$R_{\mathrm{H}} = \frac{8\rho_{\mathrm{f}} L_{\mathrm{c}} Q}{\pi^2 D_{\mathrm{p}}^5} f, \tag{3-16}$$

where f is the frictional coefficient. The hydraulic resistance imposed by a pipeline is solely based on frictional resistance with the pipe walls, which varies for laminar and turbulent flows. In case of laminar flows, the frictional coefficient f is given by

$$f = \frac{64}{Re} \tag{3-17}$$

and results in a hydraulic resistance

$$R_{\mathrm{H}} = \frac{128 \mu L_{\mathrm{c}} Q}{\pi D_{\mathrm{p}}^4} \tag{3-18}$$

for laminar flows.

The frictional coefficient of turbulent flows is less convenient and can be evaluated by solving the Colebrook-White equation:

$$f = \left(-2 \log \left[\frac{2.51}{Re\sqrt{f}} + \frac{\epsilon_{\mathrm{p}}}{3.7 D_{\mathrm{p}}} \right] \right)^{-2}, \tag{3-19}$$

where ϵ_p is the effective internal surface roughness. As this equation has to be solved recursively, the simplified the Haaland approximation is preferred [55]

$$f = \left(-1.8 \log \left[\frac{6.9}{Re} + \left(\frac{\epsilon}{3.7 D_{\mathrm{p}}} \right)^{1.11} \right] \right)^{-2}, \tag{3-20}$$

which is accurate for $4000 < Re < 10^8$ [55][56].

Finally, substituting the Haaland approximation of the Colebrook-White formula in the Darcy-Weisbach formula yields the hydraulic resistance [36]

$$R_{\mathrm{H}} = \frac{8 \rho L_{\mathrm{c}} Q}{\pi^2 D_{\mathrm{p}}^5} \left(-1.8 \log \left[\frac{6.9}{Re} + \left(\frac{\epsilon_{\mathrm{p}}}{3.7 D_{\mathrm{p}}} \right)^{1.11} \right] \right)^{-2} \tag{3-21}$$

for turbulent flows.

3-3-4 Hydraulic capacitance

The hydraulic capacitance is equivalent to the spring stiffness in a mechanical system and represents the resistance to a change of volume [37]. There are two factors contributing to this effect: the compressibility of the fluid and the elasticity of the pipeline. The hydraulic capacitance is the inverse of the hydraulic spring stiffness, given by

$$C_{\mathrm{H}} = \frac{V_{\mathrm{c}}}{E_{\mathrm{f}}} = \frac{\pi D_{\mathrm{p}}^2 L_{\mathrm{c}}}{4 E_{\mathrm{f}}} \tag{3-22}$$

where E_{f} is the effective bulk modulus.

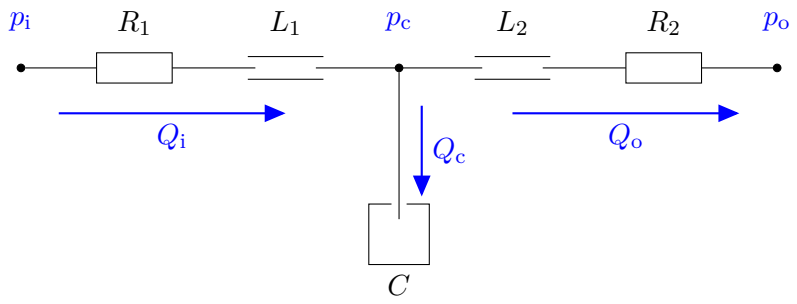

Figure 3-8: A representation of a pipeline segment and its hydraulic properties for the non-linear time-invariant state-space model [36]. The i- and o-subscripts signify the input and output properties.

3-3-5 Non-linear time-invariant model

The complication of the system is the inconvenient circular dependency: the hydraulic resistance is determined by the flow rate going through the pipeline, which in turn depends on the resistance it encounters [37]. Iterative methods can be used to obtain a viable solution for a certain interval, but only provide an accurate solution for a steady-state flow. A dynamic flow can be captured in a Linear Parameter Varying (LPV) state-space model that is used to represent the nonlinear terms. This is essentially the same as a non-linear time-invariant state-space model, which updates the coefficient matrices of the state-space model at every step of the simulation to reflect nonlinear resistive terms [36].

Consider a single pipeline segment as displayed in Figure 3-8. Subsequently, from the definition of the hydraulic properties, it can be seen that for each branch holds

$$p_i - p_c = R_1 Q_i + L_1 \dot{Q}_i \tag{3-23}$$

$$p_c - p_o = R_2 Q_o + L_2 \dot{Q}_o. \tag{3-24}$$

Using the law of flow continuation, the net flow is

$$Q_c = Q_i - Q_o. \tag{3-25}$$

Lastly, from the definition of hydraulic capacitance follows

$$Q_c = C \dot{p}_c \tag{3-26}$$

Rewriting Eq. (3-26) yields

$$\dot{p}_c = \frac{1}{C} Q_c \tag{3-27}$$

Substituting Eq. (3-25) in Eq. (3-24) yields

$$p_c - p_o = R_2 Q_i - R_2 Q_c + L_2 \dot{Q}_i - L_2 \dot{Q}_c, \tag{3-28}$$

which can be rewritten to

$$\dot{Q}_c = \frac{R_2}{L_2} Q_i - \frac{R_2}{L_2} Q_c + \dot{Q}_i - \frac{1}{L_2} p_c + \frac{1}{L_2} p_o. \tag{3-29}$$

Lastly, substituting Eq. (3-27) in Eq. (3-28) gives

$$\ddot{p}_c = \frac{R_2}{CL_2}Q_i - \frac{R_2}{L_2}\dot{p}_c + \frac{1}{C}\dot{Q}_i - \frac{1}{CL_2}p_c + \frac{1}{CL_2}p_o \tag{3-30}$$

Eq. (3-27), Eq. (3-30) and Eq. (3-29) then fully capture the dynamics of a single-segment pipeline.

From the in-going flow and pressure and out-going flow and pressure, two parameters can be selected as input and two as output. Based on this selection, a state space can be derived from the equations above.

With the other components in mind, the inputs are chosen to be the input flow and output pressure, leaving the other two as output variables. It is assumed that the pipe branches have an equal length and the pipe diameter is constant, allowing the simplification $L = L_1 = L_2$. The single-segment pipeline considered as illustrated in Figure 3-8, can then be represented by the following non-linear time-invariant state-space model

$$\begin{bmatrix} \dot{p}_\mathrm{c} \\ \ddot{p}_\mathrm{c} \\ \dot{Q}_\mathrm{c} \end{bmatrix} = \begin{bmatrix} 0 & 0 & \frac{1}{C} \\ \frac{-1}{CL} & \frac{-R_2}{L} & 0 \\ \frac{-1}{L} & 0 & \frac{-R_2}{L} \end{bmatrix} \begin{bmatrix} p_\mathrm{c} \\ \dot{p}_\mathrm{c} \\ Q_\mathrm{c} \end{bmatrix} + \begin{bmatrix} 0 & 0 & 0 \\ \frac{1}{CL} & \frac{R_2}{CL} & \frac{1}{C} \\ \frac{1}{L} & \frac{R_2}{L} & 1 \end{bmatrix} \begin{bmatrix} p_\mathrm{o} \\ Q_\mathrm{i} \\ \dot{Q}_\mathrm{i} \end{bmatrix} \tag{3-31}$$

$$\begin{bmatrix} p_\mathrm{i} \\ Q_\mathrm{o} \\ Q_\mathrm{c} \end{bmatrix} = \begin{bmatrix} 1 & 0 & 0 \\ 0 & 0 & -1 \\ 0 & 0 & 1 \end{bmatrix} \begin{bmatrix} p_\mathrm{c} \\ \dot{p}_\mathrm{c} \\ Q_\mathrm{c} \end{bmatrix} + \begin{bmatrix} 0 & R_1 & L \\ 0 & 1 & 0 \\ 0 & 0 & 0 \end{bmatrix} \begin{bmatrix} p_\mathrm{o} \\ Q_\mathrm{i} \\ \dot{Q}_\mathrm{i} \end{bmatrix}. \tag{3-32}$$

The time simulation results displayed in Figure 3-9 clearly demonstrate the ability to reflect water hammer effects [36].

3-4 Spear valve

The hydraulic network ends at the spear valves, as illustrated in Figure 3-10. The fluid flows from a high pressure in the pipeline to atmospheric pressure as it leaves the nozzle. As shown,

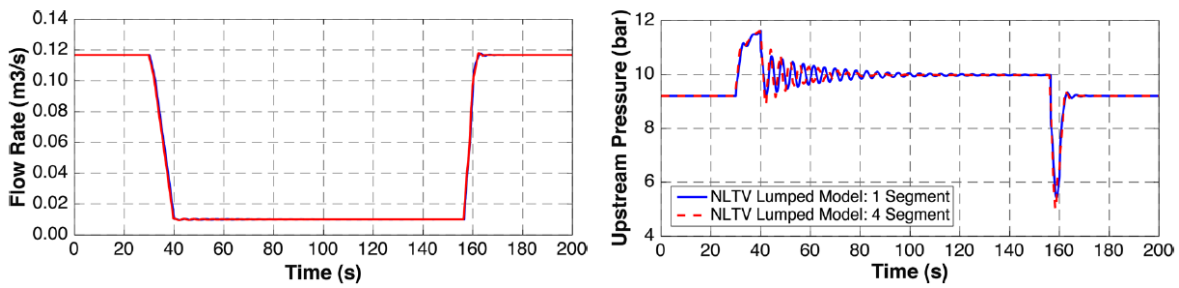

Figure 3-9: A time simulation of the non-linear time-invariant state-space model showing water hammer effects [36].

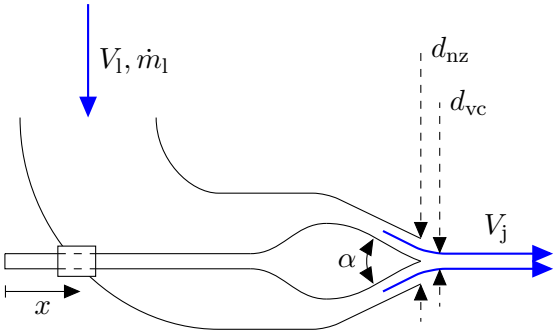

Figure 3-10: An illustration of the flow along the spear through the nozzle. The low-velocity, high-pressure flow is transitioned in the nozzle to a high-velocity jet at atmospheric pressure.

the flow passes the spear and is compressed to a smaller exiting area, referred to as the nozzle area.

For an ideal flow, Bernoulli's principle applies [37][57]:

$$\Delta p + \frac{1}{2}\rho_\mathrm{f} V^2 + \rho_\mathrm{f} g z = \mathrm{C}. \tag{3-33}$$

Since the nozzle is directed horizontally in the Pelton turbine, there is no significant height difference allowing to neglect the third, potential term. It can then be seen that the pressure difference results in a significant velocity increase. In other words, in the nozzle, the hydrostatic flow is transformed into a hydrokinetic flow. The exiting velocity of an ideal flow is then given by

$$V_\mathrm{j} = \sqrt{V_\mathrm{l}^2 + \frac{2\Delta p_\mathrm{n}}{\rho_\mathrm{f}}}, \tag{3-34}$$

where V_l is the velocity in the line, ρ_h the water density and Δp_n the pressure differential over the nozzle.

Kinematic Influence on Jet Speed

Given that the line operates at high pressure and low flow rate, the energy contribution of the velocity in the line V_l is negligible. To underline this statement, consider the flow from Section 3-3 of $Q_\mathrm{e} = 0.1\,\mathrm{m}^3/\mathrm{s}$. Take a small pipeline diameter of $D_\mathrm{e} = 0.1\,\mathrm{m}$ and lower differential pressure of $\Delta p_\mathrm{e} = 100\,\mathrm{bar}$. This results in a line velocity of $V_\mathrm{l} = Q_\mathrm{e}/A_\mathrm{l} = 12.7\,\mathrm{m/s}$. With the seawater properties of Table 3-1, this yields $V_\mathrm{j,e} = \sqrt{162.1 + 19493.2} = 140.2\,\mathrm{m/s}$. The contribution of the line velocity is clearly negligible even under advantageously chosen parameters. It can be seen that more realistic values, such as a larger pipeline diameter and higher differential pressure, would result in an even smaller contribution than given above. Hence, Eq. (3-34) is simplified to

$$V_\mathrm{j} = \sqrt{\frac{2\Delta p_\mathrm{n}}{\rho_\mathrm{h}}}. \tag{3-35}$$

This expression however neglects viscous friction losses in the nozzle that can be modelled by the velocity coefficient C_v, resulting in

$$V_\mathrm{j} = C_\mathrm{v}\sqrt{\frac{2\Delta p_\mathrm{n}}{\rho_\mathrm{h}}}, \tag{3-36}$$

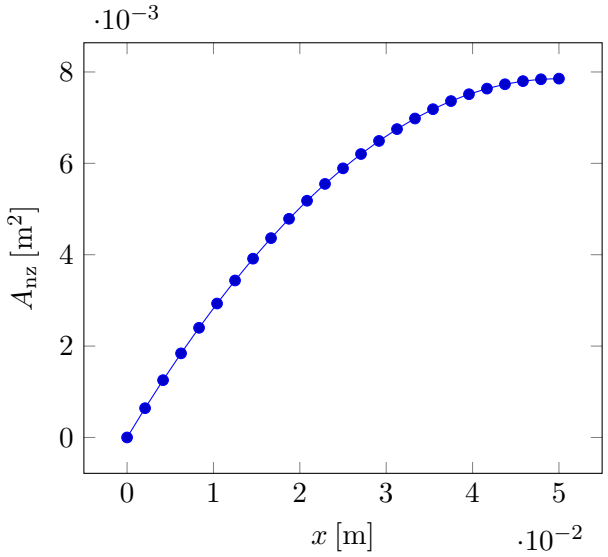

Figure 3-11: The nozzle area A_{nz} as a function of the spear valve position x.

where C_{v} typically lies between 0.92 and 0.98 for well-designed nozzles [37].

After exiting the orifice, the jet typically converges further to the vena contracta [38]. At the vena contracta, the jet cross section is at its minimum and therefore the jet velocity at its maximum [57]. It is assumed that this effect is negligible due to the shape of

Given the exiting velocity, the total outgoing flow is defined by the product of the exiting velocity and the nozzle area. Subsequently, the nozzle area can be manipulated by controlling the position of the spear valve, as shown in Figure 3-11. The explicit relation between the spear valve position and the nozzle area is given by

$$A_{\text{nz}} = \pi \left(\frac{1}{4} d_{\text{nz}}^2 - (x \tan(\alpha/2))^2 \right), \tag{3-37}$$

where d_{nz} is the nozzle diameter, x the spear position and α the angle of the spear tip, as shown in Figure 3-10. Naturally, the effective nozzle area is bounded by: $0 \leq A_{\text{nz}} \leq \frac{\pi}{4} d_{\text{nz}}^2$.

Finally, this yields the outgoing flow rate

$$Q_{\text{nz}} = V_{\text{nz}} A_{\text{nz}}. \tag{3-38}$$

Subsequently, as the nozzle area can be manipulated by the spear position, the outgoing flow rate can be controlled. The imbalance between the ingoing and outgoing flow rate of the pipeline will result in a change of pressure until a new steady-state is obtained. Hence by varying the spear position, the pressure at the nozzle can be regulated. Lastly, as sudden changes in flow or pressure at the spear valve may induce water hammer effects and caution should be taken when manipulating the spear position [37][44].

3-5 Pelton turbine

In the Pelton turbine, the hydrokinetic energy is converted to mechanical energy. As shown in Figure 3-12a, a water jet is directed at a runner wheel with buckets. Subsequently, the

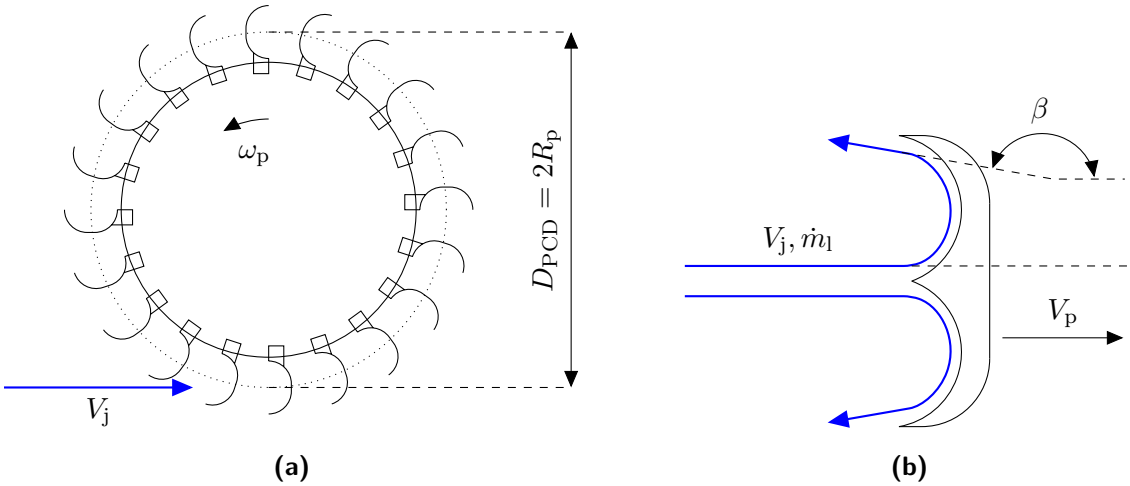

Figure 3-12: Schematic overview of the working principle of the Pelton turbine. The water jet is captured by (a) the buckets on the Pelton runner wheel. The capture efficiency is affected by (b) the deflection of the flow in the bucket [35].

momentum of the water exerts a force on the buckets due to the deflection of the jet. The combined force on the buckets provides a mechanical torque on the runner wheel.

The water jet enters in the middle of the bucket and ideally exits in the opposite direction, as depicted in Figure 3-12b. Consider an ideal flow, then the force exerted by the jet on a single bucket is

$$F_b = \dot{m}_j(V_j - V_b)(1 - \cos\beta) \tag{3-39}$$

where $\dot{m}_j$ is the mass flow of the jet, V_j the jet speed, V_b the bucket speed and β the deflection angle between entering and exiting direction of the fluid. Generally, the water jet is directed at the Pitch Circle Diameter (PCD) of the runner wheel D_{PCD}.

The bucket speed depends on its position on the runner wheel and is given by

$$V_b = \omega_p R_b, \tag{3-40}$$

where R_b is the radius, equal to half the PCD.

Following classical mechanics, the total power on the runner is then given by

$$P_p = \sum_{n_b} F_b V_b = \dot{m}_l(V_j - V_p)(1 - \cos\beta)V_p, \tag{3-41}$$

where n_b is the number of nozzles and $\dot{m}_l$ the total mass flow in the line.

The total available kinetic power in the water jets is

$$P_j = \frac{1}{2}\dot{m}_l V_j^2. \tag{3-42}$$

The efficiency of the Pelton turbine η_p can be described by the ratio of the captured mechanical power and the available kinetic power [35]:

$$\eta_p = \frac{P_p}{P_j} = 2\left(\frac{V_b}{V_j} - \frac{V_b^2}{V_j^2}\right)(1 - \cos\beta) \tag{3-43}$$

Definition of the relative velocity, called the peripheral speed coefficient $k = V_{\mathrm{p}}/V_{\mathrm{j}}$, yields

$$\eta_{\mathrm{p}} = 2k(1-k)(1-\cos\beta). \tag{3-44}$$

Evidently the efficiency is maximum if $\dot{\eta}_{\mathrm{p}} = 2(1-2k) = 0$. This means that the efficiency is maximum when $V_{\mathrm{p}}/V_{\mathrm{j}} = 0.5$ and is thus irrespective of the deflection angle α. In practice, as a result of bearing and windage losses, the peripheral speed coefficient is ideally in the range of 0.45-0.48 [35][58]. Therefore, maximum efficiency can be achieved by proper design and controlling the jet and bucket speed correctly.

Firstly, the jet speed is dictated by the pressure differential over the nozzle as explained in Section 3-4. In theory, the jet speed can be controlled by the spear valve position. More conventional however aims to control the bucket speed by adjusting the generator torque, which is described in Section 3-6.

Continuing on Eq. (3-44), when considering the effects of frictional losses of the water jet in the bucket, the exiting velocity changes. This results in

$$\eta_p = 2k(1-k)(1-\underbrace{\left(1-\frac{1}{2}c_{\mathrm{w}}\right)}_{\xi_{\mathrm{p}}}\cos\beta), \tag{3-45}$$

where c_w is the friction number as derived from frictional losses considered in [35].

Finally, the shaft torque provided by the runner wheel can be described by

$$\tau_{\mathrm{p}} = \frac{\eta_{\mathrm{p}} P_{\mathrm{j}}}{\omega_{\mathrm{p}}} \tag{3-46}$$

3-6 Electrical generator

In the last step of the chain, an electrical generator converts the mechanical energy to electrical energy. In order to feed the electrical power directly to the grid, alternating current (AC) generators are employed. Generally, AC generators can be divided into two classes: synchronous and asynchronous [59][60]. Synchronous generators must run at a certain speed in order to correctly supply power to the grid, whereas asynchronous generators do not have this constraint [25]. Since the optimal Pelton runner wheel speeds are expected to vary, as explained in the previous sections, an asynchronous generator is the preferred option.

In the generator, induction produces the electromotive force from interaction with the magnetic flux, created by the rotation. By adjusting the leakage of the magnetic flux, the generator torque can be adjusted. Therefore, assuming a rigid connection, its dynamics can be simplified to a first-order model:

$$\dot{\omega}_{\mathrm{g}} = \dot{\omega}_{\mathrm{p}} = \frac{1}{J_{\mathrm{pg}}}(\tau_{\mathrm{m}} - \tau_{\mathrm{g}}), \tag{3-47}$$

where ω_g is the rotational speed of the generator rotor, J_{pg} the combined moment of inertia of the Pelton & generator, τ_m the mechanical torque applied to the generator and τ_g the electrical

torque due to induction. Subsequently, from Eq. (3-47) it follows that the rotational speed can be controlled by controlling the electrical torque.

The available mechanical power at the generator becomes

$$P_{\mathrm{g}} = \tau_{\mathrm{g}} \omega_{\mathrm{g}}. \tag{3-48}$$

With a collective pipeline, the capacitance and high moments of inertia suggest an absence of sharp fluctuations in mechanical power. Assuming a relatively steady mechanical power, a static approximation of the generator efficiency is used for purposes of simplicity. The generated electrical power is then given by

$$P_{\mathrm{e}} = P_{\mathrm{g}} \eta_{\mathrm{g}}, \tag{3-49}$$

where η_{g} is the efficiency of the generator.

Chapter 4

Control Strategy

A wind turbine consists of many components, each with its own purpose. These can vary from an actuator for blade pitch to a braking system to decelerate the rotor for an emergency shutdown. For the wind turbine to operate effectively and safely, all systems have to harmoniously function in unity. This task rests upon the wind turbine control system. At the core of the wind turbine control system lies the strategy that defines how the wind turbine behaves to pursue its goals. This chapter focuses on the latter and derives the control strategy for the Delft Offshore Turbine (DOT) wind farm.

The chapter starts with an explanation of the general objectives of a control strategy in Section 4-1. Thereafter, Section 4-2 describes the conventional below-rated control strategy. Section 4-3 concludes this chapter and elaborates on the derivation of a below-rated control strategy for the DOT.

4-1 Control objective

The most general purpose of a wind turbine is to safely harvest electrical power from the available wind power. Unfortunately, wind power is an energy resource with strong spatial and temporal variations [61][62]. This variability imposes challenges for the operation of a wind turbine. Consequently, the primary objective to produce power is subject to several physical and economic constraints, defined in three partial objectives [39]:

- **Energy capture**
  This objective focuses on maximizing the power production. It is the most important partial objective as it directly promotes the purpose of the wind turbine.
- **Mechanical loads**
  The annual contribution of extreme wind speeds is negligible and therefore uneconomical to account for in the designed operation of the wind turbine. In above-rated conditions, the control therefore has to ensure that the structural integrity is maintained by pitching

away or disabling operation. Furthermore, numerous strategies aim at load reduction both below- and above-rated by actively controlling pitch or yaw [33].

- **Power quality**
  The variable nature of wind causes voltage fluctuation and flicker emission [25][62]. The power quality has to comply with regulations in order to be supplied to the grid [63].

All subjects are inherently interwoven and assessed in economic terms, resulting in a combined Levelized Cost of Energy (LCOE) [33]. The overall control objective of the wind turbine can then mathematically be defined to minimize this cost function, accounting for the imposed physical and economic constraints.

The reduction of mechanical loads from i.a. wake interference, or constant power production by the Pelton turbine, are subjects of interest. Nevertheless, this research initially aims solely at pursuing maximum power production.

4-2 Conventional control

The control strategy of a wind turbine defines how it pursues its objectives. For conventional wind turbines, the mode of operation and the importance of objectives depend on the wind speed. The regions of operation are laid out in the next subsection, followed by the control strategy in the subsection thereafter.

4-2-1 Regions of operation

Regions of operation are characterized by the mean wind speed perceived by the wind turbine, as shown in Figure 4-1 [6][62]. In region I, the wind does not have sufficient power to effectively overcome the losses in the wind turbine and does not compensate for the operation costs [39]. For wind speeds above the cut-in speed, the wind turbine tracks optimal performance in region II. When the wind turbine meets its designed maximum rotor speed before its rated power, a transition region IIb is introduced. In region III, the wind power surpasses the designed power rating of the turbine. Lastly, in region IV, the wind speed exceeds the cut-out speed and operation is no longer safe due to excessive mechanical loads.

4-2-2 Conventional control strategies

This section focuses exclusively on the regions between cut-in and cut-out speed, where the wind turbine is in operation. In below-rated conditions, the wind turbine operates at partial load [62]. The control objective of particularly maximizing energy capture is pursued in region II, often referred to as the Maximum Power Point Tracking (MPPT) strategy [64][65]. In conventional wind turbines, this is attained by maintaining fine-pitch and the optimal tip-speed ratio. The optimal tip-speed ratio is actively pursued by controlling the generator torque through the analytical relation

$$\tau_{\mathrm{g}} = K_{\mathrm{opt}} \omega_{\mathrm{g}}^2 \tag{4-1}$$

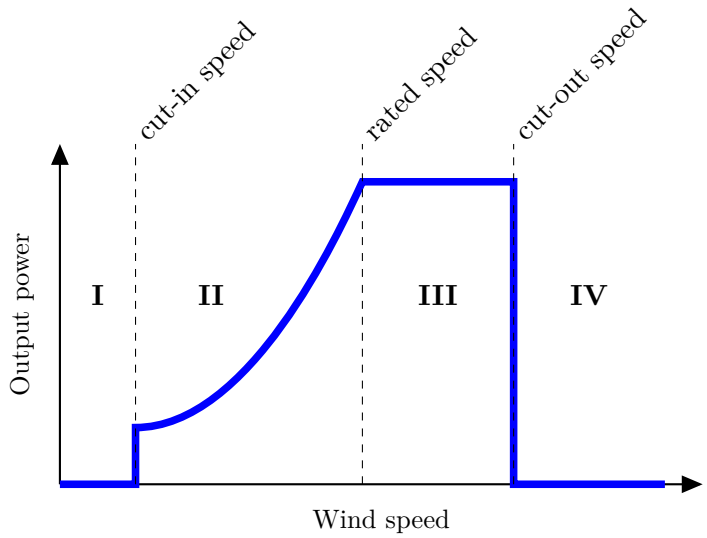

Figure 4-1: The captured power of a wind turbine over the wind speed. The regions of operation are notated by the Roman numerals. The speeds that define the boundaries between regions are indicated by the dashed lines.

where K_{opt} is the optimal feedforward gain.

If the wind turbine has the transition region IIb, the rotor speed is limited before it attains its rated power. The rotor speed is then regulated by steeply increasing the generator torque through torque control. The generated power increases, notwithstanding that the rotor efficiency decreases as result of deviation from the optimal tip-speed ratio in this region.

Above the rated wind speed, in Region III, the capture of aerodynamic torque is limited to ensure the wind turbine operates within its design limitations and avoids excessive mechanical and electrical loads [33]. The control objective therefore changes from maximizing power to limiting power by pitching the blades and intentionally reduce the rotor efficiency.

4-3 The Delft Offshore Turbine

Conventional above-rated pitch control is easily implemented in the current research as stated earlier in Chapter 2. A varying aerodynamic torque but shared hydraulic torque in below-rated conditions, however, lead to the inability to control individual rotor speeds. Suboptimal rotor efficiency is imminent and therefore, the below-rated control strategy is of more importance, as it effectively determines to what extent the available wind power is captured.

The variance in wind speed is approached by the minimum and maximum wind speed in the wind field, referred to as the wind extrema. First, a statistical analysis of the wind in the North Sea is made to set focus on the area that is optimized for performance further on. Then, the maximum power production of a DOT wind farm is determined for each combination of the wind extrema within the probability interval. Lastly, several control strategies are derived and evaluated for their ability to attain the maximum power production.

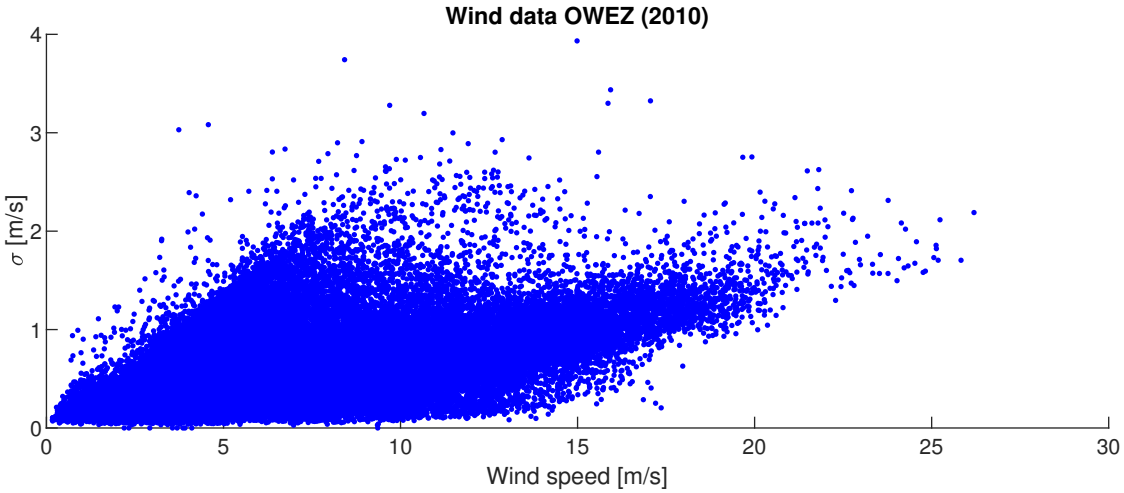

Figure 4-2: The raw data points of the wind speed in the OWEZ at an altitude of 70 m [66]. The data points represent mean and standard deviation of the measured wind speed in a 10-minute interval.

4-3-1 Wind probability of the North Sea

It is important to account for the probability of a combination of wind extrema to occur. For example, the odds of one wind turbine having a wind speed of 4 m/s and the other of 20 m/s, are virtually non-existent. It therefore stands to reason not to include such scenarios when deriving a control strategy.

The wind data of the entire year 2010 of an offshore wind farm in the North Sea, the Offshore Windpark Egmond aan Zee (OWEZ), is used [66]. The available data consists of a combination of measurements: an ultrasonic anemometer, three rotary anemometers and three wind vanes, each at heights 21 m, 70 m and 116 m [67]. The encountered wind speeds increase at higher altitudes, but for purposes of simplicity only the wind speed at hub height, 70 m, is considered [68].

The original data gives the mean and standard deviation of both wind direction and wind speed, aggregated over an interval of 10 minutes. For illustration, Figure 4-2 showcases the raw data points of the wind speed. The wind direction determines whether the measurement tower is in the wake of the wind farm. As such, the wind data is able to give a fair representation of the disturbed and undisturbed wind speeds encountered throughout a wind farm.

The raw aggregate data is binned in wind speeds at an interval of 0.25 m/s. Assuming an equal number of measurement samples in each 10-minute interval, the average and standard deviation of the bins become

$$\mu_{\text{bin},j} = \frac{1}{n_j} \sum_{i=1}^{n_j} [\mu_i] \tag{4-2}$$

$$\sigma_{\text{bin},j} = \sqrt{\frac{1}{n_j} \sum_{i=1}^{n_j} [\sigma_i^2 + (\mu_{\text{bin},j} - \mu_i)^2]} \tag{4-3}$$

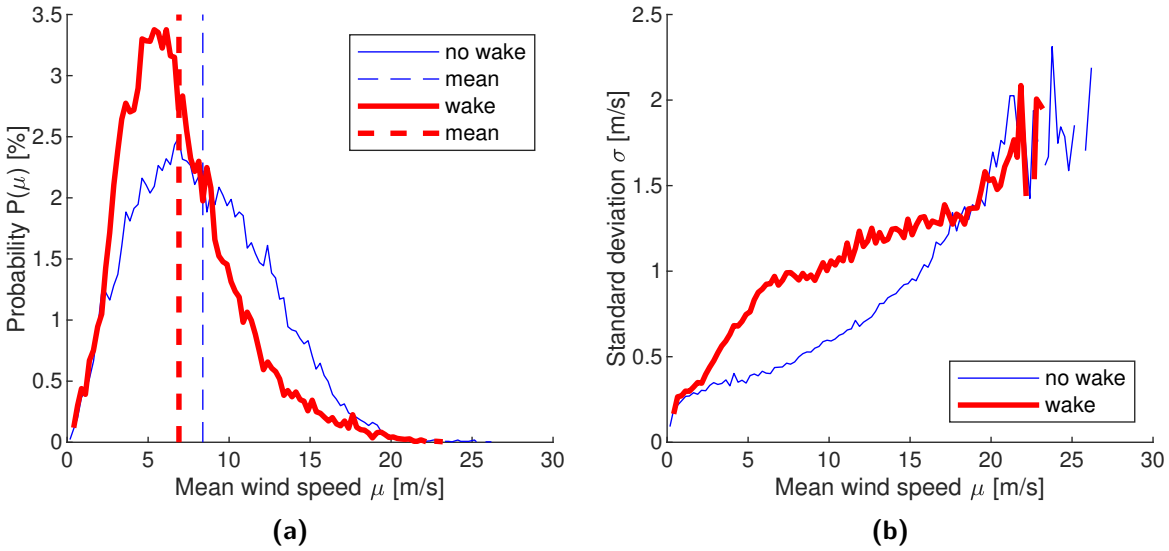

Figure 4-3: The (a) probability distribution of the bin mean wind speed shows a Weibull distribution [6][39][41]. The overall mean wind speed are indicated by the dashed lines. The (b) standard deviation of the wind speed increases for higher bin mean wind speeds.

with μ_i and σ_i the mean and standard deviation of the aggregate data point and n_j the number of aggregate data points in the j-th wind speed bin.

Furthermore, the probability of the j-th wind speed bin is calculated by

$$P(\mu_{\text{bin},j}) = \frac{n_j}{n_t} \tag{4-4}$$

where n_t represents the total number of data points in all wind speed bins.

In all calculations, a distinction is made between the presence and absence of wake effects from the wind farm. This results in the probability distribution of the mean wind speed in Figure 4-3a and its corresponding standard deviation in Figure 4-3b. The expected Weibull-distribution is clearly recognised in the left image. Furthermore, it shows a lower average wind speed in the presence of wake effect.

In Figure 4-3b, the standard deviation grows in an exponential fashion in absence of wake. Presence of wake introduces a higher standard deviation at lower wind speeds but does not appear to alter the standard deviation at higher wind speeds. Presumably, this is a result of already turbulent behavior exhibited at higher wind speeds.

Combining the probability and variance of wind speed fuses both maps into one probability map for two winds speeds as shown in Figure 4-4. The values of the wind probability depend on the size of the bins and are merely shown to better reflect the shape. The boundaries of both the 95%- and 99.7%-probability interval are shown.

Lastly, it should be noted that the measured data from the meteorological tower reflects the variance over a much smaller area. The rotor disk defined by the span of the blades covers a larger area and may benefit a lower variance perceived by the rotor [69].

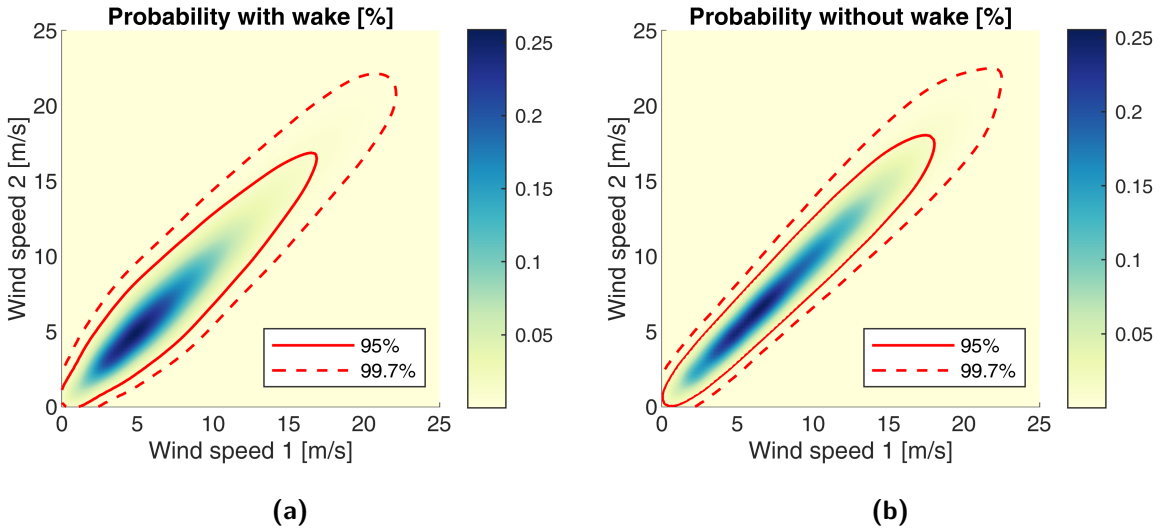

Figure 4-4: The probability distribution map of two wind speeds for both (a) wake and (b) no wake. The boundaries of the 95%- and 99.7%-probability interval are shown in both maps.

4-3-2 Maximum power production

The way DOT wind turbines produce power is distinctly different from conventional solutions; power is generated collectively, rather than individually. Consequently, the maximum power production of the DOT wind farm differs from a conventional wind farm. A prediction of the maximum power production is obtained by finding a relationship between the varying wind speeds, collective hydraulic torque, and power production.

The varying wind speeds are approached by the minimum and maximum wind speed, the wind extrema, in the wind farm. It is assumed that intermediate wind speeds do not significantly alter the shape of the overall performance. Accounting only for the wind extrema allows the convenient simplification to a relation between only two wind speeds and one hydraulic torque to a power production.

The NREL 5-MW reference turbine is used as a baseline for the DOT wind turbine. All wind turbine properties are considered to be equal, although the gearbox and its effects are removed. Similar to the maximum power production of the NREL 5-MW reference turbine, it is assumed initially that the shape of the maximum power production correlates mainly to the optimal wind capture. Therefore, all drivetrain characteristics and dynamics are neglected. Furthermore, the derivation only considers steady-state operation points and thus only reflects a static relation.

The derivation of the static maximum power production

The definition of the static maximum power production is obtained by considering two static wind speeds $V_{\mathrm{l/h}}$ and a hydraulic torque τ_i. The required torque coefficients are then given by

$$C_{\tau,\mathrm{l/h}} = \frac{\tau_i}{\frac{1}{2}\rho\pi R^3 V_{\mathrm{l/h}}^2}. \tag{4-5}$$

If the required torque coefficient exceeds the torque coefficient map, shown earlier in Figure 3-4, the wind turbine is not able to operate and does not produce power. Otherwise, the highest tip-speed ratio that provides the required torque coefficient is taken. This tip-speed ratio leads to the highest attainable rotor speed $\omega_{l/h}$ and so maximizes the mechanical power

$$P_{\mathrm{m,l/h}} = \tau_i \omega_{l/h}, \tag{4-6}$$

where the rotor speed is limited to the maximum rotor speed. The power production for the two wind speeds and hydraulic torque is simply the summation of the mechanical power.

The power production is determined following the aforementioned logic for every combination of wind speeds, from the cut-in to cut-out wind speed, and hydraulic torque, from the cut-in to maximum shaft torque. Hereafter, the maximum of the power production is taken for every combination of wind speeds. This method results in the heat map of the static maximum power production shown in Figure 4-5a.

Accounting for wake effects in the control strategy is not included in the scope of this thesis and therefore only the undisturbed wind data is used. For purposes of simplicity, the derivation of a control strategy focuses on the 95%-probability interval, indicated by the red line in Figure 4-5a. The dashed lines show the boundary where two turbines are in operation. Outside this boundary, along the axes, the maximum power production is obtained by taking a torque that only one wind turbine can attain.

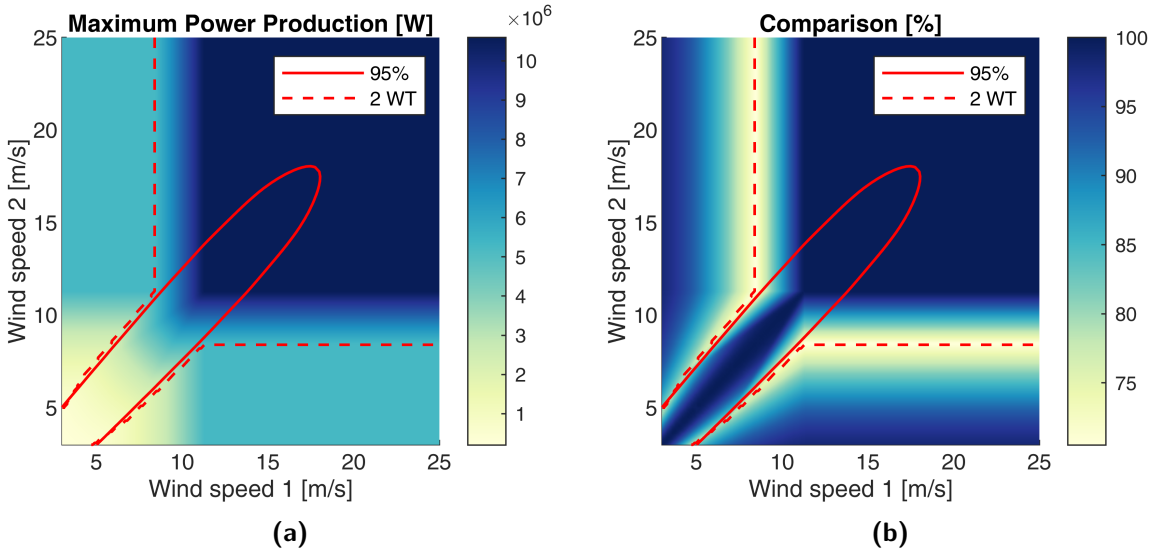

Figure 4-5: The definition of (a) the maximum power production for the DOT wind farm and (b) how this compares to the wind capture of two NREL 5-MW reference turbines. The red line indicates the 95%-probability interval. Two wind turbines are in operation between the dashed red lines, whereas it is more efficient to stop the wind turbine with lower wind speed outside these boundaries.

Figure 4-5b compares the maximum power production of the DOT wind farm to that of a conventional wind farm, employing two NREL 5-MW reference turbines. This reflects the efficiency of wind capture as a result of deviation from optimal torque to facilitate both wind turbines.

Figure 4-5b shows that along the diagonal, the power production is quite comparable to conventional wind turbines. When moving towards the limits of the 95%-probability interval in below-rated conditions, the efficiency deteriorates rapidly. Outside the boundary of this interval, the efficiency drops to 70% at the dashed boundary. Within the boundaries, both wind turbines are in operation. Outside the dashed boundary, it is theoretically more beneficial to stop the wind turbine with lower wind speed from operation. Consequently, the line pressure can be increased and the other wind turbine produces more power than the combined power at a shared, lower line pressure.

The increasing efficiency towards the axes can be explained by the fact that along the axes, the contribution of the wind turbine operating at a lower wind speed is minimal. To illustrate this effect, assume a wind turbine at cut-in and the other at rated conditions. The power production is 5.3 MW (1 rated power, 1 standstill), whereas conventional turbines produce 5.4 MW (1 rated power, 1 cut-in power), resulting in a wind capture efficiency of 98%.

Particularly at the transition from below- to above-rated, the efficiency shows a critical bottleneck. This effect is explained as follows. In below-rated conditions, a difference in wind speed prevents the pressure from rising to the optimal pressure of the highest wind speed. Consequently, the wind turbine that perceives the highest wind speed, is allowed to accelerate as it is well below the rated rotor speed. As such, it is still able to gain captured power, notwithstanding that the rotor efficiency decreases. In near-rated conditions, a similar logic applies but contrarily operates near the rotor speed. Henceforth, the wind turbine is not able to accelerate and has to pitch away to maintain maximum rotor speed. Evidently, this results in a loss of capture wind power compared to conventional solutions.

An illustration of the operating points of the wind turbines

To illustrate the wind turbine behavior that obtains maximum power production, Figure 4-6 shows the operating points of the wind turbines for several combinations of wind speeds. First, Figure 4-6a demonstrates clearly that both wind turbines have optimal performance if wind speeds are equal.

Figure 4-6b and Figure 4-6c illustrate the mechanism for maximum power production when wind speeds deviate. The wind turbine with lower wind speed reduces the tip-speed ratio and thereby increases the torque coefficient at the cost of the power coefficient. The wind turbine with higher wind speed increases tip-speed ratio and reduces the torque coefficient faster than the power coefficient, facilitating a reduced torque that the other wind turbine can sustain.

Lastly, Figure 4-6d shows that near rated conditions, the efficiency of the wind turbine with higher wind speed is slightly higher. This illustrates the fact the wind turbine with higher wind speed is able to contribute exponentially more to the power production and is, therefore, more influential in maximizing.

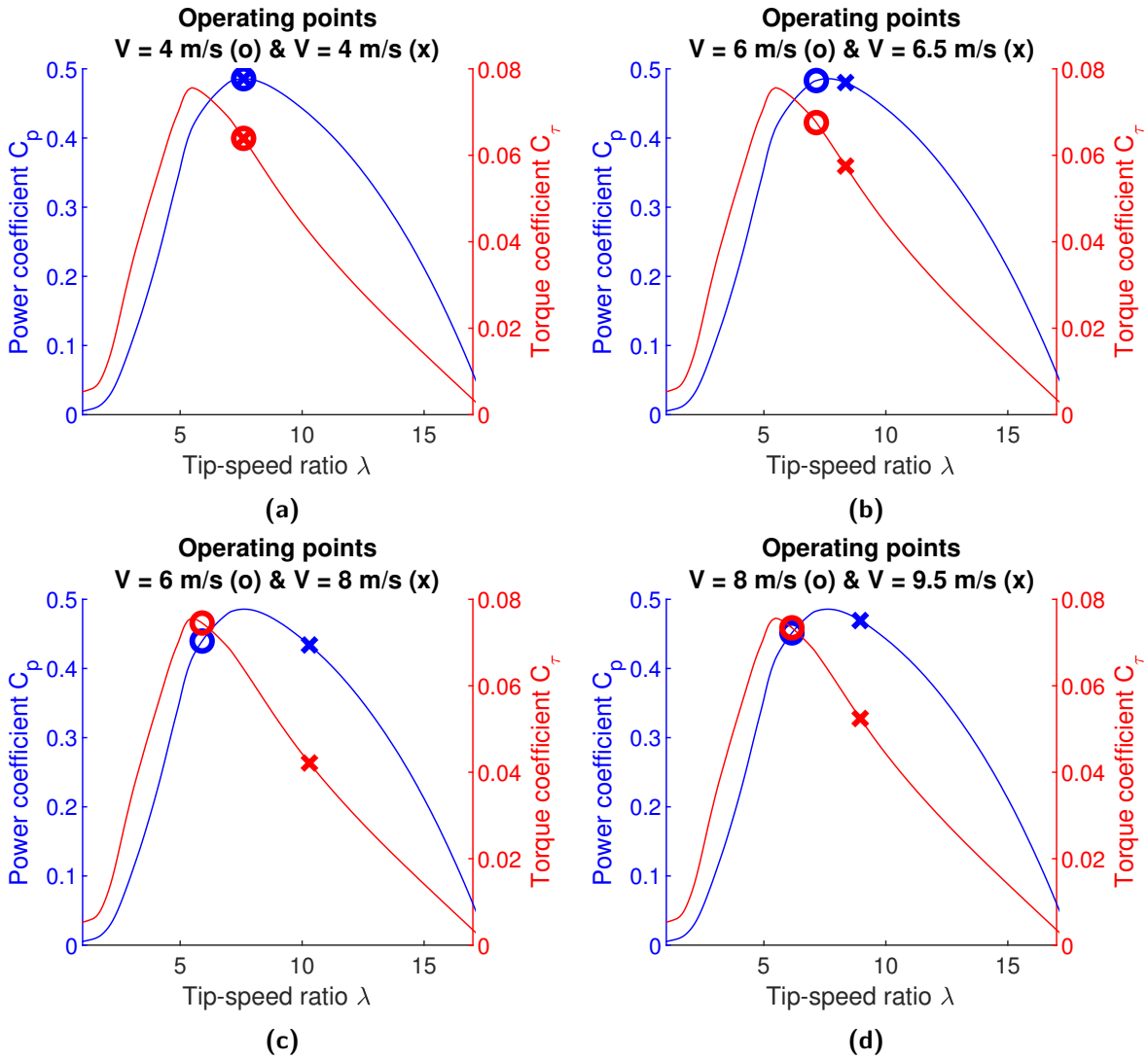

Figure 4-6: The operating points of the wind turbines for a combination of wind speeds that yield maximum power production. For equal wind speeds, both wind turbines operate at their optimal power coefficient. When the wind speeds deviate, the wind turbine with lower wind moves to the left of the optimal point reducing the power coefficient but increasing the torque coefficient. The wind turbine with higher wind speeds moves to the right of the optimal point reducing both power and torque coefficient.

4-3-3 Control strategy DOT

For above-rated conditions, conventional pitch control with passive spear valve control can be implemented as derived for the DOT500 [28]. Compared to conventional wind turbines, the DOT wind farm requires below-rated torque control that takes into account two wind speeds. As mentioned in the previous section, particularly when either wind speed reaches rated conditions in the transition region, torque control is critical.

For below-rated hydraulic torque control, several strategies were tested for their effectivity in pursuing the maximum power production:

- Strategy 1
  The first strategy follows the principle of optimal torque tracking based on the highest wind speed in the wind farm. The other wind turbine tries to keep up, unless its maximum aerodynamic torque is surpassed and eventually comes to a standstill. Figure 4-7a shows that this strategy is particularly effective around the diagonal. However, the wind turbine with the lowest wind speed comes to a standstill when shifting from the diagonal and the efficiency severely drops to 50%.

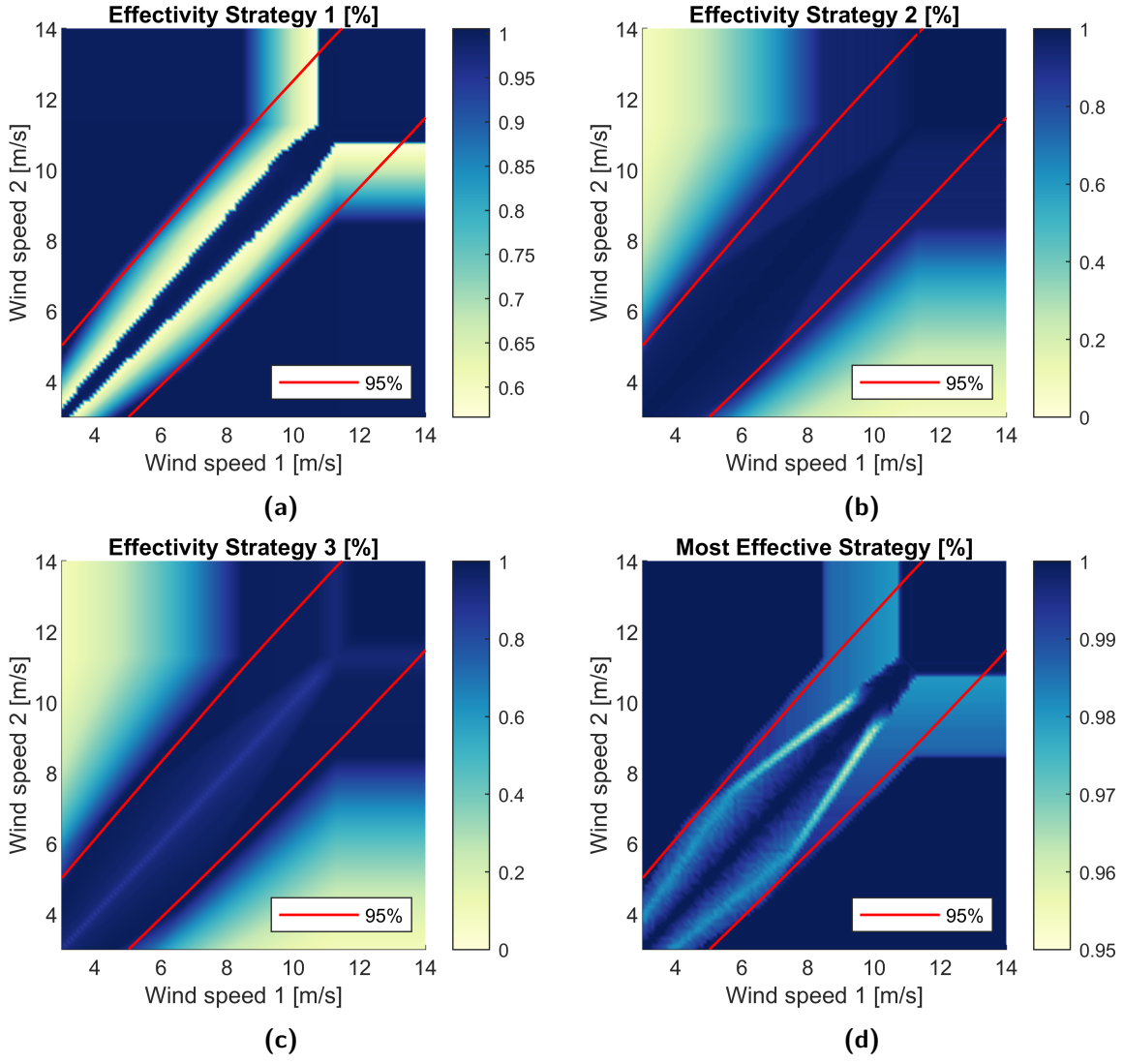

Figure 4-7: The extent to which (a) control strategy 1, (b) control strategy 2, and (c) control strategy 3 can capture the static maximum power production. Control strategy 1 & 2 track the maximum power coefficient based on the highest and lowest wind speed respectively. Control strategy 3 tracks the maximum torque coefficient based on the lowest wind speed. The (d) maximum of control strategy 1, 2 & 3 combined attains 95% or more of the static maximum power production. The 95%-probability interval boundary is given by the red line.

- Strategy 2
  Figure 4-7b shows a similar strategy, but rather bases the optimal torque on the lowest wind speed. The wind turbine with the highest wind speed is allowed to accelerate until it reaches its maximum rotor speed. The second strategy improves the performance in the off-diagonal region. Still, this strategy is not very effective near rated conditions.

- Strategy 3
  The third strategy tracks the maximum torque of the wind turbine with the lowest wind speed. Again, the other wind turbine is allowed to accelerate until its maximum rotor speed. Figure 4-7c covers the area in near-rated conditions with acceptable efficiencies, except for the diagonal. This effect is the result of pursuing the highest torque and thereby suboptimal power production, even if both rotor speeds are equal.

It can be concluded that each strategy outperforms its peers in a selected region and neither of the strategies performs particularly well overall with respect to the maximum power production. Taking the maximum of all three strategies yields the efficiency displayed in Figure 4-7d. It shows that the overall efficiency of the combined strategies is acceptable and varies between 95% and 100% of what is technically achievable. Which strategy is utilized, is displayed in Figure 4-8a.

Altogether, there is no conclusive analytical relation between optimal power production and optimal system torque, like for conventional below-rated torque control. The employment of a combination of aforementioned control strategies requires a switching logic between strategies and may over-complicate the implementation.

In the absence of a simplistic strategy that perseveres, the initial strategy was chosen as a simplistic optimal torque look-up table, shown in Figure 4-8b. Although conventional wind speed measurements often do not accurately reflect the actual wind speed, modern

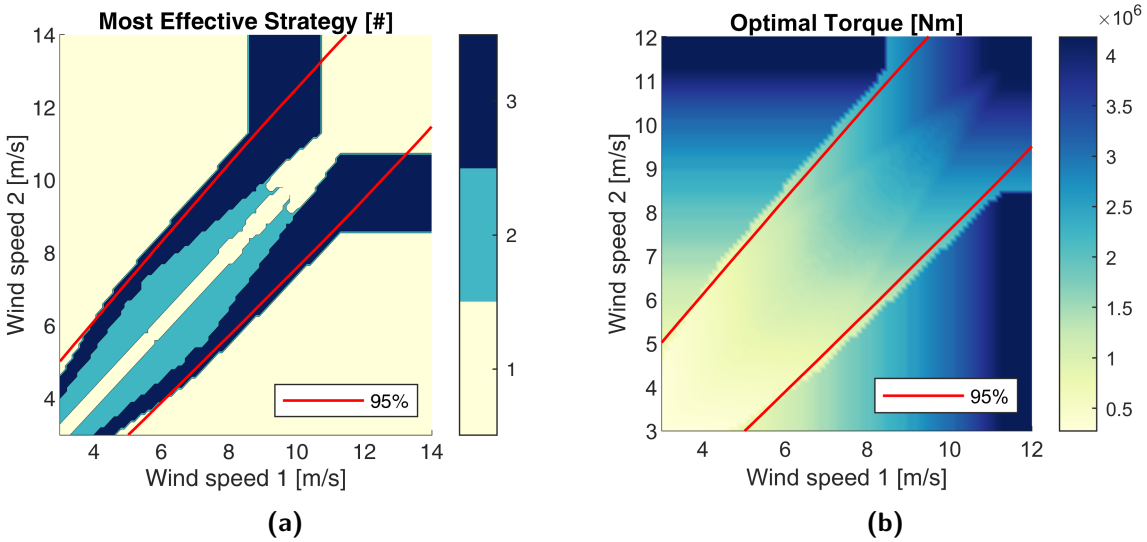

Figure 4-8: The (a) control strategy that most effectively obtains the static maximum power production and (b) the optimal torque that corresponds to the static maximum power production. The 95%-probability interval boundary is given by the red line.

methods exist that make accurate estimations of the wind speed [69]. Furthermore, innovative measurement systems are developed, such as Light Detection And Ranging of Laser Imaging Detection And Ranging (LIDAR) [70][71]. It is assumed that in the near future, technology is available to have accurate wind speeds. Consequently, this strategy maps the extremes of the wind speeds to an optimal pressure.

Chapter 5

Numerical Model

The goal of this chapter is to develop a numerical model to reflect the dynamics of a seawater-hydraulic Delft Offshore Turbine (DOT) wind farm configuration, with fixed displacement pumps. The theoretical knowledge from Chapter 3 is implemented in a commercially available high-fidelity simulation software package Simulink to obtain numerical simulation results.

This chapter starts with a general overview of the numerical model in Section 5-1. Thereafter, Section 5-2 describes the individual components and lays out the assumptions made in the design of not yet commercially available components. Section 5-3 elaborates on the control design of subsystems and performs an analysis on the system stability using Kharithonov's stability theorem. Section 6-1 concludes this chapter with a brief description of the simulations.

5-1 An overview of the numerical model

A general overview of the numerical model is illustrated in Figure 5-1. A distinction is made between the type of wind farm: NREL or DOT. The former refers to a wind farm employing the NREL 5-MW reference turbine, following the definition given in [34] and is not described in this thesis. The latter refers to the seawater-hydraulic wind farm with fixed-displacement pumps interconnected through a collective hydraulic network. The aforementioned terminology is used in the remainder of this thesis.

The DOT wind farm follows the same sequence of energy conversion and transmission as introduced earlier in Chapter 3. In Figure 5-1 however, the rotor model and hydraulic pump are combined into the DOT wind turbine block. Furthermore, the electrical generator is incorporated in the Pelton turbine block. A description of the physical components and corresponding controllers is given in the remainder of this chapter.

Both wind farms consist of only two wind turbines that reflect the minimum and maximum wind speed encountered throughout an actual wind farm. It is assumed that other potential wind turbines with intermediate wind speeds, do not have a significant influence on the operation of the wind farm.

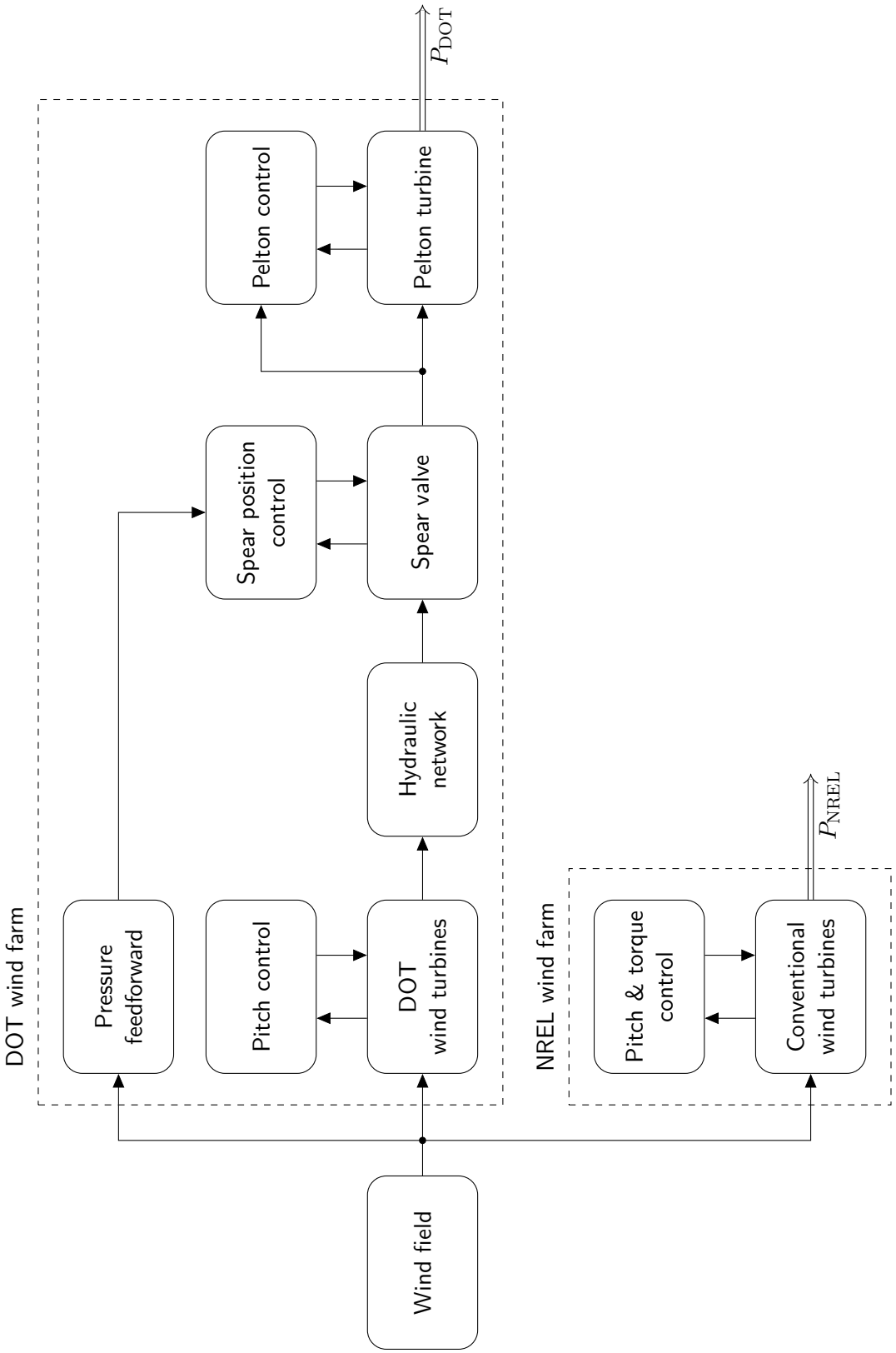

Figure 5-1: The schematic overview of the components and controllers in the numerical model. A distinction is made between the DOT wind farm and a wind farm employing the NREL 5-MW reference turbine, referred to as the NREL wind farm [34].

5-2 Component description

This section describes how the components employed in the DOT wind farm are modelled. Some components in the full-scale implementation do not yet exist and are derived following a simplified modelling approach based on the governing principles explained in Chapter 3. The components are parametrized to reflect the real-world component behavior as close as possible.

5-2-1 Wind field

The wind speed for each wind turbine is determined in the first block of Figure 5-1. This is given by either a constant or time-varying wind speed, depending on the type of simulation. The time-varying wind data is obtained from former wind farm simulations using the Parallelized Large-eddy simulation Model (PALM): an open-source model based on the non-hydrostatic, filtered, and incompressible Boussinesq approximation of the three-dimensional Navier-Stokes equations [72][73]. This model is typically used to analyze the evolution of turbulence and wake effects in the wind field of a wind farm. In this research, the resulting wind field data was used as it accurately reflects the time-varying composition. While the original model entailed six wind turbines, only the wind data just before the first row of wind turbines is used and thereby excludes wake effects from other wind turbines.

5-2-2 Wind turbine

The wind turbine is modeled by a simple first-order rotor model [64]

$$\dot{\omega}_{\mathrm{r}} = \frac{1}{J_{\mathrm{r}}}(\tau_{\mathrm{aero}} - \tau_{\mathrm{sys}}) \tag{5-1}$$

where ω_{r} is the rotor speed, J_{r} the combined rotor inertia, τ_{aero} the aerodynamic torque and τ_{sys} the system torque. The combined rotor inertia entails the rotor blades, hub, rotor shaft and hydraulic pump.

The aerodynamic torque is given by Eq. (3-5). A two-dimensional look-up table with linear interpolation is used to determine the torque coefficient. The look-up table uses the data from the NREL 5-MW reference turbine, as shown earlier in Figure 3-4 [34].

Lastly, the system torque is given by the hydraulic torque of the pump. The hydraulic torque is calculated from the rotor speed and the pump discharge pressure, following Eq. (3-12). The properties of the seawater-hydraulic pump are derived in the next subsection.

5-2-3 Seawater-hydraulic pump

The seawater-hydraulic pump is part of the main feature that the DOT introduces, but is commercially not yet available. The hydraulic parameters derived in earlier work are assumed, as stated in Appendix A [5]. The NREL 5-MW reference wind turbine is taken as the baseline for a simplistic pump design. Therefore, assume the pump is driven by a mechanical shaft

power $P_{\text{mech}} = 5.3$ MW at an angular speed of 12 RPM. Lastly, assume the seawater-hydraulic pump operates in rated conditions at a pressure of 180 bar to minimize kinetic losses. The required volumetric displacement then becomes

$$D_{\text{h}} = \frac{1}{(1 + C_{\text{f}})\Delta p} \left(\frac{P_{\text{mech}}}{\omega_{\text{r}}} - \xi_{\text{p}} \omega_{\text{r}} \right) = 0.22\,\text{m}^3/\text{rad}. \tag{5-2}$$

This results in a nominal flow of

$$Q_{\text{nom}} = \omega_{\text{r}} D_{\text{h}} - C_{\text{p}} \Delta p = 0.27\,\text{m}^3/\text{s}. \tag{5-3}$$

5-2-4 Hydraulic network

The flows generated in the wind turbines flow through two initial pipelines to a collective pipeline, as shown in Figure 5-2. Each pipeline is modelled following the dynamics described in Section 3-3. This model follows a lumped parameter approach and its accuracy is thereby subject to the number of segments in the model. The derivation of a single-element was outlined in the aforementioned section; a derivation of a double-segment pipeline can be found in Appendix B.

The derived models for a rigid pipeline of length $L = 1000$ m, diameter $d = 0.5$ m, nominal flow and varying segments, give the Bode magnitude plot from output to input pressure shown in Figure 5-3 and the system pole-zero map in Figure 5-4a. Both images clearly show that adding segments increases the accuracy of the model by including more resonance peaks and improving the location of preceding resonance peaks. When adding a segment, particularly the location of the previously added resonance peak shows visible improvement. Lastly, it can be seen that although additional segments shift the complex conjugate poles from the real axis, their negative real part remains unchanged.

Furthermore, the pipeline length is a prominent variable in the resonance frequency and damping ratio [13][44]. Figure 5-4b and Figure 5-5 demonstrate its effect for a rigid single-element pipeline of diameter $d = 0.5$ m and nominal flow. As the length increases, the

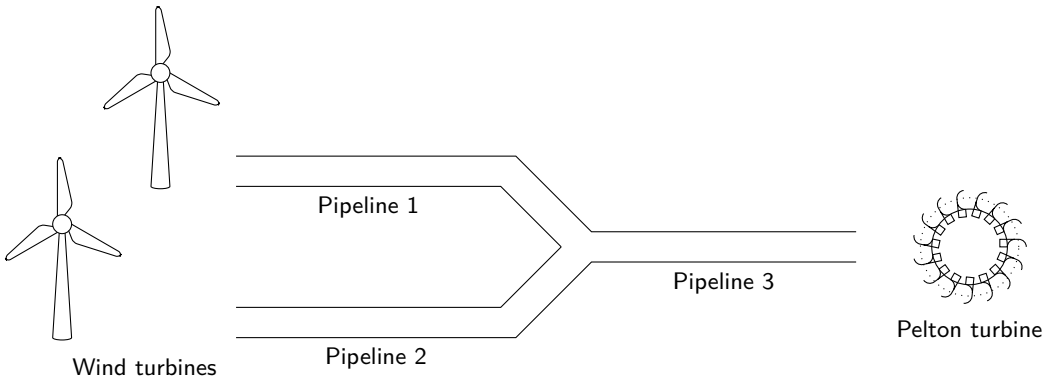

Figure 5-2: The flows generated in the wind turbines go through two initial pipelines, 1 and 2, to a collective pipeline 3. The spear valve at the end of pipeline 3 exerts a pressure on the preceding pipelines.

resonance peak shifts to lower frequencies in the Bode diagram. The system pole-zero map underlines this as the complex conjugate poles shift towards the real-axis. Moreover, it shows that the negative real part of the complex conjugate poles is not affected by the length of the pipeline. Lastly, the distance from the system poles to the origin decreases, meaning that the damping ratio increases, which is also seen by the diminishing intensity of the peaks in Figure 5-5.

Lastly, the effects of the nominal flow through the pipeline are investigated. The system pole-zero map is shown in Figure 5-6. The flow of 0.07 m^3/s refers to cut-in conditions and 0.27 m^3/s to rated conditions. In contrast to previous parameters, the negative real parts of the pole-zero locations are highly affected by the flow. While the complex parts and thus

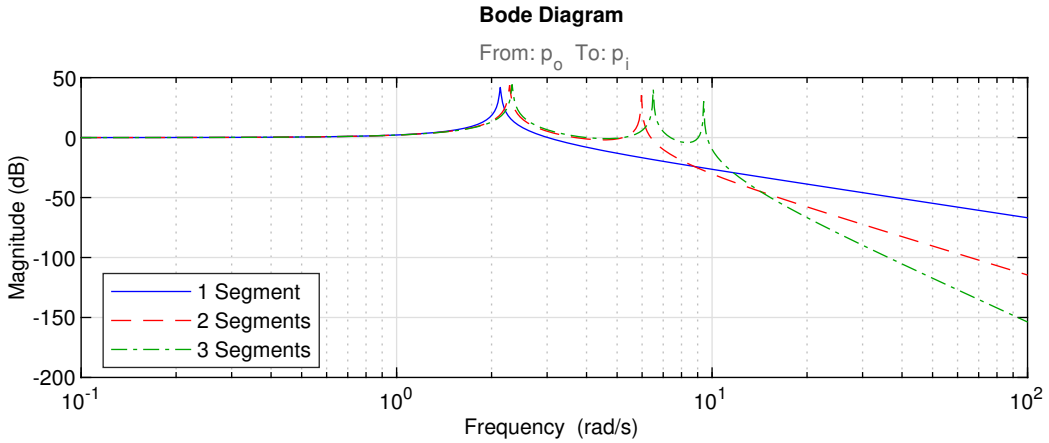

Figure 5-3: Influence of the number of segments on the Bode magnitude from output pressure to input pressure.

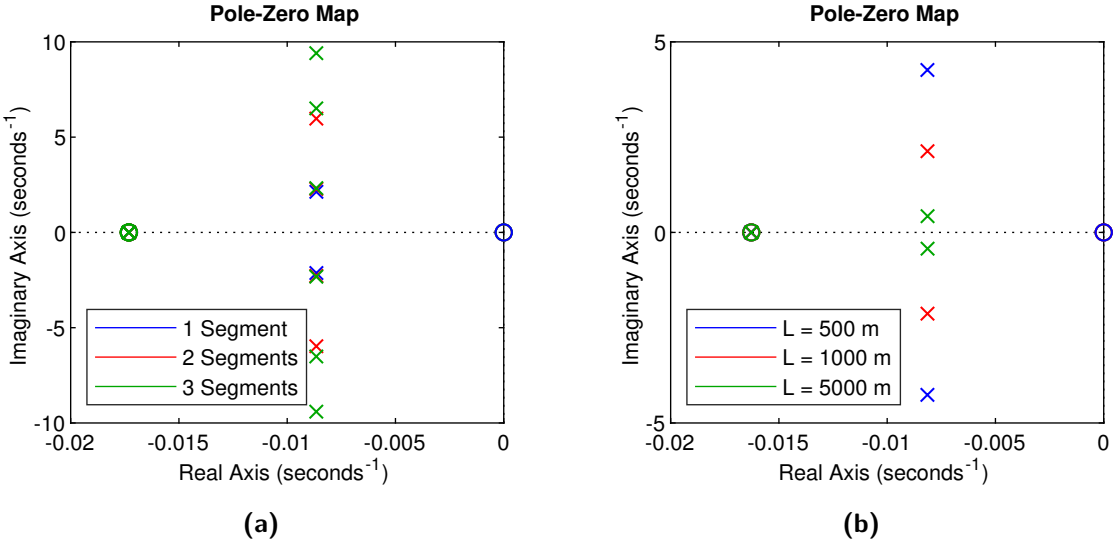

Figure 5-4: The influence of the number of segments (a) and pipeline length (b) on the poles (x) and zeros (o) of the system. The poles and zeros on the real axis coincide and only show a single color.

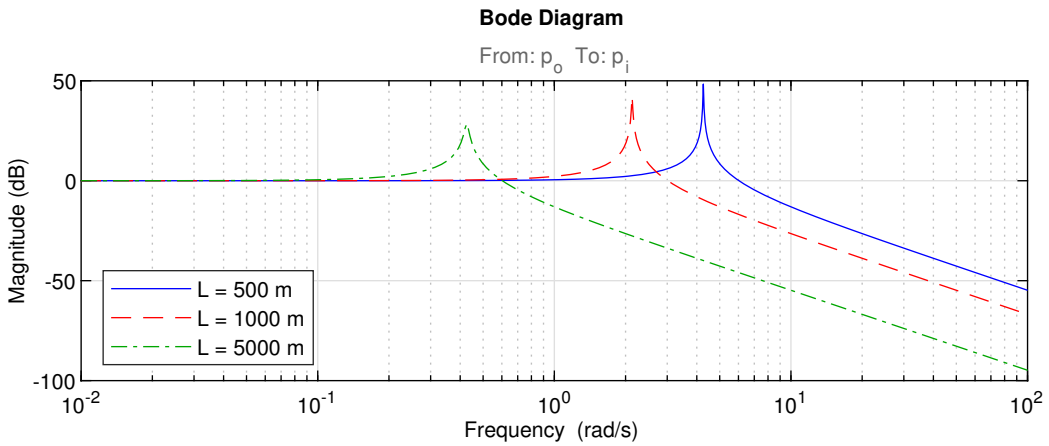

Figure 5-5: Influence of the pipe line length on the Bode magnitude from output pressure to input pressure.

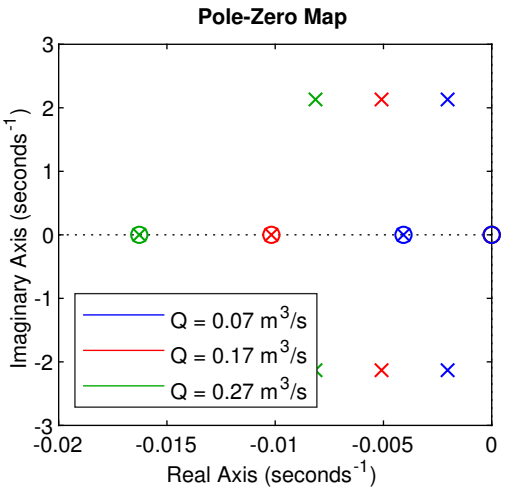

Figure 5-6: The influence of the nominal flow through the pipeline on the poles (x) and zeros (o) of the system. The zeros located at the origin coincide and only show a single color.

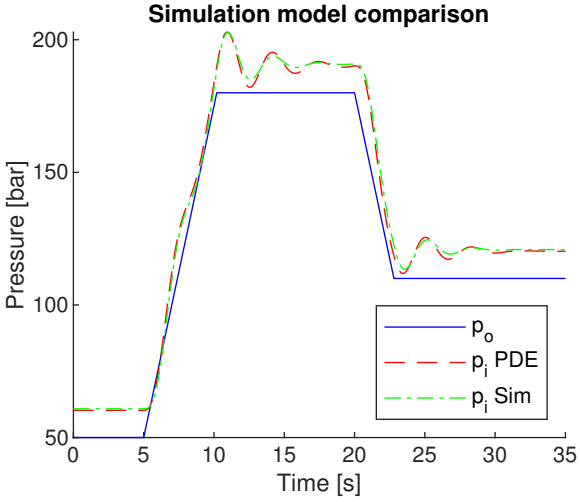

Figure 5-7: A rate-limited step response on the output pressure results in similar input pressures from the numerically derived model (PDE) and the Simscape Fluids model (Sim).

the natural frequency remains unaltered, the damping ratio is severely impacted. It is shown that the damping decreases for lower flows, meaning that the system has the lowest damping at cut-in conditions.

The Simscape Fluids toolbox allows modelling of hydraulic components in the high-fidelity software package Simulink [74]. The numerically derived single-element pipeline of Section 3-3 is compared to the segmented pipeline from this toolbox. Figure 5-7 shows that the Simscape Fluids elements adequately capture the dynamics. Additionally, the toolbox allows easy manipulation of the number of segments or interconnection of pipelines. Consequently, the Simscape Fluids toolbox is used to model the hydraulic network in the eventual simulations.

Based on the findings described above, and to limit computation times, three segments are

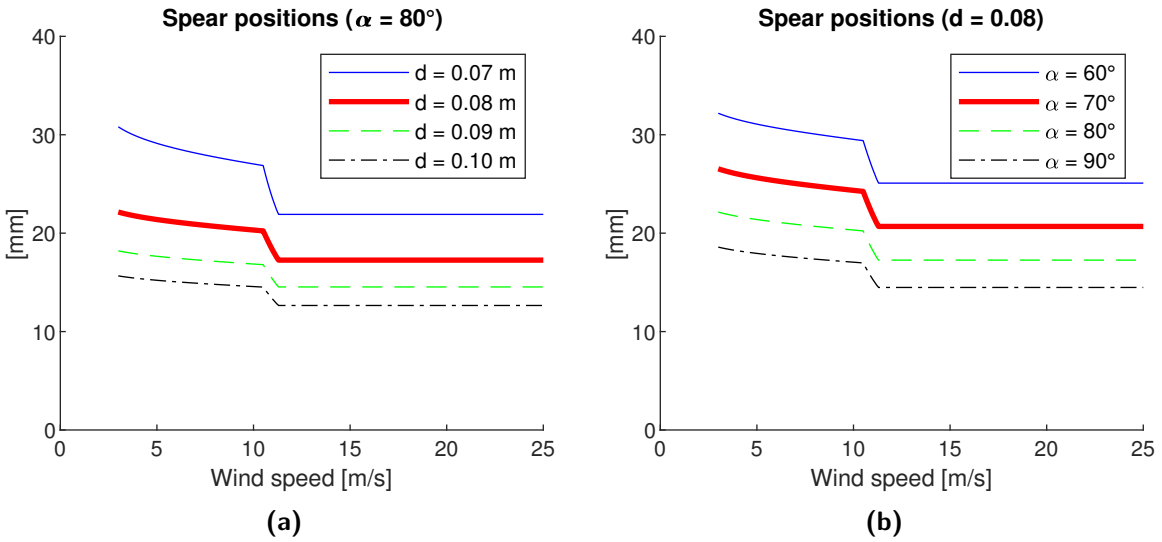

Figure 5-8: The influence of (a) the nozzle diameter and (b) the spear tip angle on the desired spear position per wind speed.

chosen to adequately capture the dynamics of each pipeline. The length of pipelines is primarily dictated by the distance between wind turbines, which in turn is entirely subject to the design of the wind farm. Based on the data available from the Offshore Windpark Egmond aan Zee (OWEZ), the length of each pipeline is predicted at 1000 m [66]. It should be stated that this is likely an overestimation of the eventual sizes of the pipelines and may therefore unnecessarily limit the control bandwidth for spear valve actuation.

5-2-5 Spear valve

The NREL 5-MW reference turbine model is used as baseline to aid in the initial design of a spear valve. Its optimal rotor speed and mechanical shaft torque per wind speed, are related to a flow and pressure respectively following the relations in Chapter 3-2. Following the dynamics described in Section 3-4, this translates to a desired spear valve position.

The nozzle diameter and spear tip angle of the spear valve are varied to display the influence of the respective parameter on the desired spear position in Figure 5-8. Firstly, Figure 5-8a shows that larger diameters have less variance in the desired spear position. Figure 5-8b exhibits a similar effect for increasing spear tip angles. The lower variance in the desired spear position means that less spear actuation is required. Simultaneously, the spear position sensitivity with respect to the line pressure increases. The increased sensitivity translates to a highly precise actuation of the spear position, that may not be possible in the physical world. Ultimately, the choice of aforementioned parameters boils down to a trade-off between required actuation of the spear position and the sensitivity of the spear position with respect to the line pressure.

Initially, the spear valve is designed with a nozzle diameter of 0.08 m and spear tip angle of 80°. The desired spear position for this spear valve then ranges from 17.3 mm to 22.1 mm. In earlier research, the spear position was actuated at 0.44 mm/s with a precision of 0.05 mm [28].

A similar actuator is assumed in this research and is able to cover the entire range of the spear valve in roughly 10 seconds.

5-2-6 Pelton turbine

The last block in the series of physical components encompasses both the capture of hydrokinetic energy by the Pelton wheel and the conversion to electrical energy by the electrical generator. The efficiency of the Pelton turbine is calculated by Eq. (3-45), which depends on fixed parameters and the peripheral speed coefficient. An estimation for the latter is provided in the next section. Lastly, the electrical power produced by the electrical generator is given by Eq. (3-49). The generator efficiency is considered to be equal to the electrical generator of the NREL 5-MW reference turbine [34].

5-3 Controller design

With a definition of all physical components, only the definition of the blocks corresponding to the controllers in Figure 5-1 remain. This section describes all controllers in the order of which the controlled variable occurs in the sequence of the physical components.

5-3-1 Pitch controller

The gain-scheduled PI controller defined for the NREL 5-MW reference wind turbine is used for pitch control [34]. Slight modifications are made to accommodate for the absence of a gearbox and generator in the DOT wind turbine. The values referring to a generator speed, are adjusted to the rotor speed by excluding the gearbox ratio. Likewise, the high-speed shaft torque is modified to give the rotor shaft torque.

The rotor speed is used as input for the controller, while the measured pitch is used for the scheduling of the control gains. Lastly, the rotor shaft torque is used to improve the switching logic between below- and above-rated conditions.

5-3-2 Spear valve controller

The spear valve provides resistance to the outgoing flow and in doing so pressurizes the flow originating from the seawater-hydraulic pumps. The resulting pressure depends on two variables: the outgoing flow and the nozzle area. The former is imposed by its predecessors, but the latter is controlled by the spear position. Active manipulation of the spear position is referred to as active spear valve control.

The spear valve control scheme constitutes of two elements, as shown in Figure 5-1. Firstly, the optimal pressure is determined by a feedforward pressure controller as discussed in Chapter 4. The minimum and maximum wind speed in the wind farm are mapped to a single output pressure using a two-dimensional look-up table with linear interpolation. Consequently, the spear valve controller is tasked with actually obtaining the desired output pressure.

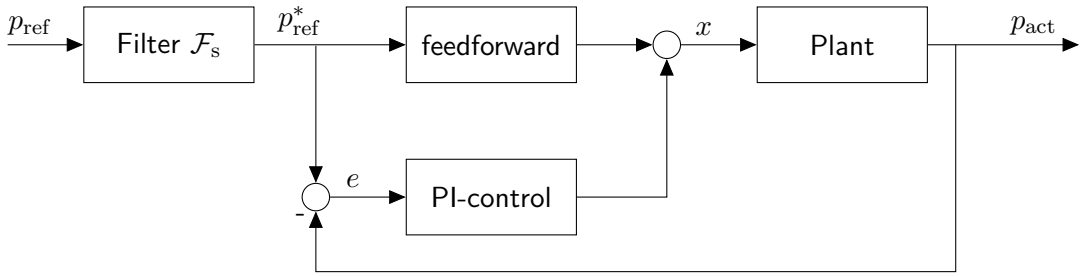

Figure 5-9: An illustration of the spear valve controller: the reference pressure is filtered by $\mathcal{F}$ and a combination of a feedforward- and feedback PI-control determines the desired spear position.

The scheme of the spear valve controller derived in earlier work as introduced in Chapter 2, is implemented [5][36]. This controller consists of a series of filters to secure a reference pressure that does not induce water hammer effects. Subsequently, a combination of feedforward feedback control, as illustrated in Figure 5-9, is used to determine the spear valve position. The feedforward control action is given by an orifice compensator; an inverse model of the spear valve determines the theoretical spear position based on the current flow and desired pressure. This spear position is augmented with a control action from a PI controller to account for parameter deviations in the inverse model.

Derivation of filters

A state space representation of the hydraulic network illustrated in Figure 5-2, is derived numerically for single-element pipelines. For the synthesis of the filters, the worst-case flow is assumed, thus the least damping at cut-in conditions.

The Bode plot of the combined hydraulic network is shown in Figure 5-10a. From Figure 5-3, it is known that the two resonance peaks in Figure 5-10a are followed by more resonance peaks. Therefore, a low-pass filter is applied on the desired output pressure. Furthermore, notch filters are added to reject the first resonance peaks. The addition of notch filters smooths out the resonance peaks and allows a higher corner frequency of the low pass filter. The combination is given by [75]

$$\mathcal{F}_{\text{s}}(s) = \mathcal{L}_{\text{s}}(s)\mathcal{N}_{\text{s1}}(s)\mathcal{N}_{\text{s2}}(s) = \frac{\omega_{\text{lp}}}{s+\omega_{\text{lp}}}\frac{s^2+\zeta_{\text{n1}}s+\omega_{\text{n1}}^2}{s^2+\zeta_{\text{d1}}s+\omega_{\text{n1}}^2}\frac{s^2+\zeta_{\text{n2}}s+\omega_{\text{n2}}^2}{s^2+\zeta_{\text{d2}}s+\omega_{\text{n2}}^2}. \tag{5-4}$$

The parameterization of the filters is based on Figure 5-10a and is specified in Table 5-1. The combined Bode diagram of the filter is shown in Figure 5-10b.

Derivation of the controller

The feedforward controller uses the same equations from Section 3-4 as the spear valve model, resulting in a perfect orifice compensator in the numerical model. This omits the immediate need for a PI controller. Therefore, the synthesis of a PI controller is neglected in the work of this thesis. To reflect the influence of the PI controller in an stability analysis however, the

gains are taken as $K_\mathrm{p} = -2.78 \cdot 10^{-10}$ m/Pa and $K_\mathrm{i} = -1.06 \cdot 10^{-10}$ m/Pa based on the work described in [5].

5-3-3 Pelton turbine controller

The derivation of a controller for the Pelton turbine is highly dependent on its parameters, such as the pitch circle diameter or rated angular speed. This key component does not yet commercially exist and its design to obtain specific parameters lies outside the scope of this thesis.

It is known however that the Pelton performs optimally at a peripheral speed coefficient of roughly 0.5. The control of the Pelton turbine is approximated by applying a first-order actuator model

$$G_\mathrm{pt}(s) = \frac{1}{\tau_\mathrm{pt} s + 1} \tag{5-5}$$

on the optimal speed based on this peripheral speed coefficient, with an estimated time constant $\tau_\mathrm{pt} = 3$ s.

5-4 Controller stability analysis

The pitch controller is refrained from a stability analysis as it is not derived in this thesis. Furthermore, a feedforward controller does not affect the system stability. Therefore, the remainder of this section focuses on the stability of the hydraulic network and the spear valve controller.

5-4-1 Kharithonov's theorem

Since a non-linear time-invariant model of the hydraulic network is used, the entire closed-loop system depends on multiple variables, such as flow or line pressure. Kharithonov's theorem can be used to assess the stability of a system with uncertain parameters [76]. This analysis is performed for an interval polynomial of the denominator of the system, shaped as

$$P(s) = a_n s^n + ... + a_2 s^2 + a_1 s + a_0 \tag{5-6}$$

Low-pass filter	corner frequency	ω_lp	1 rad/s
Notch filter 1	corner frequency	ω_n1	1.425 rad/s
	damping numerator	ζ_n1	0 rad/s
	damping denominator	ζ_d1	2.85 rad/s
Notch filter 2	corner frequency	ω_n2	3.175 rad/s
	damping numerator	ζ_n2	0 rad/s
	damping denominator	ζ_d2	6.35 rad/s

Table 5-1: Parametrization of the filters.

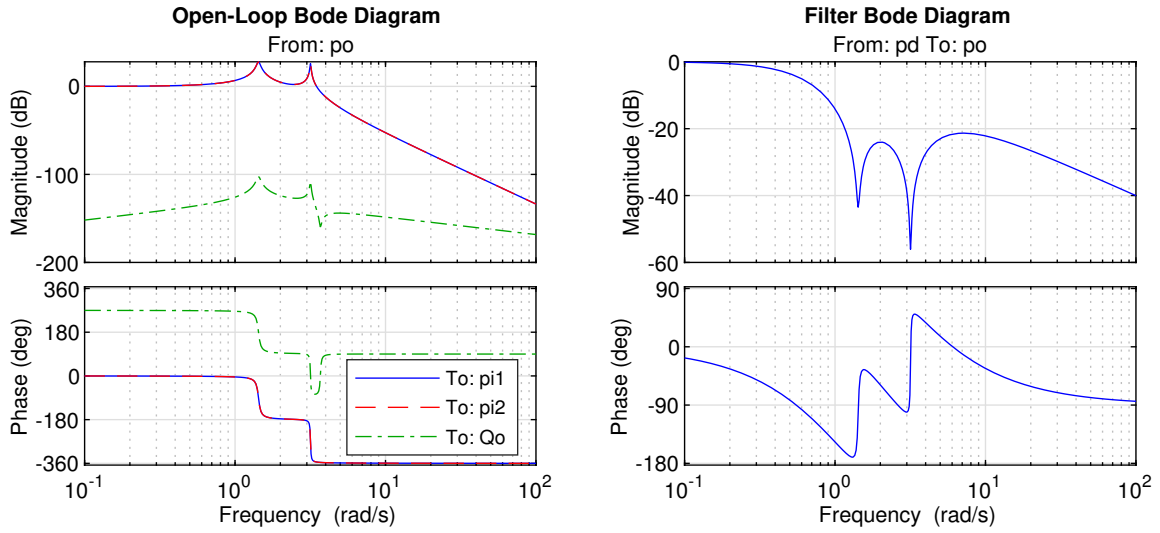

Figure 5-10: The (a) open-loop Bode diagram of two single-element pipelines connected to a collective single-element pipeline at cut-in conditions. The (b) Bode diagram of the combined series of filters from the desired pressure to the actual reference pressure.

where the uncertain coefficients a_n are bound by

$$L_n < a_n < U_n. \tag{5-7}$$

Kharitonov's theorem applies the Routh-Hurwitz criterion to determine stability of the interval polynomial. The Routh-Hurwitz criterion evaluates the stability for a single polynomial by checking the roots of the system. If all roots reside in the left half plane, i.e. have negative real parts, the system is said to be Hurwitz stable.

The Hurwitz stability is evaluated for a set of polynomials called the Kharitonov polynomials, given by

$$\begin{aligned} P_1(s) &= L_0 + L_1 s + U_2 s^2 + U_3 s^3 + L_4 s^4 + L_5 s^5 + \dots \\ P_2(s) &= U_0 + U_1 s + L_2 s^2 + L_3 s^3 + U_4 s^4 + U_5 s^5 + \dots \\ P_3(s) &= L_0 + U_1 s + U_2 s^2 + L_3 s^3 + L_4 s^4 + U_5 s^5 + \dots \\ P_4(s) &= U_0 + L_1 s + L_2 s^2 + U_3 s^3 + U_4 s^4 + L_5 s^5 + \dots \end{aligned} \tag{5-8}$$

If all members of the Kharitonov polynomials are Hurwitz stable, Kharitonov's theorem guarantees that the infinite set of polynomials in the interval polynomial are also stable.

Application of Kharitonov's theorem

The combined transfer function of the filters is already given in (5-4). The transfer function of the PI controller is given by

$$C_{\text{pi}}(s) = K_{\text{p}} + \frac{K_{\text{i}}}{s} \tag{5-9}$$

and the feedforward controller by

$$C_{\text{ff}}(s) = K_{\text{ff}}, \tag{5-10}$$

where $\underline{x}/\overline{p_{\text{o}}} < K_{\text{ff}} < \overline{x}/\underline{p_{\text{o}}}$ with x the spear position and p_{o} the output pressure.

Subsequently, given a flow, three transfer functions $P_{\text{hn1}}(s)$, $P_{\text{hn2}}(s)$ and $P_{\text{hn3}}(s)$ can be derived from the state space of the hydraulic network, mapping the output pressure to the input pressure 1, input pressure 2 and outgoing flow respectively. Lastly, the spear valve actuator is linearized around an operating pressure p_{o} and spear position x. Combined with a first-order actuator model of the spear position, this yields a transfer function from the desired spear position to a pressure

$$P_{\text{sp}}(s) = \frac{\partial p_{\text{o}}}{\partial x}(p_{\text{o}}, x)\frac{1}{\tau_{\text{sp}}s + 1}, \tag{5-11}$$

where the time constant τ_{sp} is chosen at 1.69 based on the work in [28].

Ultimately this yields the set of closed-loop transfer functions

$$\begin{aligned}
P_{\text{pi1}}(s) &= P_{\text{hn1}}(s)\frac{P_{\text{sp}}(s)(C_{\text{ff}}(s) + C_{\text{pi}}(s))}{1 + P_{\text{sp}}(s)C_{\text{pi}}(s)}LP(s)N_1(s)N_2(s) \\
P_{\text{pi2}}(s) &= P_{\text{hn2}}(s)\frac{P_{\text{sp}}(s)(C_{\text{ff}}(s) + C_{\text{pi}}(s))}{1 + P_{\text{sp}}(s)C_{\text{pi}}(s)}LP(s)N_1(s)N_2(s) \\
P_{\text{Qo}}(s) &= P_{\text{hn3}}(s)\frac{P_{\text{sp}}(s)(C_{\text{ff}}(s) + C_{\text{pi}}(s))}{1 + P_{\text{sp}}(s)C_{\text{pi}}(s)}LP(s)N_1(s)N_2(s).
\end{aligned} \tag{5-12}$$

The pressure controller operates primarily in the below-rated region and is therefore evaluated for stability for all pressures at cut-in and rated conditions. It was found that for an interval between 10 bar and 200 bar, the Kharitonov polynomials for each transfer function, are stable.

Figure 5-11 shows the sensitivity function of the closed-loop system for the parameters of several operating points. For all parameters, the sensitivity remains under zero-dB line. If the control gains of the PI-controller are increased, the sensitivity peak rises above 0 dB.

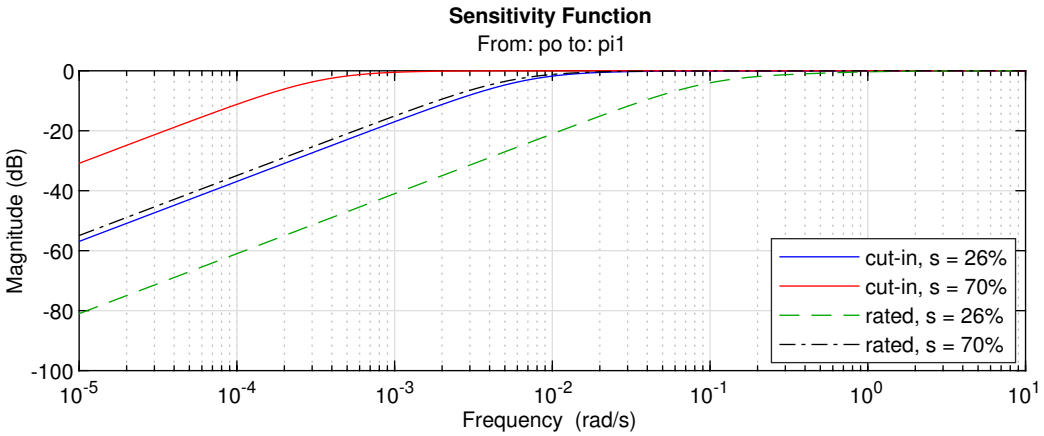

Figure 5-11: The sensitivity function of the closed-loop transfer function.

Chapter 6

Numerical Simulations

The numerical model described in Chapter 5 is used to determine the maximum power production. Moreover, it is used to assess and predict the dynamic performance of the derived control strategy in Chapter 6.

First, Section 6-1 gives a description of the numerical simulations performed on the numerical model. Consecutively, Section 6-2 post-processes the information of the numerical simulations to obtain the simulation results. Section 6-3 discusses the simulation results and verifies the static maximum power production. Lastly, Section 6-4 evaluates the performance of the derived control strategy subject to a wind time series and shows a comparison to a conventional wind farm.

6-1 Description of the numerical simulations

This section discusses the simulations that are run on the numerical model using the model parameters given in Appendix A. The first simulation aims to verify the static maximum power production. The second makes a dynamic comparison between the Delft Offshore Turbine (DOT) and NREL wind farm. Both simulations are subject to several initial and stopping conditions, which are described hereafter.

6-1-1 Verification of the maximum power production

The control strategy derived in Chapter 4 builds entirely on the prediction of the maximum power production and assumes that its shape is mainly determined by the optimal wind capture. The initial prediction neglects all drivetrain characteristics, whereas the numerical model includes all drivetrain characteristics and dynamics. Therefore, a number of simulations is performed to validate the shape of this prediction.

The simulations follow a similar procedure as the initial prediction: two fixed wind speeds are applied on the wind turbines and the simulation is run for several spear positions. The

optimal pressure and corresponding desired spear position derived in the design of the spear valve is used as a baseline. In the case of approximately equal wind speeds, an interval of 20% of the maximum spear position is placed around the baseline spear position. If the wind speeds deviate more than 2 m/s from each other, the interval is extended until the spear valve is fully opened.

6-1-2 Dynamic comparison of wind farm power production

The DOT wind farm ultimately has to compete with a conventional wind farm. A simulation is performed in below-rated conditions to make a power production comparison between the wind farms shown in Figure 5-1. The time-varying wind field described in Section 5-2-1 applies the same wind speed on both wind farms. Lastly, the results of the simulation described above are used to update the optimal pressure map in the pressure feedforward controller.

6-1-3 Simulation conditions

During the development of the numerical model, the initial conditions turned out to be crucial for the functioning and speed of the simulation. If the initial conditions are too far off, this can be considered as a step input on the system. As a result, oscillating behavior from water hammer effects occurs in the simulation. Furthermore, several conditions are added to stop the simulation in the event of a physically infeasible situation. All conditions facilitate a shorter computation time of the simulation and are further described in Appendix C.

6-2 Post-processing of numerical results

The objective of the first simulation is to determine the maximum power production and corresponding optimal pressure and spear valve position. As described above, several spear valve positions are considered for each combination of wind speed and range from slightly below to above of their calculated optimal value. Eventually, this is used to verify whether the maximum power production correlates mainly with the optimal wind capture, or that the wind farm characteristics and dynamics alter the optimal performance considerably.

The simulations are performed for a finite set of wind speeds and spear valve positions. Figure 6-1 presents an insight into the relation between spear valve position and produced power for a given wind speed combination. Since the set of simulations is finite, the results may innately exclude the exact optimal value. Therefore, an ordinary least-squares approach is used to fit a parameterizable polynomial to the obtained data. The analytical relation is consequentially used to find the maximum power and its corresponding spear valve position.

The relation between the output power P_{out} and spear valve position s is estimated by the fourth-order polynomial

$$P_{\text{out}}(s) = \beta_4 x^4 + \beta_3 x^3 + \beta_2 x^2 + \beta_1 x + \beta_0 \tag{6-1}$$

where β_i represent the unknown coefficients and x the spear position.

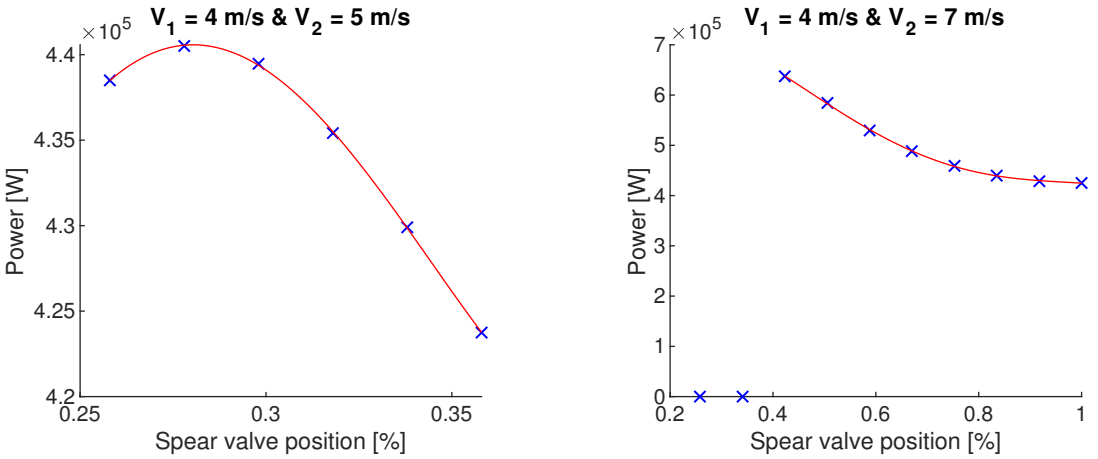

Figure 6-1: The data points (blue) of power production for several spear valve positions at a given combination of wind speeds. An ordinary least squares estimation (red) is fitted on the data points to provide an estimate of the optimal power and corresponding spear valve position.

The full derivation of the ordinary least-squares estimation can be found in Appendix D, but an example of the application of the ordinary least-squares approach on the data points for a combination of wind speeds is shown in Figure 6-1. With the estimated relation, the actual maximum power production and corresponding spear valve position are determined.

6-3 Maximum power production

The post-processing of all results of the first simulation leads to the static maximum power production shown in Figure 6-2a. Only the wind extrema combinations within the 95%-probability interval are evaluated. For clarity, the predicted maximum power production from Chapter 4 is repeatedly shown in Figure 6-2b.

The numerical results show a high resemblance to the predicted maximum power production. An important observation is made from the level of the rated-power plateau in Figure 6-2a. The incorporation of all drivetrain characteristics reduces the power production of the DOT wind farm to 73.2%. An analysis of the components gives insight into the contributors to this loss.

The most significant loss is found in the fixed-displacement pump. It has an estimated volumetric efficiency of 93.7% and mechanical efficiency of 90.4% at rated power. The transport through the hydraulic lines has an insignificant power loss and typically yields an efficiency of over 99%. As theory prescribes, the nozzle has viscous friction losses resulting in an efficiency of 95%. The overall efficiency of a multi-jet Pelton turbine typically lies around 90%, with a maximum of 92.5% [77][78]. Assuming the Pelton turbine operates at optimal speed, the chosen model parameters lead to a rated Pelton efficiency of 91% [79]. Lastly, the electrical generator is presumed to have an efficiency of 94.4%, equal to that of conventional wind turbines [34]. Altogether, these efficiencies result in an overall drivetrain efficiency of 69.1%.

Figure 6-3a demonstrates to what extent the DOT wind farm can obtain the static maximum power production compared with the NREL wind farm. The comparison that is derived

theoretically in Chapter 4 is again shown in Figure 6-3b. For both images, the focus is set on the below-rated region as the power production is constant in above-rated conditions.

Figure 6-3 confirms that the incorporation of all drivetrain characteristics reduces the maximum power production to roughly 73% for equal wind speeds. In both images, the performance deteriorates for a variance in wind speeds. Furthermore, both images exhibit a bottleneck near rated conditions.

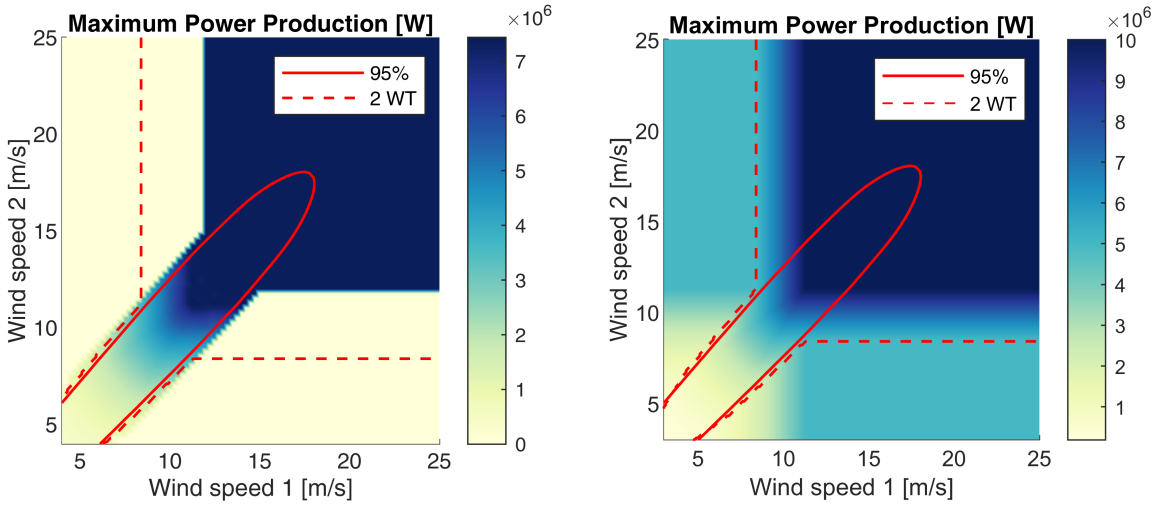

Figure 6-2: The (a) simulated maximum power production and (b) theoretical optimal wind capture of the DOT wind farm. The 95%-probability interval and boundary for operation of both turbines are indicated by the red lines.

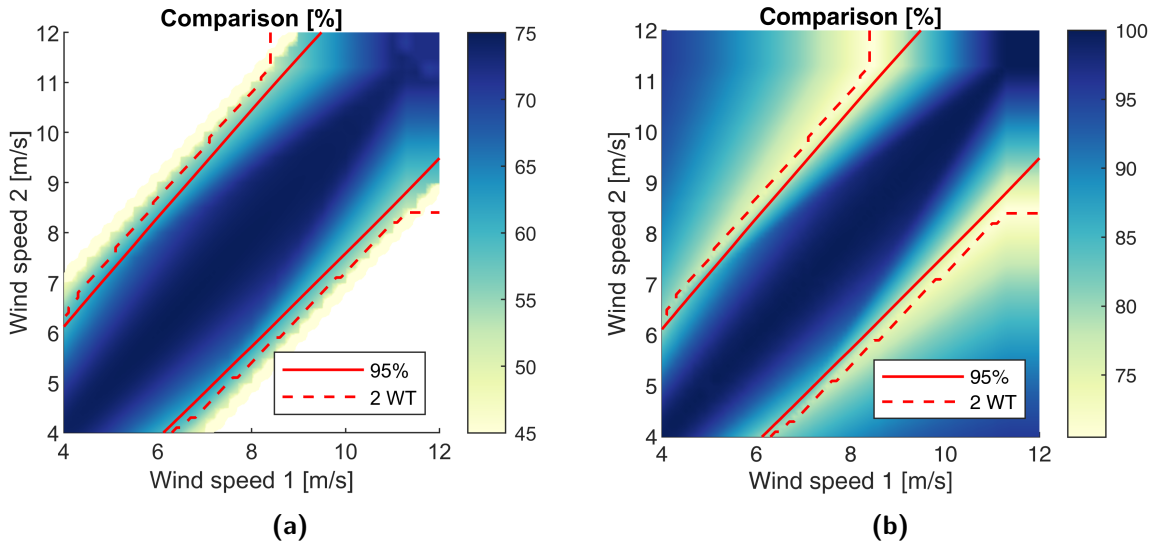

Figure 6-3: The (a) simulated maximum power production of the DOT wind farm is compared with the NREL wind farm. For clarity, the (b) same comparison derived theoretically in Chapter 4, is shown again.

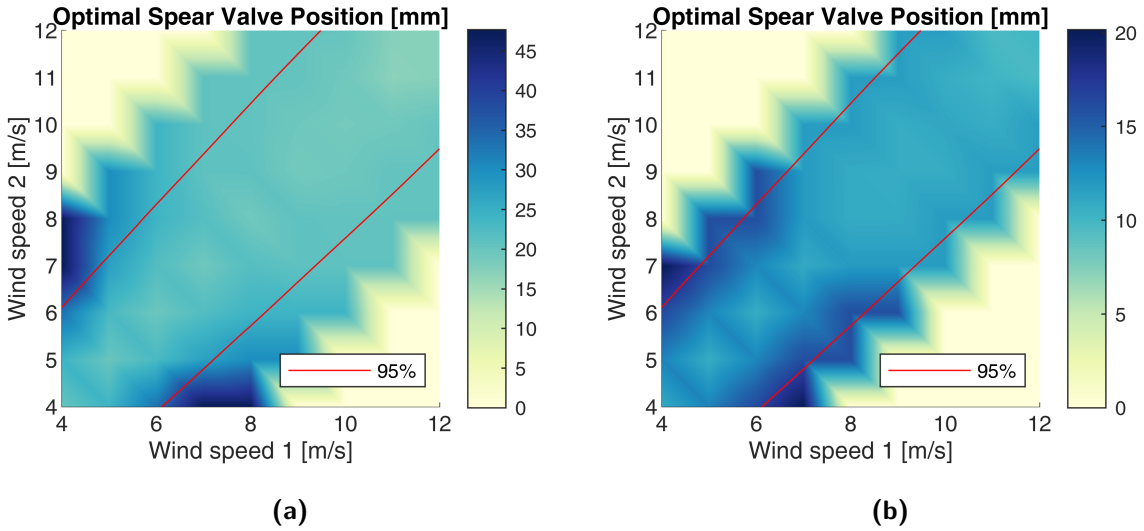

Figure 6-4: Initial simulation results indicate that (a) the initial nozzle design (d = 0.08 m) requires significant spear actuation. An alternative is presented by (b) a nozzle with a larger diameter (d = 0.1 m) that requires less actuation.

6-3-1 Optimal spear valve positions

The optimal spear valve positions corresponding to the maximum power production of initial simulations are shown in Figure 6-4a. The actual spear valve positions near the diagonal lie close to their expected value from Chapter 5. When deviating from the diagonal, it is seen that the spear valve ought to be opened considerably further for optimal performance, particularly near cut-in conditions. This effect is accredited to the acceleration of the wind turbine with higher wind speed. As a result of the higher rotor speed, the wind turbine produces a higher flow and the spear valve has to be opened to avoid a pressure build-up. If the spear valve is not opened, the pressure build-up may result in the standstill of the wind turbine with the lower wind speed.

The desired spear valve position fluctuates more than the range expected in Chapter 5. Therefore, the actuation speed of the spear valve would likely not suffice in dynamic conditions. Solutions to this end, are increasing the number of nozzles, the nozzle diameter or actuator speed of the spear valve. An improved design is left out of the scope of this thesis, as it is highly susceptible to the number of wind turbines in the wind farm, and it was chosen to simply increase the nozzle diameter.

For comparison, the same numerical simulations are performed for the larger nozzle diameter. Figure 6-4b confirms that the larger nozzle requires less actuation to facilitate the desired change in nozzle area, particularly near cut-in conditions. Hence, the final set of simulations was performed with the discussed larger nozzle.

6-3-2 Optimal line pressure

Figure 6-5 shows the optimal spear valve position and pressure associated with the maximum power production. Both clearly display the bottleneck towards rated conditions. As Fig-

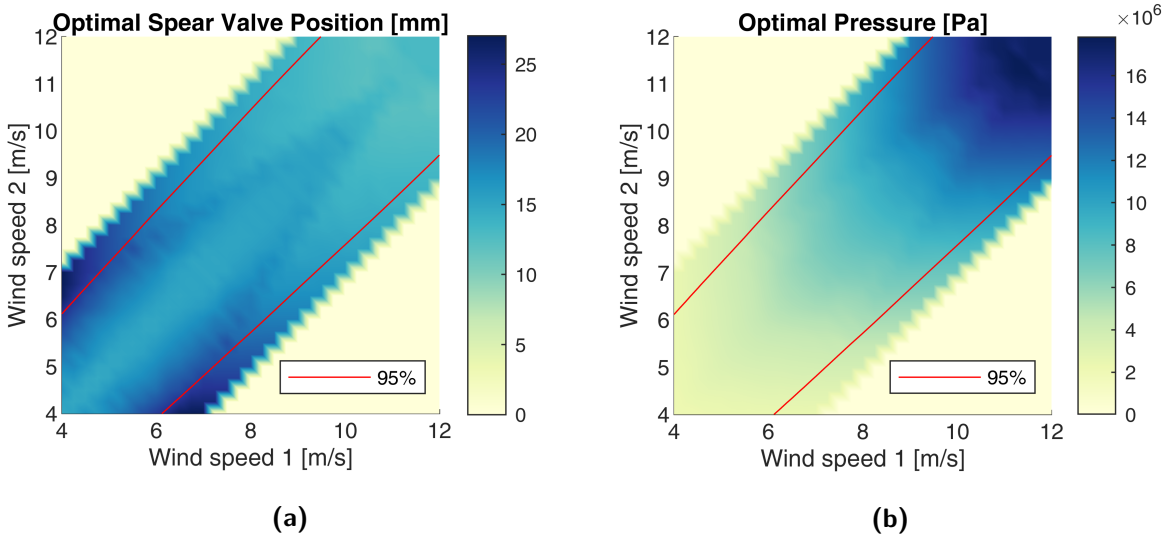

(a) (b)

Figure 6-5: The (a) optimal spear valve position and (b) pressure for maximum power production.

ure 6-5b accounts for all drivetrain characteristics and dynamics, it is used for the proposed feedforward of the optimal pressure.

6-4 Comparison with the NREL 5-MW Reference Turbine

The performance in terms of power production of the DOT wind farm is compared to the NREL wind farm, as described earlier in Chapter 5. During the initial simulations, it was observed that a slight mismatch between the first resonance peak of the hydraulic network and target frequency of the notch filter $\mathcal{N}_1$ results in a significantly worse performance, as the reference pressure input induced water hammer effects in the pipeline. As a consequence, the in- and output pressure oscillate heavily and propagate to the power production. For the eventual simulations, the notch was adjusted to its actual location at 1 rad/s.

The wind field applied to both wind farm is equal. First, Figure 6-6a shows the wind speeds perceived by the individual wind turbines. Thereafter, Figure 6-6b gives the rotor speed of the turbines in the DOT wind farm. Subsequently, the spear valve position and line pressure of the collective pipeline in the DOT wind farm are displayed in Figure 6-6c.

Figure 6-6 shows that the wind turbine with the highest wind speed is allowed to accelerate above its optimal rotor speed. This is derived from the fact that the second wind turbine almost reaches 10 RPM around 600 s, while it perceives only a wind speed of 7 m/s. Furthermore, it reveals that when the wind speeds converge, the rotor speeds tend to return to optimal rotor speed as well. Lastly, both rotor speeds exhibit less fluctuation than the wind speed, which is examined further on in this section.

Sensibly, the line pressure in Figure 6-6c correlates strongly with the lowest wind speed. Figure 6-6c also shows that actuation of the spear valve does not necessarily cause deviations in the collective line pressure. Especially between 500s and 600s, relatively constant pressure is observed, while the spear position is heavily actuated. This is merely a result of the increased

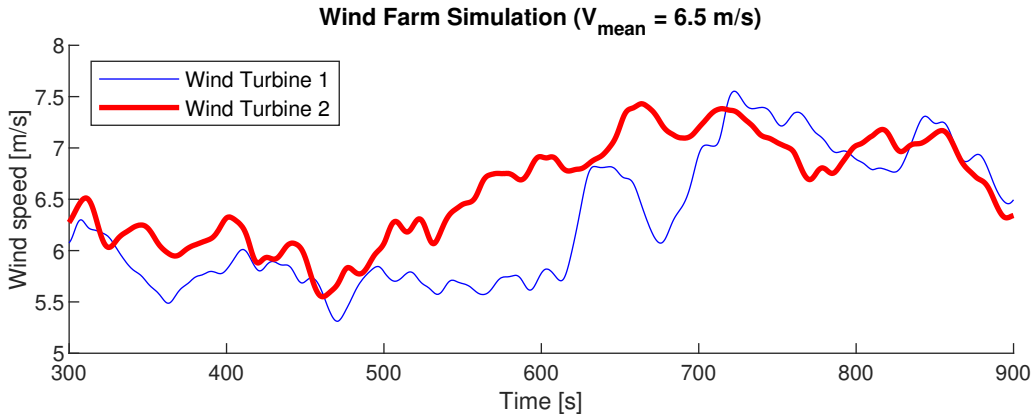

(a)

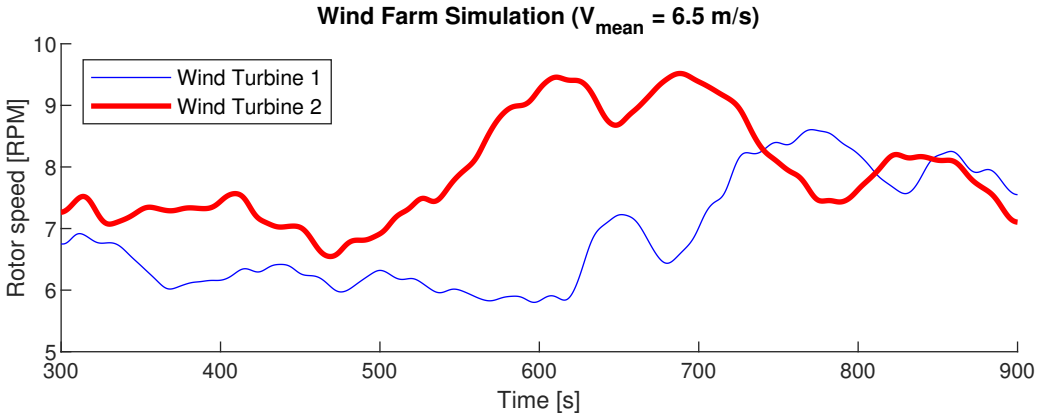

(b)

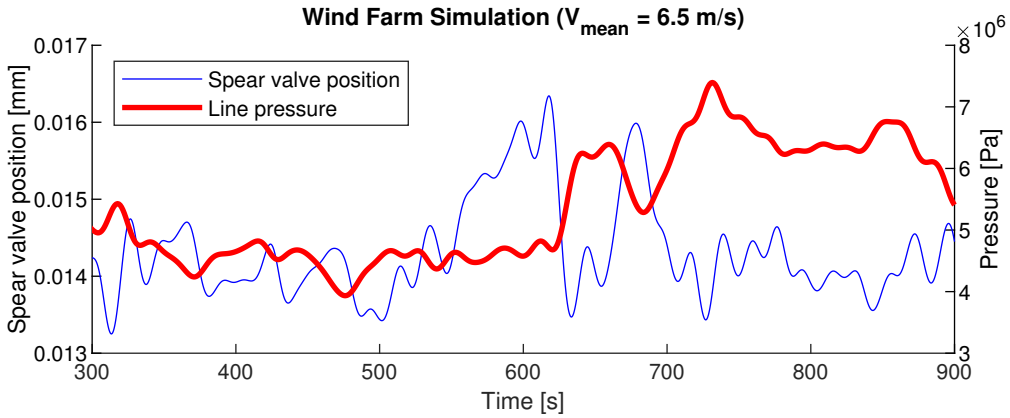

(c)

Figure 6-6: Wind farm simulation for a wind time series with mean wind speed of 6 m/s. The (a) wind speeds and (b) rotor speeds are shown for each wind turbine in the simulation. Lastly, the (c) spear valve position and line pressure are shown.

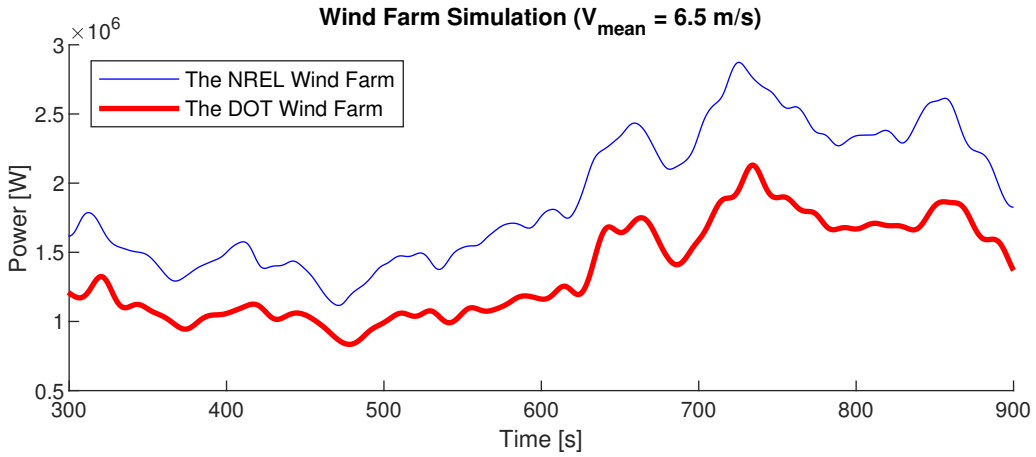

Figure 6-7: Wind farm simulation for a wind time series with mean wind speed of 6.5 m/s for several low-pass filters, characterised by the time constant τ, on the feedforward pressure control. The performance of two DOT wind turbines is compared to conventional NREL turbines.

flow, due to the increased rotor speed seen in Figure 6-6b. Without active actuation of the spear position, the line pressure would increase and may result in the standstill of the first wind turbine. The amount of actuation seen clearly advocates for the necessity to actively control the spear valve position in dynamic operation.

The power production of both wind farms is shown in Figure 6-7. The power of the DOT wind farm revolves around 72.4% of the power production of the NREL wind farm. Despite the expectation of added damping, no reduction in the power fluctuation of the DOT wind farm is obtained.

Lastly, a delay can be observed mainly at the peaks of the power production in Figure 6-7. An analysis of the available aerodynamic power, hydraulic power in the wind turbine and hydraulic power at the Pelton turbine, shows that the delay of roughly 8 seconds results from the hydraulic network.

Chapter 7

Lab-Scale Test Set-Up Design

For the numerical model of the seawater-hydraulic wind farm with a collective pipeline, many assertions have been made. As a result, discrepancies exist between a numerical model and the physical world. A lab-scale test set-up is built to verify the derived control strategy.

This chapter starts with a general overview of the test set-up in Section 7-1. Next, Section 7-2 addresses the individual components in the set-up in more detail, including their limitations and a forecast of possible scaling obstacles. The derivation for individual component control is discussed in Section 7-3.

7-1 General overview

The main purpose of the lab-scale experimental set-up is to perform a hardware-in-the-loop simulation of a seawater-hydraulic wind farm, illustrated in Figure 7-1. The hardware-in-the-loop simulation can be used to validate the control strategy derived in Chapter 4. The set-up is designed to allow testing of both hydraulic configurations as introduced in Chapter 1. Another main consideration in the entire set-up design is the ability to expand towards a Reverse Osmosis (RO) configuration. However, the RO capabilities are outside the scope of this thesis.

As introduced in Chapter 4, two wind turbines represent the lowest and highest wind speed in the wind farm. If a control strategy is able to control both wind turbines, it is assumed that this strategy is effective for a wind farm with wind turbines at intermediate wind speeds as well.

The governing idea of the proposed experimental set-up is illustrated in Figure 7-1. The wind turbines are represented by the combination of the virtual wind turbine model and physical components: an electric motor and hydraulic pump. The physical variables, such as the angular speed and hydraulic pressure, determine the theoretical hydraulic torque. Furthermore, the physical variables are used, in combination with the theoretical wind field and wind turbine model, to simulate the virtual aerodynamic torque. Consequently, a first-order rotor model and controller update the controlled variables in the experimental set-up.

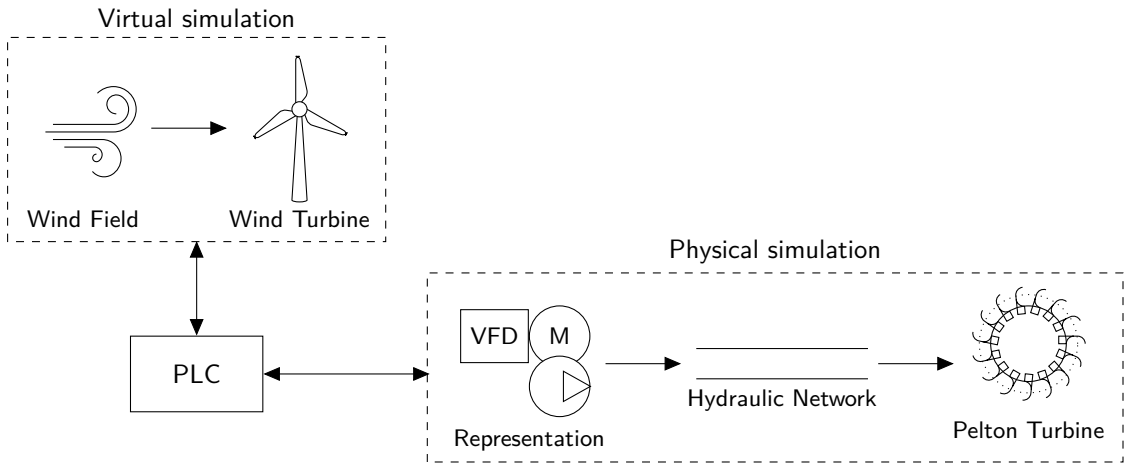

Figure 7-1: An illustration of the hardware-in-the-loop simulation: a combination of a virtual simulation of a theoretical model and a physical simulation with lab-scale components. Both are connected to a PLC that facilitates interaction between the two systems.

After the representation of the two wind turbines, it is shown that the fluid is transported through a hydraulic network to the Pelton turbine. The network is designed to facilitate both configurations, discussed in Chapter 1 (Figure 1-6), and so it feeds to a collective or individual spear valve by setting manual valves. The main components are laid out in Section 7-2, but a complete overview of the hydraulic diagram and employed components is found in Appendix E.

All components are controlled through a Programmable Logic Controller (PLC). The PLC reads all sensor inputs and consecutively sends appropriate control values to the Variable Frequency Drive (VFD) that in turn controls each of the motors. The design and manufacturing of the electrical cabinet can be found in Appendix F.

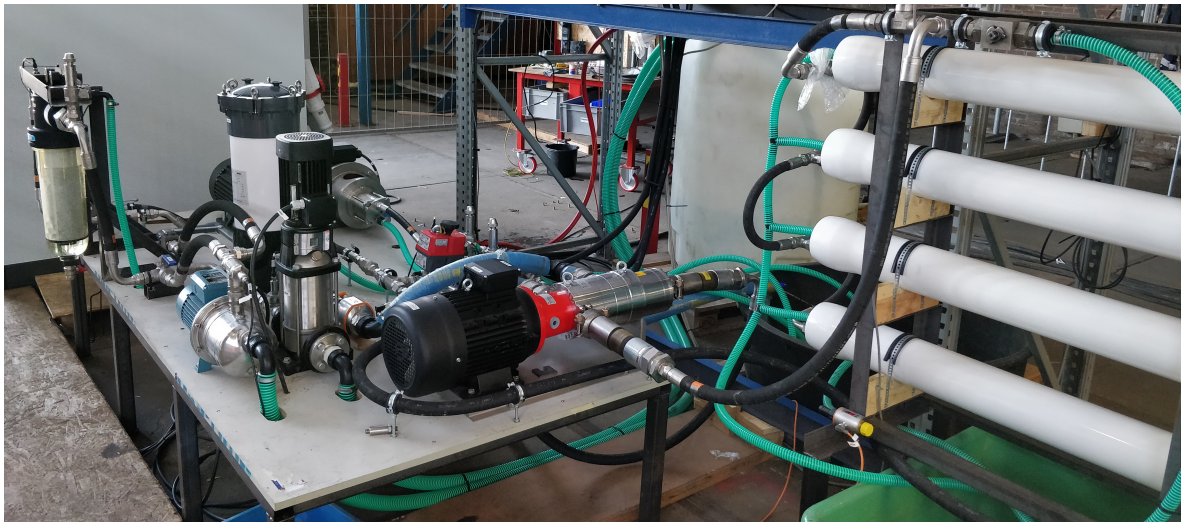

Figure 7-2: The hardware-in-the-loop simulation consists of a virtual and physical simulation. The physical simulation is provided by the lab-scale set-up shown in this picture, with most of the physical components commissioned.

7-2 Description of physical components

The components shown in the physical simulation outline in Figure 7-1 correspond to physical components, shown in Figure 7-2. This section elaborates on these components and their design specifications. A more detailed description of all used components is enclosed in Appendix E and Appendix F.

7-2-1 Wind turbine representations

As introduced, the Delft Offshore Turbine (DOT) wind turbine is represented by an electric motor coupled to a hydraulic pump. To facilitate high pressures, the DOT requires a positive displacement pump, and as such, this type of pump is also used for the lab-scale test.

The driving consideration when selecting the size of this pump is the expansion to RO. In the initial design, each pump was to supply seawater to a single RO membrane. The specification of the pump is required to supply a flow of 60 L/min at 60 bar. The ideal driving power is in theory $P = Q\Delta p = 6\,\text{kW}$. As losses will inevitably occur, the electric motor power rating is chosen slightly higher at 7.5 kW, imposing a minimal pump efficiency of 80% at nominal pressure to achieve the desired flow.

The axes are aligned by a lantern housing and are coupled using a ROTEX flexible jaw coupling, obviating any misalignment and safeguarding the maximum torque [80]. The lantern is depicted right of the black, electric motors in Figure 7-3.

7-2-2 Hydraulic network

To ensure the structural integrity of the hydraulic network, the following design philosophies were followed. For atmospheric pressure lines, conventional green suction hoses are used to

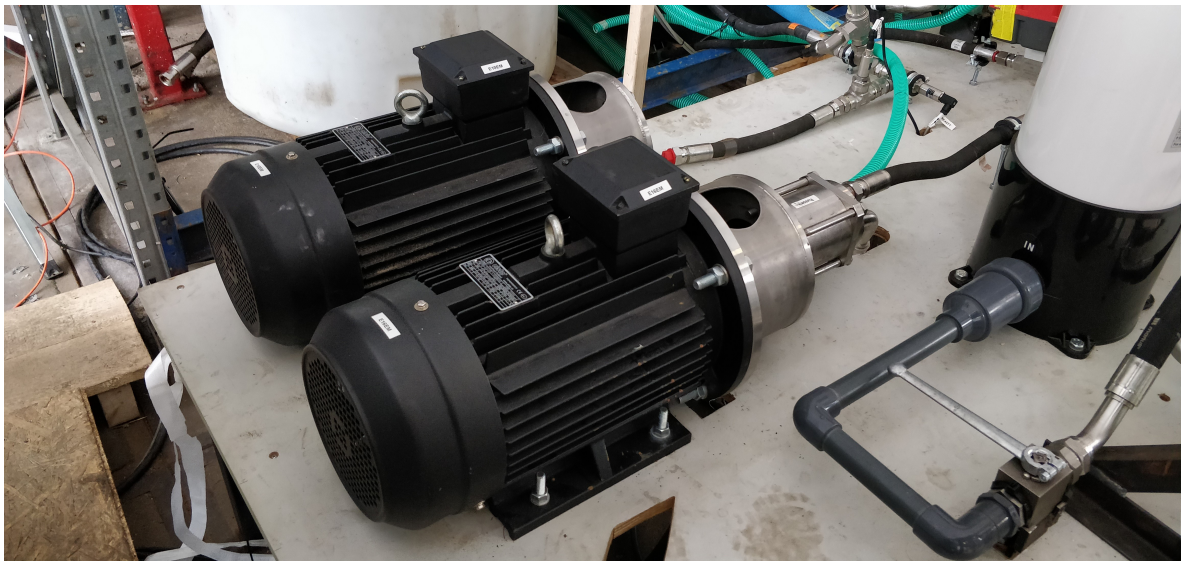

Figure 7-3: The wind turbines are represented by an electric motor and hydraulic pump, connected by a ROTEX flexible jaw coupling in an aluminium lantern housing.

Manufacturer	TheWaterHydraulics
Type	MB160-M35
Speed (max.)	4000 RPM
Displacement	34.6 cc/rev
Pressure (max.)	160 bar

(a)

Manufacturer	Elsto
Type	H3G-160M-4
Power	7.5 kW
Voltage	3 x 400V
Speed	1500 RPM

(b)

Table 7-1: Specifications of (a) the axial piston motor, used as the seawater-hydraulic pump, and (b) the electric motor, serving as the wind turbine representation.

withstand possible pressure bursts and to avoid implosion. The hose ends are connected to a tulle with a clamp, that typically converts to a screw connection.

Low-pressure piping is made from PVC and is manufactured in-house. The remaining low-pressure lines and all high-pressure lines are carried by pressure hoses from a certified manufacturer and include swivels for easy installation.

High pressures in the hydraulic network are prevented by the application of pressure relief valves. In general, the pressure relief valves are placed in the proximity to the possible origin of pressure build-up, e.g. a clogged filter or pump. Additionally, pressures are constantly monitored in the software and will trigger an emergency stop in case of an overload. In an emergency shut-down, the pressure is instantly released from the system by an electrically actuated emergency valve.

7-2-3 Pelton Turbine

Pelton turbines are usually implemented in combination with a basin and dam at a higher altitude, resulting in a low-pressure, high-volume flow. The size of the Pelton turbine in the current research is radically different as it is subject to a high-pressure low-volume flow to minimize kinetic losses in the pipelines. The Pelton turbine is therefore custom designed and made by Guglielmi, in Vogogna, Italy.

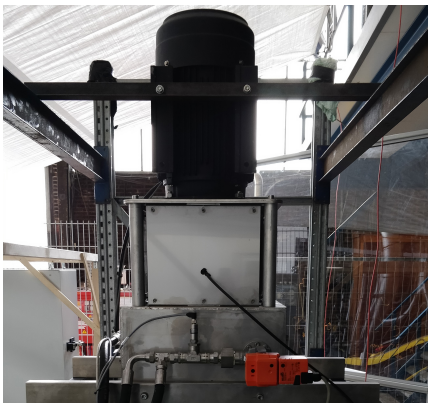

Figure 7-4: The Pelton turbine and the orange spear valve actuators are mounted above the tank.

Figure 7-5: A close-up picture of the Pelton runner wheel. The spear valves are placed in opposite directions and as close to the buckets as possible.

An electric motor with VFD is used as a generator to recover energy from the water jets. A torque sensor with speed encoder is installed between the motor and runner wheel to measure the dynamic fluctuations in torque accurately. Again, a flexible jaw coupling is used to account for small misalignment and ward the maximum torque.

Manufacturer	Elsto/Guglielmi
Type	H3G-160M2-2
Power	15 kW
Voltage	3 x 400V
Speed	3000 RPM
# of buckets	30
Deflection angle	168°
PCD	0.325 m

Table 7-2

Manufacturer	Belimo/Guglielmi
Type	LVC24A-MP-TPC
Pressure	60 bar
Nominal flow	3.6 m^3/h
Spear tip angle	50°
Nozzle diameter	6 mm
Actuator Stroke	15 mm
Actuator Speed	0.43 mm/s

Table 7-3

Table 7-4: Specifications of (a) the Pelton turbine with the electric generator and (b) the spear valve with actuator.

7-2-4 Auxiliary systems

The hydraulic pump, as part of the wind turbine representations, give definition to the auxiliary systems. The pumps are designed to each give a nominal flow of 3.6 m^3/h. Furthermore, the feed pressure should be 3 bar to ensure proper inlet of the pump chambers. Lastly, the pumps dictate a maximum particle size of 10 μm.

(a)

(b)

Figure 7-6: The auxiliary system provide the hydraulic pumps with the proper feed flow. The test set-up has (a) two boost pumps - only the left is used in this thesis - and (b) a centrifugal filter.

A simple centrifugal boost pump as described in Table 7-5, is used to meet the aforementioned conditions. The benefit of this pump is that, by design, it does not have a strict limitation on the particle size and allows a suction height up to 16 m at the inlet. The fluid is then filtered by the centrifugal filter specified in Table 7-6 to meet the desired maximum particle size.

Manufacturer	Calpeda
Type	NGX 6/22
Power	1.5 kW
Voltage	3 x 400V
Flow	0.5 - 8.4 m^3/h
Pressure	2.5 - 4.5 bar
Temperature	0 - 35 °C

Table 7-5

Manufacturer	Cintropur
Type	NW500
Flow (max.)	28 m^3/h
Pressure (max.)	16 bar
Membrane	10 μm
Temperature	0 - 50 °C

Table 7-6

Table 7-7: Specifications of (a) the boost pump and (b) the centrifugal filter providing the inlet conditions of the hydraulic pumps.

7-2-5 Electric & control cabinet

All components in the electrical cabinet, the outer shell of the cabinet and all motors are connected to the earth. This protects against electrocution as a result of static charges in the coils of the motor and electric leakages.

The high-voltage circuit is protected against overload and short-circuiting by means of thermal and magnetic circuit breakers. The DC bus of the high voltage circuit is protected by high

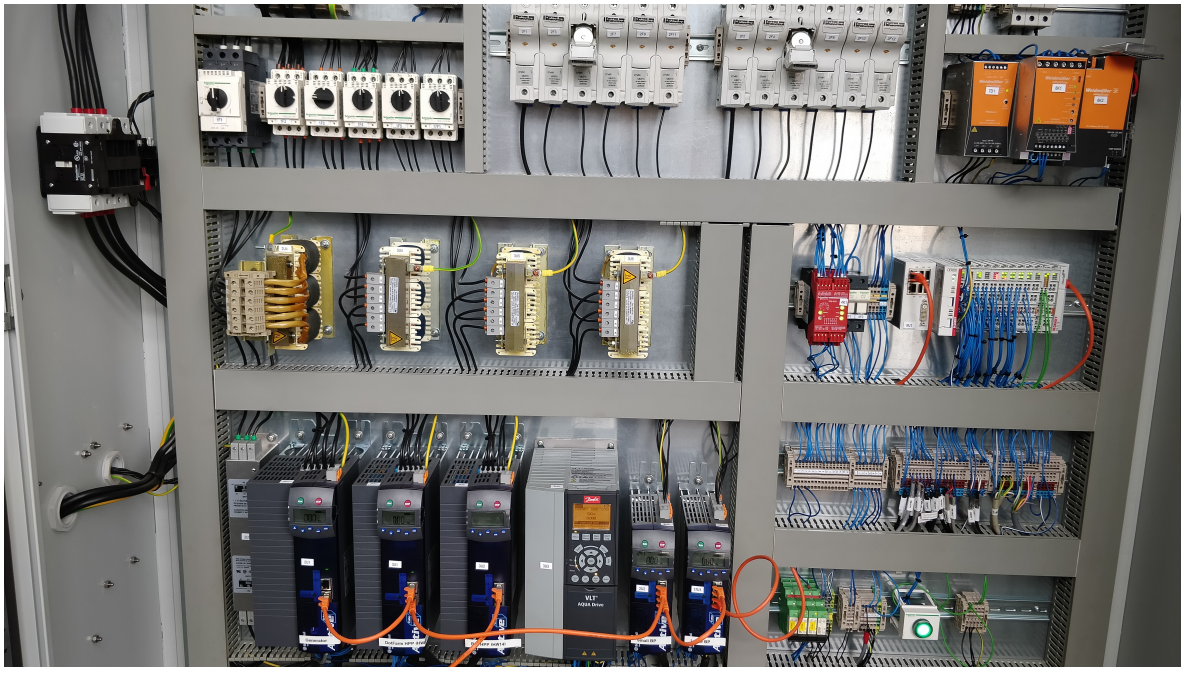

Figure 7-7: A picture of the electric control cabinet during the commissioning of the test set-up.

voltage fuses. The low-voltage circuit is protected against overload and short-circuiting by a thermal circuit breaker and field fuses after an Uninterruptible Power Supply (UPS).

All wiring is dimensioned to continuously withstand the maximum current allowed by the aforementioned safeguards and ensures the integrity of the wiring, even in the event of short-circuiting. Furthermore, the high-voltage wiring is entirely separated from low-voltage wiring & sensor cables in both the electrical cabinet and the test set-up. The separation of the wiring ensures that noise and disturbances from magnetic flux are minimized.

The low-voltage circuit encompassing the PLC is equipped with an UPS in the event of power loss. If either voltage circuit loses power supply, an emergency stop is triggered. The system remains controllable due to the presence of the UPS.

7-3 Subsystem control design

While the value of the desired set-point is determined by the supervisory controller, the subsystem controllers actually obtain the desired set-point. Subsystem controllers are often implemented by relatively simple control structures that respond quickly to reach the desired value [81][33]. The application of subsystem controllers allows to effortlessly test the control strategy that is incorporated in the supervisory controller.

The considered experimental set-up has multiple subsystem controllers, of which two are derived in this thesis. The first aims at regulating the feed pressure to the hydraulic pumps and is described next. After that, the Pelton turbine controller that ensures optimal electrical power production, is outlined.

7-3-1 Feed pressure control

The feed pressure control is an important auxiliary system as it ensures proper inlet conditions to the hydraulic pumps. Consider the hydraulic network between the boost pump and the pumps as a single element. The change in feed pressure is then given by

$$\Delta \dot{p}_{\text{feed}} = \frac{1}{C_{\text{feed}}}(Q_{\text{in}} - Q_{\text{out}}) \tag{7-1}$$

where C_{feed} encompasses the hydraulic capacity of the entire aforementioned hydraulic network. In this particular case, Q_{in} represents the flow of the boost pump and Q_{out} the flow of both hydraulic pumps. Eq. (7-1) clearly demonstrates that whenever there is a discrepancy between in- and outgoing flow, the pressure changes.

Hence, the in- and outgoing flows have to be matched to maintain a constant feed pressure. This results in an analytical relation between the flows. Consequently, if a relationship between the flow and the angular speed of the respective pump is defined, an analytical relation of the pump speeds can be determined. This analytical relation makes the system highly suitable for feedforward control.

A complete scheme of the proposed feed pressure control is illustrated in Figure 7-8. The boost pump is commanded by a simple, yet effective, feedforward control action based on the

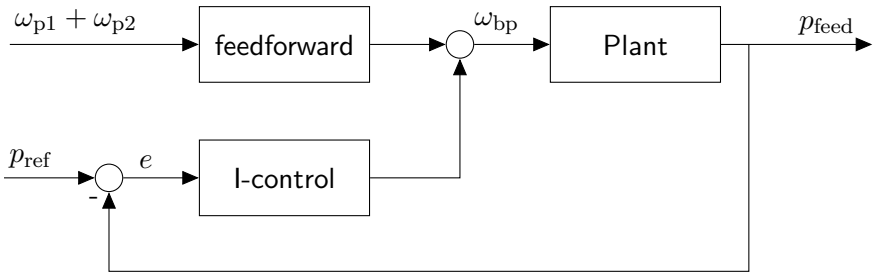

Figure 7-8: An illustration of the feed pressure controller. The speed of the hydraulic pumps lead to a feedforward control action and is augmented with an integral control action by closing the loop on the reference pressure.

hydraulic pump speeds. Temporal differences in flow may arise, so a feedback control loop with integral action is added to the control scheme. The analytical relation and integral gain are derived next.

The derivation of the analytical relation between pump speeds

A perk of the working principle of the applied positive-displacement pumps is that it displaces a fixed volume per revolution, referred to as the volumetric displacement. Hence, irrespective of the operating conditions, the outgoing flow of Eq. (7-1) is conveniently given by

$$Q_{out} = D_h\omega_{p1} + D_h\omega_{p2} = D_h(\omega_{p1} + \omega_{p2}) \tag{7-2}$$

where ω_{p1} and ω_{p2} are the angular speeds of the high-pressure pumps, and D_p is the displacement given in Table 7-1a.

The boost pump employs a centrifugal impeller, of which the relation between flow and angular speed under a pressure is not yet known. An initial experiment is performed to map the relationship between the flow and speed of the boost pump at atmospheric pressure. The speed set-point of the boost pump is set with incremental fixed values. The generated flow is led through the filter back to an open end at atmospheric pressure in the tank. Each stage of a boost pump speed will eventually result in a steady-state flow, measured after the filter.

The aforementioned leads to the relation between boost pump speed and measured flow displayed in Figure 7-9. Based on the results, the flow at atmospheric pressure is approximated by

$$Q_{bp} = \frac{1}{k_{bs}}\omega_{bp}, \tag{7-3}$$

where k_{bs} is the slope of 1/308 (m^3/h)/RPM and ω_{bp} is the angular speed of the boost pump.

However, the conditions during operation of the test set-up deviate from atmospheric pressure, as the boost pump is to supply a feed pressure of 3 bar. The initial hypothesis is that the linear relation holds, but requires a fixed increment in angular speed to account for the deviation in desired pressure.

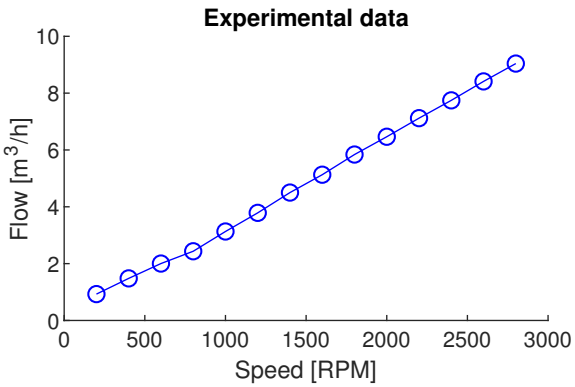

Figure 7-9: The resulting linear relationship between flow and speed of the centrifugal boost pump.

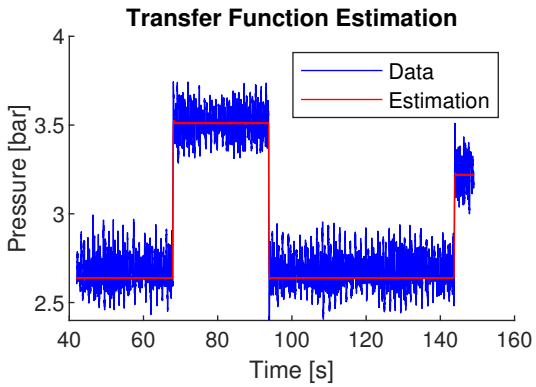

Figure 7-10: A linear simulation of the estimated transfer function compared to the actual output.

As given in Table 7-6, the centrifugal filter introduces a pressure loss of roughly 0.5 bar between the boost pump outlet and hydraulic pump inlet. Hence to obtain a feed pressure of 3 bar at the inlet of the hydraulic pumps, the boost pump has to operate at a pressure of roughly 3.5 bar. The technical specification sheet of the boost pump suggests it can attain this pressure for a maximum flow of 4.25 m^3/h at 2800 RPM. From the linear relation, it is found that only 1300 RPM is required to obtain the same flow under atmospheric pressure. Consequently, it is expected that a constant baseline speed of 1500 RPM is required to supply the feed pressure of 3 bar in the absence of flow.

The ingoing flow of Eq. (7-1) is then given by

$$Q_{\text{in}} = \frac{1}{k_{\text{bs}}}(\omega_{\text{bp}} - k_{\text{bb}}), \tag{7-4}$$

where k_{bb} is the constant baseline speed of 1500 RPM.

The derived relations Eq. (7-2) and Eq. (7-4) are substituted into Eq. (7-1). The change in pressure is set to zero and then rewritten to the analytical relation

$$\omega_{\text{bp}} = k_{\text{bs}} D_{\text{h}} (\omega_{\text{p1}} + \omega_{\text{p2}}) + k_{\text{bb}}. \tag{7-5}$$

Filtering of the hydraulic pump speed

The angular speeds of the hydraulic pumps ω_{p1} and ω_{p2} are estimated by their drives, which yield noisy signals. To avoid a highly fluctuating target speed of the boost pump, a filter is designed to reject the noise. An example of the measured signal at both minimum and maximum speed is shown in Figure 7-11a. A Fast Fourier Transform (FFT) is used to analyze the power spectral density estimation of the signals shown in Figure 7-11b [82]. The sampling frequency of 100 Hz is dictated by the cycle time of the PLC and, by Shannon's sampling theorem, results in an analyzed spectrum up to 50 Hz.

A distinct peak can be observed around 20 Hz (≈ 125 rad/s) and 40 Hz (≈ 250 rad/s) during operation at the minimum speed. At maximum speed, the power spectral density estimation

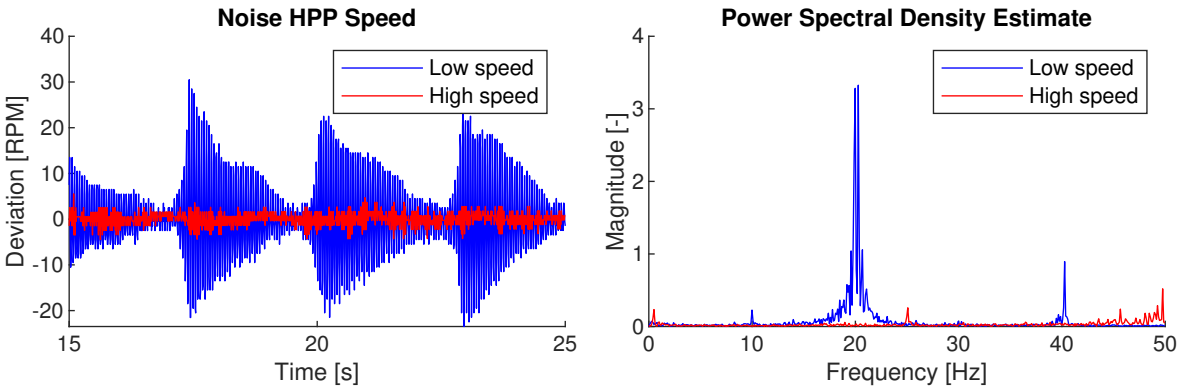

Figure 7-11: The measured high-pressure pump speed has significant noise. A close-up on (a) the noise and (b) its power spectral density estimate on both low and high speed.

shows a more equal distribution with only minor peaks. This merely suggests that no noise frequency can be targeted specifically.

Therefore a combination of a notch filter $\mathcal{N}_{\mathrm{p}}(s)$ and a first-order low-pass filter $\mathcal{L}_{\mathrm{p}}(s)$ is synthesized to obtain a smooth signal. In the Laplace-domain, these filters are shaped as [76]

$$\mathcal{N}_{\mathrm{p}}(s)\mathcal{L}_{\mathrm{p}}(s) = \frac{s^2 + \beta_{\mathrm{n}} s + \omega_{\mathrm{c1}}^2}{s^2 + \beta_{\mathrm{b}} s + \omega_{\mathrm{c1}}^2} \frac{\omega_{\mathrm{c2}}}{s + \omega_{\mathrm{c2}}} \tag{7-6}$$

where ω_{c1} is the central rejected frequency of the notch filter, β_{n} and β_{d} represent the damping coefficient of the numerator and denominator respectively, and ω_{c2} is the cut-out frequency of the low-pass filter. The filter parameters are empirically tuned to $\omega_{\mathrm{c1}} = 125$ rad/s, $\beta_{\mathrm{n}} = 0$ rad/s, $\beta_{\mathrm{d}} = 500$ rad/s and $\omega_{\mathrm{c2}} = 15$ rad/s.

Loop-shaping the integral gain of the feed pressure control

It is desired to shape the integrator gain on a dynamic model of the open-loop system to ensure the stability of the closed-loop system. First, a first-order transfer function of the system is estimated from the time-domain data of another basic experiment. While the outgoing flow by the hydraulic pumps is held constant at 2 m^3/h, a step on the boost pump speed results in the step response of the feed pressure, shown in Figure 7-10.

The first-order transfer function with the shape [75]

$$G(s) = \frac{k_{\mathrm{bpi}}}{s + \omega_{\mathrm{bpi}}} \tag{7-7}$$

is determined by an instrumental-variable estimation [83]. This is implemented by the *tfest*-function of MATLAB's System Identification Toolbox [84]. The identification results in the values $k_{\mathrm{bpi}} = 0.05$ and $\omega_{\mathrm{bpi}} = 17.3$. Figure 7-10 shows a linear simulation of the estimated transfer function over the actual data.

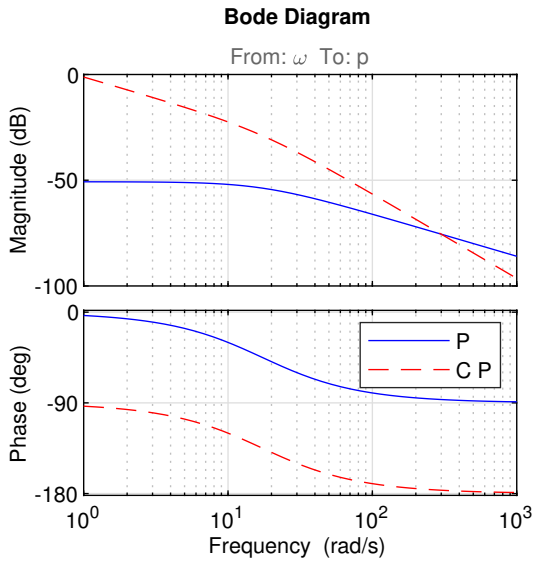

Figure 7-12: The Bode diagram of the open-loop boost system P, from speed to pressure, and the the open-loop boost system with controller C.

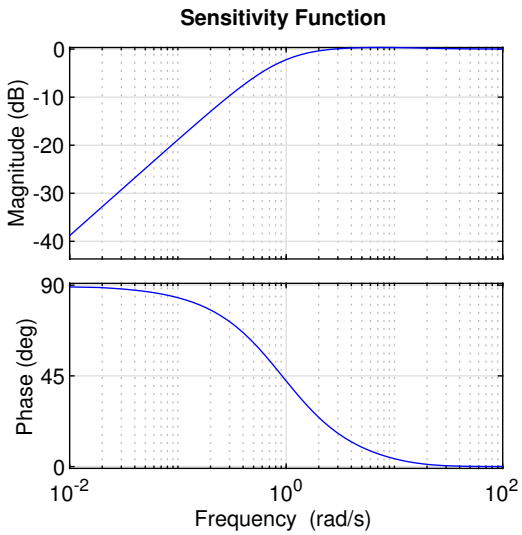

Figure 7-13: The sensitivity function of the closed-loop system. If the integral gain is increased further, the sensitivity peak surpasses the zero-dB line.

Consequently, the loop is closed by applying conventional feedback and introducing an integral action K_i/s only. The Bode diagram of the open-loop system with and without a controller is plotted in Figure 7-12. The integrator gain is shaped to yield ample gain margin and limit the peak sensitivity, to account for errors in the model and disturbances in the plant. An integrator gain $K_\mathrm{i} = 300$ is selected and results in a gain margin of 16.5dB and the sensitivity function shown in Figure 7-13.

7-3-2 Pelton speed control

In earlier research, introduced in Chapter 2, it was set out that feedforward control can very well be used to control the Pelton turbine [5][28]. The optimal performance of the Pelton turbine, as given in Section 3-5, holds if

$$\omega_\mathrm{p} = \frac{1}{2R_\mathrm{p}} C_\mathrm{v} \sqrt{\frac{2\Delta p_\mathrm{n}}{\rho_\mathrm{h}}} \tag{7-8}$$

and can be rewritten as

$$\omega_\mathrm{p} = K_\mathrm{pt} \sqrt{\Delta p_\mathrm{n}}. \tag{7-9}$$

Again, the analytical relation advocates for the application of feedforward control.

Assuming seawater properties from Table 3-1, Pelton properties from Table 7-2 and a discharge coefficient of 0.95, yields an initial estimate for the feedforward gain

$$K_{\mathrm{pt}} = \frac{C_{\mathrm{v}}}{2R_{\mathrm{p}}}\sqrt{\frac{2}{\rho_{\mathrm{h}}}} = 0.128\,\mathrm{rad/Pa}^{0.5}. \tag{7-10}$$

The implementation of feedforward control is prone to parameter errors. As no feedback is applied, a slight variance in parameters can lead to significant steady-state errors and suboptimal Pelton operation [36].

Filtering of the line pressure

The line pressure is measured by the high-pressure sensor FT800-2000 from FirstRate. Unfortunately, like most pressure sensors, this provides a noisy signal. Similar to the feedforward controller implemented for the feed pressure, the direct implementation of this value would lead to a highly fluctuating reference speed. A low-pass filter is added to remove the noise from the measured line pressure [76]

$$\mathcal{L}_{\mathrm{l}}(s) = \frac{\omega_{\mathrm{c3}}}{s + \omega_{\mathrm{c3}}}, \tag{7-11}$$

where the corner frequency ω_{c3} is empirically found to give satisfactory results at 3 rad/s.

7-4 Tuning of the subsystem controllers

The initial subsystem controllers, derived in the previous section, are tuned to improve their performance. In this section, first, the feed pressure control is optimized empirically. Thereafter, the Pelton controller is improved by data-driven performance optimization using the Extremum Seeking Control (ESC) method.

7-4-1 Tuning of the feed pressure controller

Several observations were made during the initial deployment of the feed pressure control. While the hypothesis of a linear relation between speed and flow was confirmed, the different operating pressure significantly altered the slope and base of the analytical relation. Due to the beneficial performance of the integrator gain, the actual relation could easily be derived from the steady-state values of the integral action. This resulted in the corrected parameters $k_{\mathrm{bs}}D_{\mathrm{h}} = 0.34$ and $k_{\mathrm{bb}} = 2200$.

The eventual result of the feed pressure tuning is presented in Figure 7-14a and Figure 7-14b. From the left image, it is observed that the disturbances of the high-pressure hydraulic pumps do not significantly propagate to the boost pump speed. Furthermore, it is seen that especially during transitions in speed, the integral action actively provides a control action. Most importantly, the tuned feed pressure control results in a favorable, constant feed pressure of 3 bar.

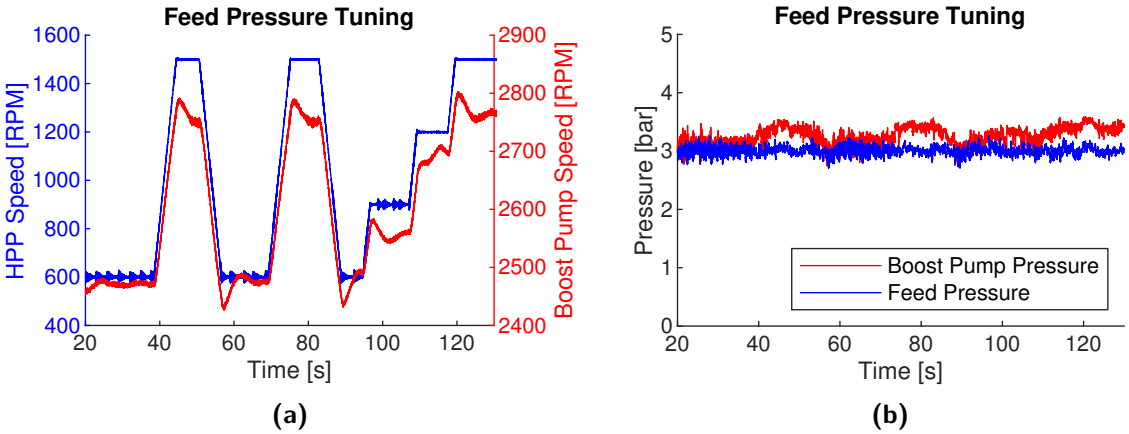

Figure 7-14: The system is exposed to (a) a series of step responses on the high-pressure pump speed. The tuned controller shows exemplary performance in (b) regulating the constant feed pressure of 3 bar. The pressure at the boost pump shows the pressure loss over the centrifugal filter.

7-4-2 Data-driven optimization of the Pelton controller

The Pelton controller is optimized to mitigate the effect of parameter deviations. ESC is implemented to find the improved value of the feedforward gain. The ESC algorithm is a model-free, data-driven optimization method. It seeks to minimize a cost function based on the output of the system by altering the control parameters subject to optimization.

The scheme is illustrated in Figure 7-15. The system parameter is excited by a periodic excitation signal

$$\hat{K}_{\mathrm{pt}} = K_{\mathrm{pt}} + a\sin(\omega_{\mathrm{e}} t), \tag{7-12}$$

where $a\sin(\omega_{\mathrm{e}} t)$ represents the dither signal. The frequency ω_{e} has to be within the bandwidth of the system dynamics, such that the same periodic excitation can be seen in the output of

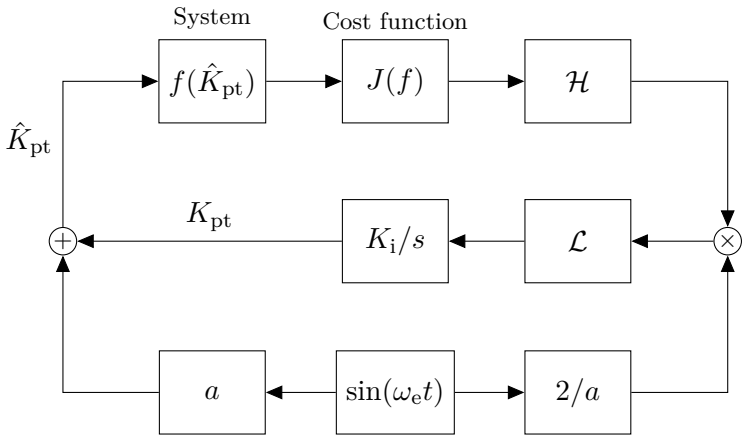

Figure 7-15: The block scheme of Extremum Seeking Control algorithm.

the system. Furthermore, the amplitude a has to yield a significant signal-to-noise ratio to clearly distinct fluctuation of the system from noise.

The perturbed system parameter then yields a perturbed output of the system. The aim is to maximize the generated electrical power and therefore the system output is used directly, obviating a cost function. The objective function is written in a Taylor series expansion

$$P_{\mathrm{e}}(\hat{K}_{\mathrm{pt}}) \approx P_{\mathrm{e}}(K_{\mathrm{pt}}) + a\sin(\omega_{\mathrm{e}}t)\frac{\partial P_{\mathrm{e}}}{\partial \hat{K}_{\mathrm{pt}}} + \mathcal{O}, \tag{7-13}$$

where $\mathcal{O}$ signifies higher-order terms. The signal is filtered through a high-pass filter to remove the first steady-state DC-term. Consecutively, the signal is multiplied by the demodulation signal $2/a\sin(\omega_{\mathrm{e}}t)$ and gives

$$2\sin^2(\omega_{\mathrm{e}})\frac{\partial P_{\mathrm{e}}}{\partial \hat{K}_{\mathrm{pt}}} + \mathcal{O} = \frac{\partial P_{\mathrm{e}}}{\partial \hat{K}_{\mathrm{pt}}} - \cos(2\omega_{\mathrm{e}})\frac{\partial P_{\mathrm{e}}}{\partial \hat{K}_{\mathrm{pt}}} + \mathcal{O}. \tag{7-14}$$

If the plant introduces a significant phase delay with respect to the frequency period, the demodulation is compensated with a phase offset as well.

The choice of the integrator gain K_{i} determines the rate at which the system parameter is updated and is a trade-off between convergence speed and stability. A low integrator gain removes the contribution of the cosine located at a twice the dither frequency. Hence, the signal fed to the integrator is filtered through a low-pass filter, leaving only the information of the gradient. As such, the integrator gain can be increased to yield faster convergence. The integrated gradient updates the system parameter

$$K_{\mathrm{pt}} = K_{\mathrm{pt,init}} + K_{\mathrm{i}}\int \frac{\partial P_{\mathrm{e}}}{\partial \hat{K}_{\mathrm{pt}}} \tag{7-15}$$

where $K_{\mathrm{pt,init}}$ is the initial estimate derived in Section 7-3. Ultimately, the equation above converges to the optimal value of K_{pt} as the gradient information converges to zero.

Application of Extremum Seeking Control

Consider below-rated operation around 30 bar for the application of ESC, such that there exists sufficient clearance for a perturbation on the system. feedforward based on the estimated parameter then results in an initial nominal generator speed of 2100 RPM or 220 rad/s.

The generator drive is limited to a change rate of 20 Hz/s, which translates to an angular acceleration 104.7 (rad/s)/s. From the derivative of Eq. (7-12), it can then be concluded that $a \cdot \omega$ should not invoke a change rate that exceeds this value. To remain within the dynamics of the system, this opposes the limit $a \cdot \omega < 0.052$. As the system naturally follows the desired set-point, it is assumed that this limitation supersedes the limitation opposed by the bandwidth of the system.

The noise on the speed estimation of the generator drive typically lies within 10 RPM. To yield a significant signal-to-noise ratio, the excitation of the system parameter is chosen at

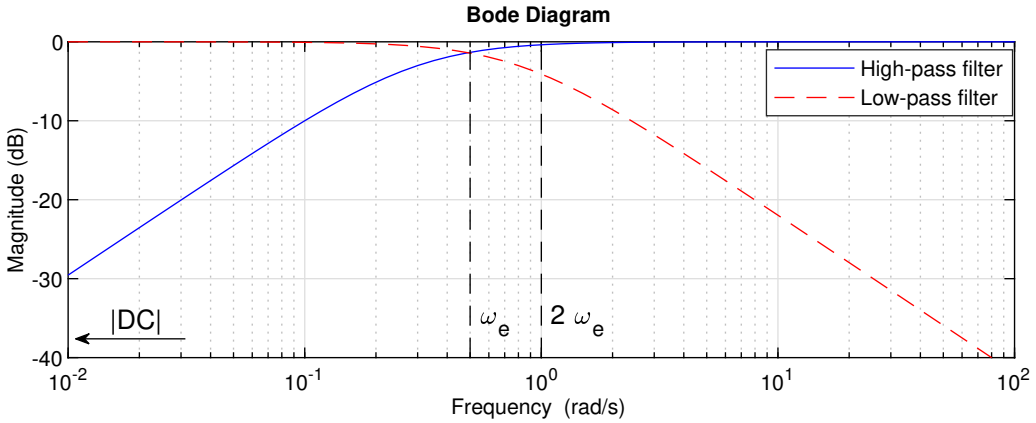

Figure 7-16: The high-pass filter is designed to remove the |DC|-term. Consequently, the low-pass filter remove the double dither frequency $2\omega_e$ and higher-order terms. Both filters aim to pass through the dither frequency unscathed.

$a = 0.0052$ to result in an amplitude of 100 RPM. The frequency of the dither signal is chosen as $\omega_e = 0.5$ rad/s. Although higher frequencies may still respect the opposed limitation, this frequency was chosen to conveniently obviate the phase offset in the demodulation signal.

The high-pass filter cut-in frequency is chosen as $\omega_{hpf} = 0.3$ rad/s, such that the harmonics of the dither signal pass through. The low-pass filter cut-off frequency is chosen as $\omega_{lpf} = 0.8$ rad/s, to suppress the double dither frequency. Figure 7-16 shows the intended effects: removal of the DC-term and double dither frequency, but leaving information on the dither frequency intact. Lastly, the integrator gain is empirically found to give satisfactory results at $K_i = 1 \cdot 10^{-4}$.

The process of ESC is displayed in Figure 7-17a and Figure 7-17b. The optimized value of K_{pt} stagnates at a plateau of 0.082 after roughly 1000 seconds. Figure 7-17b shows that the generator speed accurately tracks the shape of the perturbed feedforward gain, which

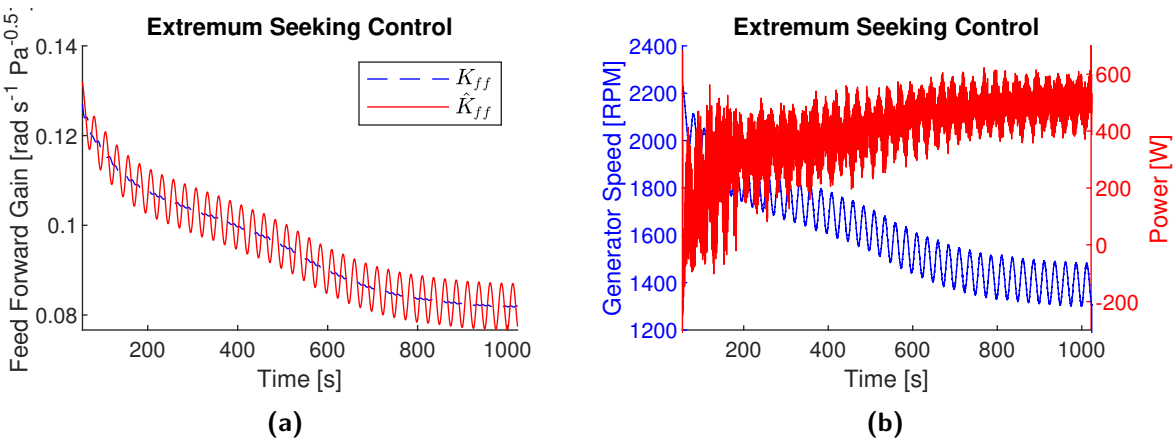

Figure 7-17: The optimization by Extremum Seeking Control updates (a) the feedforward gain and improves (b) the power. The generator speed accurately follows the perturbed feedforward gain.

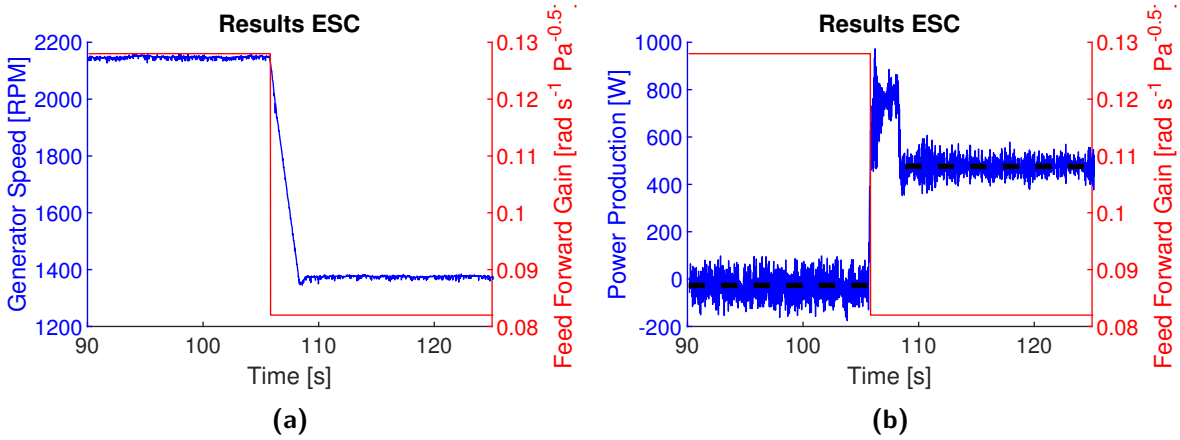

Figure 7-18: The optimized feedforward gain is forced on the system around 105 s. It shows that the (a) the generator speed decreases and (b) power production increases. The dashed lines indicate the mean power plateaus of -27 W and 473 W.

confirms that the dither frequency lies within the bandwidth of the system. Lastly, it can be seen that the power indeed increases from roughly -27W to 473W by applying the updated value found with ESC.

Both images show that ESC optimizes the feedforward gain, which is confirmed by forcing the feedforward gain K_{pt} during operation at a steady-state flow and pressure. The results are shown in Figure 7-18a and Figure 7-18b, and evidently demonstrate that the optimized value produces more power than the initial estimate. Simultaneously, the result also indicates a significant issue with the Pelton turbine.

The torque sensor with speed encoder is located between the roller bearing hub and the generator, and therefore only reflects the mechanical energy after the hub. The Pelton turbine is operated without any external loads to reveal the mechanical losses in Figure 7-19. The mechanical losses grow exponentially with speed and are therefore attributed to aerodynamic resistance.

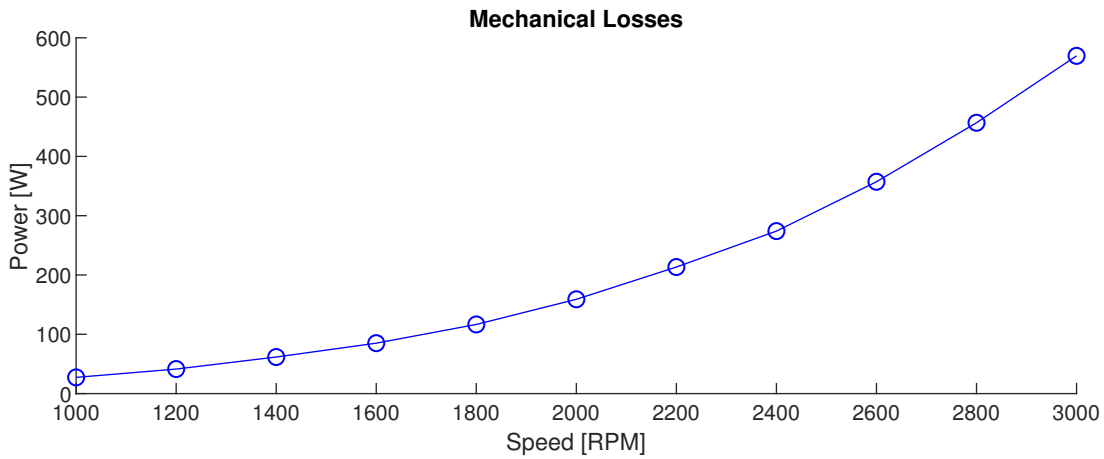

Figure 7-19: The mechanical losses in the Pelton turbine grow exponentially with speed.

Chapter 8

Conclusion and Recommendations

8-1 Conclusion

This thesis focuses on deriving an optimal control strategy for a seawater-hydraulic wind farm with fixed-displacement pumps interconnected through a collective hydraulic network to a centralized power station, referred to as the Delft Offshore Turbine (DOT) wind farm. The difficulty herein arises from the combination of the fixed-displacement pumps and a collective pipeline, imposing an equal hydraulic torque throughout the wind farm. At the same time, the fluctuating wind speed throughout the wind farm results in a varying aerodynamic torque per wind turbine. An imbalance between the aerodynamic and hydraulic torque accelerates the wind turbines and results in the deviation from their individual optimal operating points.

The task of the control strategy derived in this thesis is to pursue the collective optimal performance, while simultaneously safeguarding the maximum rotor speed in all wind turbines. Conventional pitch control, as derived for the NREL 5-MW reference turbine, limits the maximum rotor speed in both below- and above-rated conditions. Pitch control with a fixed hydraulic torque satisfies as the control strategy for above-rated conditions. However, a hydraulic torque control strategy to obtain optimal performance in below-rated conditions does not yet exist and is derived in this thesis.

For the DOT, the optimal performance of the below-rated control strategy focuses solely on the partial objective of maximizing power production. Since individual wind turbines deviate from their optimal operating point, the collective maximum power production of the DOT wind farm is thus far unknown. Therefore, the first sub-goal of this thesis is to identify the hydraulic torque, equivalently pressure, that maximizes the power production for the multiple wind speeds in the wind farm.

The multiple wind speeds throughout the wind farm are approached by its extremes. The minimum wind speed reflects the wind turbine that can obtain the lowest pressure, while the maximum wind speed indicates the wind turbine that can obtain the highest power. The pressure maximizing the power production of these turbines is assumed to yield the collective maximum power production for intermediate wind speeds as well.

Each combination of extreme wind speeds is mapped to a maximum power production and corresponding optimal pressure. To set a narrower focus on this maximum power production map, the probability of each combination of extreme wind speeds is included. A statistical analysis uses wind speed measurements of the existing offshore wind farm Egmond aan Zee, leading to the 95%-probability interval used for the derivation of an optimal control strategy.

It is concluded that within the 95%-probability interval, the maximum power production is obtained for pressures that all wind turbines can sustain. From the perspective of collective optimal performance, control strategies based on conventional methods do not perform well overall. The best below-rated control strategy is the use of feedforward of the optimal pressure based on the extremes of the measured wind speed. In order to facilitate this control strategy, the DOT requires a measurement or estimation technology to determine the wind speeds throughout the wind farm accurately.

Towards the second and third sub-goal of this thesis, a numerical model is derived to reflect the characteristics and dynamics of the DOT wind farm accurately. The subsystem controllers in the complete control scheme of the DOT wind farm are designed, including a stability analysis, and implemented in the numerical model.

Numerical simulations confirm the performance of the control scheme, which implements the control strategy, in dynamic conditions. The rotor speeds are free to fluctuate in below-rated conditions but remain limited to the maximum rotor speed through conventional pitch control. The fluctuation of rotor speeds results in a varying flow. The spear valve controller counteracts the varying flow to maintain the reference pressure. This concludes that active spear valve control is a necessity for the DOT wind farm in below-rated conditions.

The DOT wind farm is compared with a conventional wind farm employing the NREL 5-MW reference turbine. In rated conditions, the DOT wind farm power production is reduced to 73.2% compared with the conventional wind farm. In a dynamic, below-rated numerical simulation, the power production fluctuates around 72.4% of the conventional wind farm. To offset power production losses, and reduce the Levelized Cost of Energy (LCOE), it is therefore concluded that the DOT wind farm must provide at least an equivalent cost reduction in the capital and operational expenditure.

A lab-scale test set-up is built to indicate discrepancies between the derived model and the physical world, as stated in the fourth sub-goal. Due to unforeseen problems, the derived maximum power production and control strategy are not validated by experimental data. However, a partial validation is obtained through the design and optimization of two subsystem controllers: the feed pressure and Pelton turbine controllers.

A feedforward feedback control scheme provides feed pressure control. The feedforward control action exploits a derived analytical relation between the pump speeds, while a feedback action on the feed pressure removes residual steady-state errors. The steady-state values of the feedback action update the derived analytical relation. Ultimately, the tuned feedforward-feedback controller exhibited exemplary performance and underlined the competence of such a control scheme. If the auxiliary systems of the DOT wind farm allow an analytical relation, a similar control scheme should be implemented.

The Pelton turbine also uses a feedforward controller based on the analytical relation for optimal power capture. An Extremum Seeking Control algorithm is applied and improved the power production from -27W to 473W by optimizing the feedforward gain. The value of

the optimized feedforward gain is corrected to 67% of the estimated value. The significant difference led to the discovery of poor mechanical efficiency of the Pelton turbine as a result of aerodynamic friction, whereas these losses are negligible in theory. A relatively high-pressure, low-volume flow is inherent to the DOT and results in high velocities in the Pelton turbine. This should be taken into careful consideration during the design of the Pelton turbine. Furthermore, it is concluded that Extremum Seeking Control is an accessible, model-free algorithm to optimize parameters.

8-2 Recommendations

Based on the results and conclusions of this thesis, several recommendations are discussed.

- **The effect of multiple wind turbines on the maximum power production**

  In this research, the varying wind speed in a wind field is approached by its two extrema. For simplicity, it is assumed initially that intermediate wind speeds do not significantly alter the collective optimum. The approach can be formulated as the following steady-state optimization problem

$$\arg\max_{\tau_{\mathrm{r,h}}} \sum_{i=1}^{n_{\mathrm{t}}} \eta_{\mathrm{r},i}(\tau_{\mathrm{r,h}}, \beta_{\mathrm{r},i}, V_{\mathrm{w},i}) P_{\mathrm{w},i}(V_{\mathrm{w},i})$$

$$\text{s.t.} \qquad \omega_{\mathrm{r},i} \leq \omega_{\max},$$

  where n_{t} is the number of wind turbines in the optimized wind farm, which is in this case two, $\tau_{\mathrm{r,h}}$ the collective hydraulic torque, $\beta_{\mathrm{r},i}$ the rotor pitch angle, $V_{\mathrm{w},i}$ the wind speed, $P_{\mathrm{w},i}$ the available wind power and $\omega_{\max}$ the maximum rotor speed.

  The available wind power of wind turbine i depends solely on its wind speed. Subsequently, the rotor efficiency of wind turbine i is determined by its tip-speed ratio and pitch angle. The tip-speed ratio is the result of the steady-state rotor speed based on the balance between the hydraulic and aerodynamic torque. The pitch angle serves to limit the torque coefficient if necessary, to meet the constraint on the maximum rotor speed.

  The inclusion of multiple wind turbines with intermediate wind speeds affects this optimization problem following two mechanisms:

  1. Intermediate wind speeds that occur in multiple wind turbines, are weighted more in the optimization problem.
  2. Higher wind speeds have more available wind power and can contribute more to the collective power production. Therefore, higher wind speeds are more dominant in this optimization problem.

  Hence, the inclusion of intermediate wind speeds may shift the collective optimum, depending on the distribution of the wind speeds in a wind field.

The operating points shown in Chapter 4 suggest that wind turbines with the average wind speed would lie closely to the optimal power coefficient. Nevertheless, both aforementioned mechanisms emphasize the operating points of these wind turbines and may affect the collective optimum.

- **A control strategy for wake effects**

  Accounting for wake effects is of tremendous importance to the DOT. As seen in this thesis, the deviation in wind speeds leads to suboptimal performance of the DOT wind farm. The presence of wake significantly increases the variance in wind speeds and thereby inherently deteriorates the performance of the wind farm.

  The minimization of wake effects is a popular topic, also for conventional wind farms [85]. Control strategies to this end are devised, which implement yaw misalignment, rotor tilting or deliberately pitching away for example.

- **The effect of individual pipelines**

  The employment of individual pipelines allows individual optimal rotor efficiency. However, the Pelton runner wheel can only facilitate 4 to 6 nozzles, implying that for a wind farm multiple Pelton runner wheels have to be employed [35].

  Furthermore, the flow and pressure will vary in each line, resulting in different mass flows and jet speeds respectively. The various momenta of the jets inevitably result in suboptimal Pelton efficiency and unknown dynamics due to asymmetrical loads on the Pelton runner wheel.

  Both effects add complexity to the design of such a Pelton turbine, yet could provide a better overall drivetrain efficiency.

- **Replace broken components in the lab-scale test set-up**

  The lab-scale test set-up gives insight into the behavior of the physical components. An excellent example in this regard is the Pelton turbine that showed different behavior than expected from theory.

  Moreover, the set-up can show how differences between the model and the physical world affect the maximum power production. In doing so, the experimental data can validate the derived maximum power production and control strategy.

- **Below-rated pitch control for torque increase**

  In the current research, the pitch angle is maintained at fine-pitch for below-rated rotor speeds. As a result, a wind turbine can increase its torque coefficient by 15% by decreasing its tip-speed ratio. However, another increase of 0.8% in the torque coefficient can be obtained by pitch actuation to negative pitch angles. While this appears a small gain at the cost of actuation, it could have a sizable contribution to the annual power production.

- **Development of a variable displacement pump**

  A variable volumetric displacement allows control of the hydraulic torque and thereby individual rotor speeds. Consequently, the rotor speed can be controlled to maintain optimal tip-speed ratio and leads to individual optimal rotor efficiency. Even a modular

activation mechanism as seen in Statoil-Hägglunds, IFAS and Artemis-Mitsubishi could yield better results.

- **Development of novel rotor blades**

  The torque and power coefficient of the rotor blades are considered as described for the NREL 5-MW reference turbine. Reducing the tip-speed ratio below optimal tip-speed ratio allows increasing the torque coefficient by 15% at an equivalent loss of 15% in captured power. A new rotor blade design may improve the possible increase in torque.

Appendix A

Model Parameters

The model parameters used for the numerical simulations are given in the following Table.

Wind turbine			
Rated speed	$\omega_{\mathrm{r,nom}}$	12.1	RPM
Rated torque	$\tau_{\mathrm{r,nom}}$	4.3e6	Nm
Rotor diameter	R_{r}	63	m
Air density	ρ_{w}	1.225	$\mathrm{kg/m^3}$
Combined moment of inertia (DOT)	J_{w}	3.59e7	$\mathrm{kgm^2}$

Hydraulic pump			
Rated speed	$\omega_{\mathrm{p,nom}}$	12.1	RPM
Rated flow	$Q_{\mathrm{p,nom}}$	0.266	$\mathrm{m^3/s}$
Rated pressure	$\Delta p_{\mathrm{p,nom}}$	180e5	Pa
Rated volumetric efficiency	$\eta_{\mathrm{v,nom}}$	93.2	%
Dry friction coefficient	C_{f}	0.02	-
Viscous damping coefficient	ξ_{p}	50e3	Nms
Laminar leakage coefficient	C_{p}	1e-9	$\mathrm{m^3/s/Pa}$
Volumetric displacement	D_{h}	0.224	$\mathrm{m^3/rev}$

Hydraulic network			
Circular pipe diameter	D_{p}	0.5	m
Line length	L_{p}	1000	m
Internal surface roughness	ϵ	5e-5	-
Seawater density	ρ_{f}	1026	$\mathrm{kg/m^3}$
Dynamic viscosity	μ	1.3e-3	kg/m/s
Effective bulk modulus	E	2.33e9	Pa

Spear valve			
Nozzle diameter	D_{n}	0.1	m
Discharge coefficient	C_{d}	0.95	-
Spear tip angle	α	80	$^{\circ}$
Spear actuator time constant	τ_{sv}	1.69	s

Pelton turbine			
Jet deflection angle	β	165	$^{\circ}$
Bucket friction factor	ζ_{p}	0.85	-
Pelton actuator time constant	τ_{pt}	3	s
Generator efficiency	η_{g}	94.4	%

Appendix B

Derivation of a Double-Segment Pipeline State Space Representation

Consider a pipeline with two segments shown in Figure B-1. The pressure decay over the branches is described by

$$p_i - p_{c1} = R_1 Q_1 + L_1 \dot{Q}_1 \tag{B-1}$$

$$p_{c1} - p_{c2} = R_2 Q_2 + L_2 \dot{Q}_2 \tag{B-2}$$

$$p_{c2} - p_o = R_3 Q_3 + L_3 \dot{Q}_3. \tag{B-3}$$

By the law of flow continuation it holds for the hydraulic chambers that

$$Q_{c1} = Q_1 - Q_2 \tag{B-4}$$

and

$$Q_{c2} = Q_2 - Q_3. \tag{B-5}$$

The definition of hydraulic capacitance gives

$$\dot{p}_{c1} = \frac{1}{C_1} Q_{c1} \tag{B-6}$$

and

$$\dot{p}_{c2} = \frac{1}{C_2} Q_{c2}. \tag{B-7}$$

Substituting Eq. (B-4) in Eq. (B-2) and rearranging the terms lead to

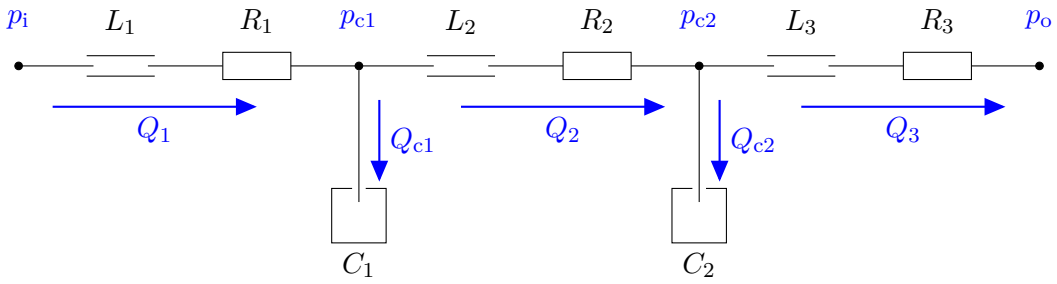

Figure B-1: A representation of a double-segment pipeline.

$$\dot{Q}_{c1} = -\frac{1}{L_2}p_{c1} + \frac{1}{L_2}p_{c2} - \frac{R_2}{L_2}Q_{c1} + \frac{R_2}{L_2}Q_1 + \dot{Q}_1. \tag{B-8}$$

Eq. (B-6) and Eq. (B-8) then result in

$$\ddot{p}_{c1} = -\frac{1}{C_1L_2}p_{c1} + \frac{1}{C_1L_2}p_{c2} - \frac{R_2}{L_2}\dot{p}_{c1} + \frac{R_2}{C_1L_2}Q_1 + \frac{1}{C_1}\dot{Q}_1 \tag{B-9}$$

Similarly, substitution of Eq. (B-4), Eq. (B-5) and Eq. (B-8) in Eq. (B-3) gives

$$\begin{aligned}\dot{Q}_{c2} = \frac{1}{L_2}p_{c1} - \left(\frac{1}{L_3} + \frac{1}{L_2}\right)p_{c2} + \left(\frac{R_2}{L_2} - \frac{R_3}{L_3}\right)Q_{c1} - \frac{R_3}{L_3}Q_{c2} \\ + \frac{1}{L_3}p_o + \left(\frac{R_3}{L_3} - \frac{R_2}{L_2}\right)Q_1\end{aligned} \tag{B-10}$$

With Eq. (B-5), Eq. (B-7) and Eq. (B-8), Eq. (B-10) is rewritten to

$$\begin{aligned}\ddot{p}_{c2} = \frac{1}{C_2L_2}p_{c1} - \left(\frac{1}{C_2L_2} + \frac{1}{C_2L_3}\right)p_{c2} + \left(\frac{C_1R_2}{C_2L_2} - \frac{C_1R_3}{C_2L_3}\right)\dot{p}_{c1} - \frac{R_3}{L_3}\dot{p}_{c2} \\ + \frac{1}{C_2L_3}p_o + \left(\frac{R_3}{C_2L_3} - \frac{R_2}{C_2L_2}\right)Q_1\end{aligned} \tag{B-11}$$

Subsequently, the output variables are given by rearranging Eq. (B-1) as

$$p_1 = p_{c1} + R_1Q_1 + L_1\dot{Q}_1 \tag{B-12}$$

and rewriting Eq. (B-4) and Eq. (B-5) to

$$Q_3 = Q_1 - Q_{c1} - Q_{c2}. \tag{B-13}$$

Assume an equal diameter and segment lengths, than the hydraulic capcitance $C = C_1 = C_2$ and hydraulic inductance $L = L_1 = L_2 = L_3$. Furthermore, the in- and output flows are inserted: $Q_1 = Q_i$ and $Q_3 = Q_o$.

Ultimately, the derived equations are combined in a state space representation:

$$\begin{bmatrix} \dot{p}_{c1} \\ \dot{p}_{c2} \\ \ddot{p}_{c1} \\ \ddot{p}_{c2} \\ \dot{Q}_{c1} \\ \dot{Q}_{c2} \end{bmatrix} = \begin{bmatrix} 0 & 0 & 0 & 0 & \frac{1}{C} & 0 \\ 0 & 0 & 0 & 0 & 0 & \frac{1}{C} \\ \frac{-1}{CL} & \frac{1}{CL} & -\frac{R_2}{L} & 0 & 0 & 0 \\ \frac{1}{CL} & \frac{-2}{CL} & \frac{R_2 - R_3}{L} & -\frac{R_3}{L} & 0 & 0 \\ \frac{-1}{L} & \frac{1}{L} & 0 & 0 & -\frac{R_2}{L} & 0 \\ \frac{1}{L} & \frac{-2}{L} & 0 & 0 & \frac{R_2 - R_3}{L} & -\frac{R_3}{L} \end{bmatrix} \begin{bmatrix} p_{c1} \\ p_{c2} \\ \dot{p}_{c1} \\ \dot{p}_{c2} \\ Q_{c1} \\ Q_{c2} \end{bmatrix} + \begin{bmatrix} 0 & 0 & 0 \\ 0 & 0 & 0 \\ 0 & \frac{R_2}{CL} & \frac{1}{C} \\ \frac{1}{CL} & \frac{R_3 - R_2}{CL} & 0 \\ 0 & \frac{R_2}{L} & 1 \\ \frac{1}{L} & \frac{R_3 - R_2}{L} & 0 \end{bmatrix} \begin{bmatrix} p_o \\ Q_i \\ \dot{Q}_i \end{bmatrix} \tag{B-14}$$

$$\begin{bmatrix} p_i \\ Q_o \\ Q_{c1} \\ Q_{c2} \end{bmatrix} = \begin{bmatrix} 1 & 0 & 0 & 0 & 0 & 0 \\ 0 & 0 & 0 & 0 & -1 & -1 \\ 0 & 0 & 0 & 0 & 1 & 0 \\ 0 & 0 & 0 & 0 & 0 & 1 \end{bmatrix} \begin{bmatrix} p_{c1} \\ p_{c2} \\ \dot{p}_{c1} \\ \dot{p}_{c2} \\ Q_{c1} \\ Q_{c2} \end{bmatrix} + \begin{bmatrix} 0 & R_1 & L \\ 0 & 1 & 0 \\ 0 & 0 & 0 \\ 0 & 0 & 0 \end{bmatrix} \begin{bmatrix} p_o \\ Q_i \\ \dot{Q}_i \end{bmatrix}. \tag{B-15}$$

Appendix C

Initial and Stopping Conditions of the Numerical Simulations

The numerical simulations are subject to several initial and stopping conditions. The initial conditions prevent step responses of the system. The stopping conditions aim to prevent physically improbable or infeasible conditions.

The initial pitch angle for below-rated wind speeds is set to the fine-pitch angle. In above-rated conditions, it is approached by a one-dimensional linear interpolation for purposes of simplicity. Assuming that the wind turbine operates near the optimal tip speed ratio in below-rated conditions, the rotor speed is linearly dependent on the wind speed. Hence, the initial rotor speed is estimated using an interpolation between the limits of the below-rated wind speeds and their corresponding optimal rotor speeds. The maximum rotor speed is taken for wind speeds in the above-rated region. The estimated initial rotor speeds dictate most of the remaining initial parameters, following the equations laid out in Chapter 3.

The initial pressure of each pipeline is overestimated to prevent numerical errors and negative flows during the start-up of the numerical model. As such, each pipeline is initialised at a pressure 4 bars higher than its successor.

The simulations are stopped if the rotor speed of either wind turbines comes to a standstill. Furthermore a static constraint is opposed to the rotor shaft torque of both wind turbines, which is limited to the rated torque of the NREL 5-MW reference turbine at 4.18 MNm. This constraint is implemented by monitoring for shaft torques exceeding the limit for more than a minute. Similar conditions are set on the pressure in the system. The static pressure cannot exceed 200 bar for more than 10 seconds and the dynamic pressure cannot exceed 400 bar.

Appendix D

Derivation of the Ordinary Least-Squares Estimation

The relation between the output power P_{out} of the Delft Offshore Turbine (DOT) wind farm and the spear valve position x is estimated by the fourth-order polynomial

$$P_{\text{out}}(s) = \beta_4 x^4 + \beta_3 x^3 + \beta_2 x^2 + \beta_1 x + \beta_0, \tag{D-1}$$

where β_i represent the unknown coefficients and x the spear position. The series of numerical results are rearranged to a column-vector and yield the matrix form

$$P_{\text{out}} = X\beta \tag{D-2}$$

where X contains the column-vectors of values of x to each of the orders in Eq. (D-1) and β is the vector of the unknown coefficients. As the name suggests, the coefficient vector β is estimated by $\hat{\beta}$ through solving the quadratic minimization problem

$$\hat{\beta} = \arg\min_{\beta} \left(\|P_{\text{out}} - X\beta\|^2 \right). \tag{D-3}$$

Given that the columns of X are linearly independent, the minimization problem has a unique solution by solving the equation

$$X^{\text{T}} X\hat{\beta} = X^{\text{T}} P_{\text{out}}, \tag{D-4}$$

where $X^{\text{T}}X$ is known as the Gramian matrix of X. Combined with the linear independence of X, the Gramian matrix has the beneficial property of positive definiteness. Finally, the ordinary least-squares approach then results in the estimated coefficient vector

$$\hat{\beta} = (X^{\text{T}}X)^{-1} X^{\text{T}} P_{\text{out}}. \tag{D-5}$$

Appendix E

Hydraulic Diagram and Components

The hydraulic diagram is included from page 97 onwards and the complete list of components is given on page 99. The two boost pumps in the left of the hydraulic diagram, specified in Table E-1, provide a feed flow to the rest of the system. Only the Calpeda pump is used in this thesis. The feed pressure is monitored by four low-pressure sensors, the FirstRate FST800-2000, listed in Table E-2. The maximum particle size of the feed flow is secured by the filters given in Table E-3. The Cintropur filter leads to the high-pressure pump and the EWP-USA to the Reverse Osmosis (RO) set-up. A pressure relief valve protects the low-pressure network from pressures over 8 bar.

The high-pressure pumps in the center of the hydraulic diagram, detailed in Table E-4, feed a pressurized flow to the RO set-up and the Pelton turbine. The flow is monitored by four high-pressure sensors, the FirstRate FST800-211, and two temperature sensors, the FirstRate FST600-212, given in Table E-2. Two pressure relief valves protect the high-pressure network from pressure over 69 bar. Furthermore, an electrically actuated valve can instantly depressurize the system in case of an emergency stop.

In the right of the hydraulic diagram, the high-pressure network ends with the spear valves at the Pelton turbine, specified in Table E-5. After the Pelton turbine captures the hydrokinetic power, the water falls in the water tank located under the Pelton turbine.

Manufacturer	Calpeda
Type	NGX 6/22
Flow	0.5 - 8.4 m^3/h
Speed	2800 RPM
Pressure	2.5 - 4.5 bar
Power	1.5 kW
Voltage	3 x 400 V
Temperature	0 - 35 °C

Manufacturer	Grundfos
Type	CRN3-11 A-FGJ-G-E-HQQE
Flow (max.)	3 m^3/h
Speed	2900 RPM
Pressure (max.)	25 bar
Power	1.1 kW
Voltage	3 x 400 V
Temperature	-20 - 120 °C

Table E-1: Specifications of the boost pumps providing the feed flow and pressure to the system.

Manufacturer	FirstRate		
Type	FST800-2000	FST800-211	FST600-202
Application	Low-pressure	High-pressure	Temperature
Pressure	0 - 10 bar	0 - 75 bar	300 bar
Sensor signal	4 - 20 mA	4 - 20 mA	4 - 20 mA
Temperature	-20 - 125 °C	-20 - 85 °C	0 - 50 °C

Table E-2: Specifications of the pressure and temperature sensors that are used for monitoring.

Manufacturer	Cintropur
Type	NW500
Flow (max.)	28 m^3/h
Pressure (max.)	16 bar
Membrane size	10 μm
Temperature	0 - 50 °C

Manufacturer	EWP-USA
Type	HPCF-B-5DC2
Flow (max.)	9 m^3/h
Pressure (max.)	6 bar
Membrane size	3 μm
Temperature	0 - 45 °C

Table E-3: Specifications of filters ensuring the maximum particle size of the feed flow.

Manufacturer	TheWaterHydraulics
Type	MB160-M35
Speed (max.)	4000 RPM
Pressure (max.)	160 bar
Displacement	34.6 cc/rev
Temperature	2 - 50 °C

Manufacturer	Elsto
Type	H3G-160M-4
Power	7.5 kW
Voltage	3 x 400 V
Speed	1500 RPM

Table E-4: Specifications of (left) the axial piston motor, used as the seawater-hydraulic high-pressure pump, and (right) the electric motor, serving as the wind turbine representation.

Manufacturer	Elsto/Guglielmi
Type	H3G-160M2-2
Power	15 kW
Voltage	3 x 400 V
Speed	3000 RPM
Pitch Circle Diameter (PCD)	0.325 m
# of buckets	30
Deflection angle	168°

Manufacturer	Belimo/Guglielmi
Type	LVC24A-MP-TPC
Nominal flow	3.6 m^3/h
Nozzle diameter	6 mm
Spear tip angle	50°
Actuator force	500 N
Actuator stroke	15 mm
Actuator speed	0.43 mm/s

Table E-5: Specifications of (left) the Pelton turbine with the electric generator and (right) the spear valve with actuator.

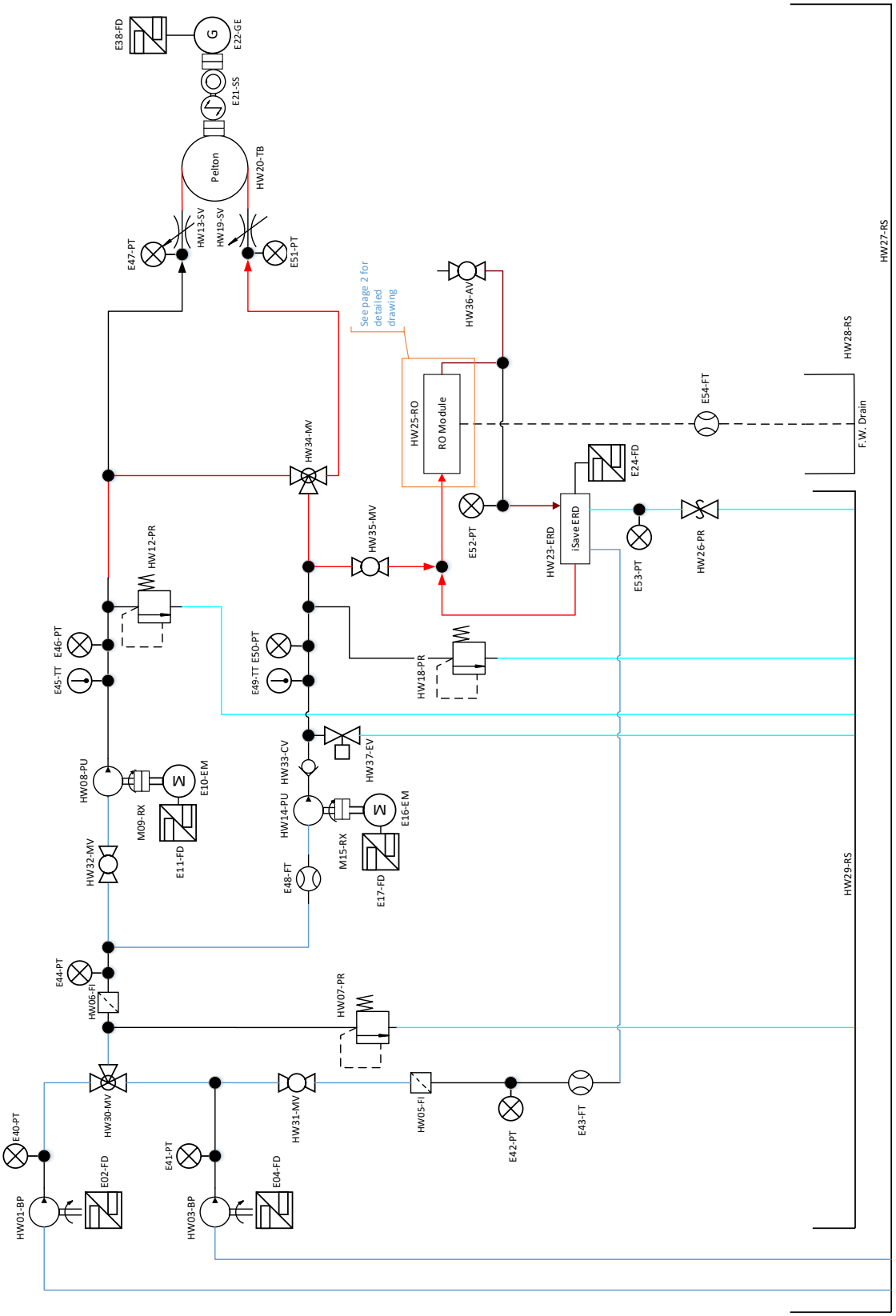
E38-FD
G
E22-GE
E21-SS
Pelton
HW20-TB
E47-PT
HW13-SV
HW19-SV
E51-PT
See page 2 for detailed drawing
HW36-AV
HW25-RO
RO Module
HW34-MV
HW35-MV
E52-PT
HW23-ERD
iSave ERD
E24-FD
E53-PT
HW26-PR
E54-FT
HW28-RS
F.W. Drain
HW27-RS
HW12-PR
E46-PT
E45-TT
E49-TT
E50-PT
HW18-PR
HW33-CV
HW37-EV
HW08-PU
M09-RX
E10-EM
E11-FD
HW14-PU
M15-RX
E16-EM
E17-FD
HW32-MV
E48-FT
E44-PT
HW06-FI
HW07-PR
HW29-RS
HW30-MV
HW31-MV
HW05-FI
E42-PT
E43-FT
E40-PT
E41-PT
HW01-BP
HW03-BP
E02-FD
E04-FD

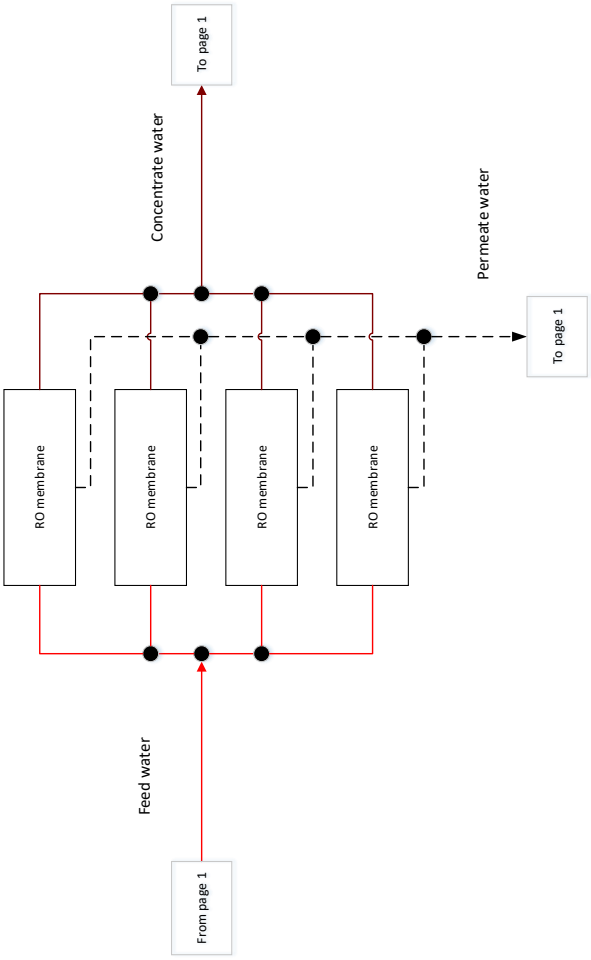
To page 1
Concentrate water
Permeate water
To page 1
RO membrane
RO membrane
RO membrane
RO membrane
Feed water
From page 1

Family	Diagram label	Supplier	Manufacturer	Details
Boost Pump	**HW01-BP**	Lenntech	Grundfos	Grundfos_CRN-3-11-A-FGJ-G-E-HQQE
Frequency Drive	**E02-FD**		Bonfiglioli	Bonfiglioli ActiveCube EtherCAT
Boost Pump	**HW03-BP**		Calpeda	Calpedaa_NGX6-22
Frequency Drive	**E04-FD**		Bonfiglioli	Bonfiglioli ActiveCube EtherCAT
Filter	**HW05-FI**	Lenntech	EWP-USA	HPCF-B-5DC2
Filter	**HW06-FI**		Cintropur	Cintropur_NW500
Pressure Relief Valve	**HW07-PR**		Goetze	Goetze 451 bFK-20-f-f-20-20 PTFE
Pump	**HW08-PU**		The water Hydraulics	Janus M30 35cc
Rotex Coupling	**M09-RX**			KTR Rotex 38 Standard
Electromotor	**E10-EM**		Elsto	H3G-132M-4
Frequency Drive	**E11-FD**	Elsto	Bonfiglioli	Bonfiglioli ActiveCube EtherCAT
Pressure Relief Valve	**HW12-PR**		Goetze	Goetze 451 bFK-20-f-f-20-20 PTFE
Spear Valve	**HW13-SV**		Belimo	LVC24A-MP-TPC
Pump	**HW14-PU**	Hydroton	TheWaterHydraulics	Janus M30
Rotex Coupling	**M15-RX**			KTR Rotex 38 Standard
Electromotor	**E16-EM**		Elsto	H3G-132M-4
Frequency Drive	**E17-FD**	Elsto	Bonfiglioli	Bonfiglioli ActiveCube EtherCAT
Pressure Relief Valve	**HW18-PR**		Goetze	Goetze 451 bFK-20-f-f-20-20 PTFE
Spear Valve	**HW19-SV**			LVC24A-MP-TPC
Pelton Turbine	**HW20-TB**			
Torque Sensor	**E21-TS**		NCTE	NCTE Series 3000
Generator	**E22-GE**		Elsto	H3G-160M2-2
Energy Recovery Device	**HW23-ERD**	Lenntech	Danfoss	iSave_21plus
Frequency Drive	**E24-FD**	Lenntech	Danfoss	VLT Aqua Drive FC 202
RO-membranes	**HW25-RO**	Lenntech		DOW Filmtec SW30-4040 & H4E4G1 pressure vessel
Pressure Relief Valve	**HW26-PR**		Goetze	
Reservoir	**HW27-RS**			
Reservoir	**HW28-RS**			
Reservoir	**HW29-RS**			
Manual valve	**HW30-MV**		Fluiconnecto	
Manual valve	**HW31-MV**		Fluiconnecto	
Manual valve	**HW32-MV**		Fluiconnecto	
Check Valve	**HW33-CV**	Fluiconnecto	PH-Hydraulik	RD-I-G3/4”
Manual valve	**HW34-MV**		Fluiconnecto	
Manual valve	**HW35-MV**		Fluiconnecto	
Air Relieve Valve	**HW36-AV**		Fluiconnecto	
Electric valve	**HW37-EV**			
Frequency Drive	**E38-FD**	Elsto	Bonfiglioli	
Pressure transducer	**E40-PT**		Firstrate	FirstRate FST600-202
Pressure transducer	**E41-PT**		Firstrate	FirstRate FST600-202
Pressure transducer	**E42-PT**		Firstrate	FirstRate FST800-211
Flow transducer	**E43-FT**		IFM	SM9000 SMR21XGXFRKG/US
Pressure transducer	**E44-PT**		Firstrate	FirstRate FST800-211
Temperature transducer	**E45-TT**		Firstrate	FirstRate FST600-202
Pressure transducer	**E46-PT**		Firstrate	FirstRate FST800-2000
Pressure transducer	**E47-PT**		Firstrate	FirstRate FST800-2000
Flow transducer	**E48-FT**		IFM	SM7000 SMR34GGXFRKG/US-100
Temperature transducer	**E49-TT**		Firstrate	FirstRate FST600-202
Pressure transducer	**E50-PT**		Firstrate	FirstRate FST800-2000
Pressure transducer	**E51-PT**		Firstrate	FirstRate FST800-2000
Pressure transducer	**E52-PT**		Firstrate	FirstRate FST800-2000
Pressure transducer	**E53-PT**		Firstrate	FirstRate FST800-211
Flow transducer	**E54-FT**		IFM	SM7000 SMR34GGXFRKG/US-100

Appendix F

Electrical Drawings and Components

The electrical cabinet was designed and manufactured under supervision of Elsto, as shown in Figure F-1. The complete electrical drawings are shown from page 102 and components from page 111. The low- and high-voltage systems are completely separated in the design of the electrical cabinet to prevent electromagnetic disturbances. Both systems have their own mains supply entering the cabinet on the left side. The mains power supplies go directly to two mains switches, which are operated on the outside of the cabinet. The mains cables continue to two separate terminal blocks that distribute the power in the electrical cabinet.

Each subsequent line is protected by a (magnetic) circuit breaker directly after the power distribution. On the high-voltage side, the power lines to the variable frequency drives pass through line chokes to remove harmonic distortions. All drives are connected to a high-voltage DC-bus, which employs double fusing. On the low-voltage side, an AC/DC-converter supplies power to an Uninterruptible Power Supply (UPS) to ensure continuity of the control systems, even during loss of power. Field fuses protect further components after the UPS.

Figure F-1: The manufacturing process of the electrical cabinet at Elsto Drives & Controls.

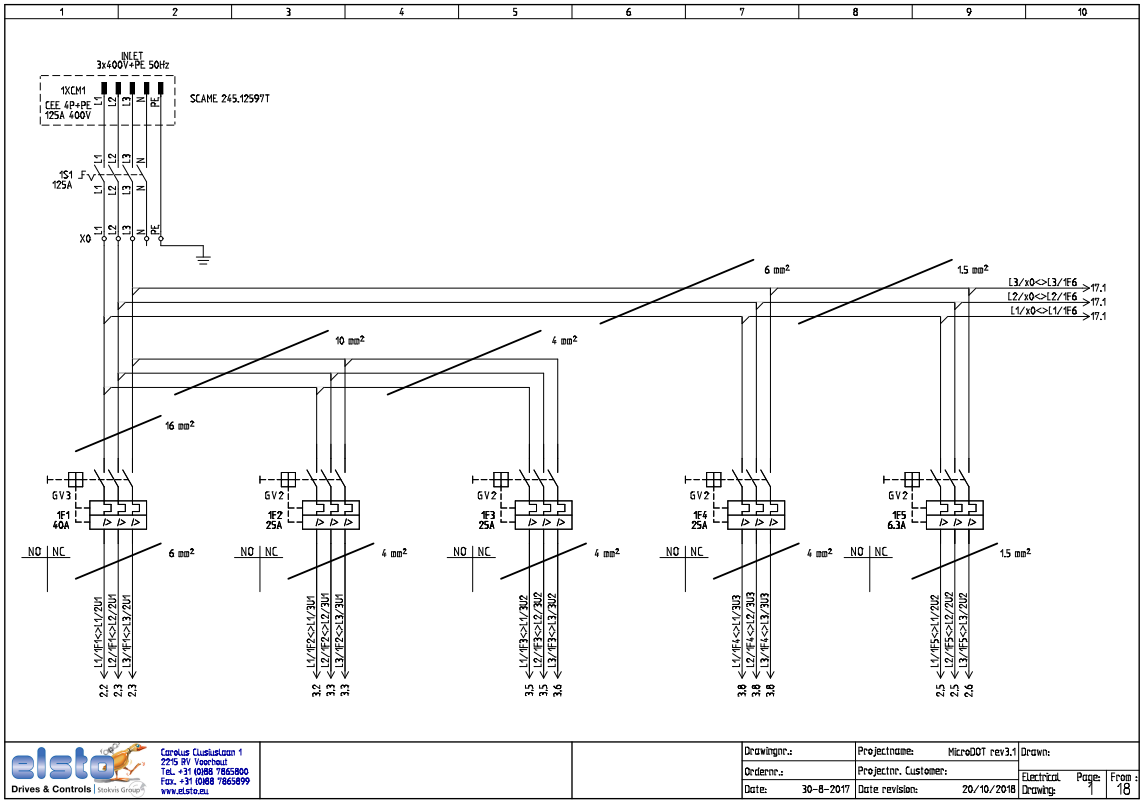
INLET
3x400V+PE 50Hz
1XCM1
CEE 4P+PE
125A 400V
SCAME 245.12597T
1S1
125A
X0
6 mm²
1.5 mm²
10 mm²
4 mm²
16 mm²
L3/x0<>L3/1F6 >17.1
L2/x0<>L2/1F6 >17.1
L1/x0<>L1/1F6 >17.1
GV3
1F1
40A
GV2
1F2
25A
1F3
25A
1F4
25A
1F5
6.3A
NO | NC
6 mm²
4 mm²
4 mm²
4 mm²
1.5 mm²
L1/1F1<>L1/2U1
L2/1F1<>L2/2U1
L3/1F1<>L3/2U1
L1/1F2<>L1/3U1
L2/1F2<>L2/3U1
L3/1F2<>L3/3U1
L1/1F3<>L1/3U2
L2/1F3<>L2/3U2
L3/1F3<>L3/3U2
L1/1F4<>L1/3U3
L2/1F4<>L2/3U3
L3/1F4<>L3/3U3
L1/1F5<>L1/2U2
L2/1F5<>L2/2U2
L3/1F5<>L3/2U2
2.2
2.3
2.3
3.2
3.3
3.3
3.5
3.5
3.6
3.8
3.8
3.8
2.5
2.5
2.6
Carelus Cluiskuiaan 1
2215 BV Voorhout
Tel. +31 (0)88 7865800
Fax. +31 (0)88 7865899
www.elsto.eu
Drawingnr.:
Ordernr.:
Date: 30-8-2017
Projectname: MicroDOT rev3.1
Projectnr. Customer:
Date revision: 20/10/2018
Drawn:
Electrical Drawing: Page: 1 From: 18

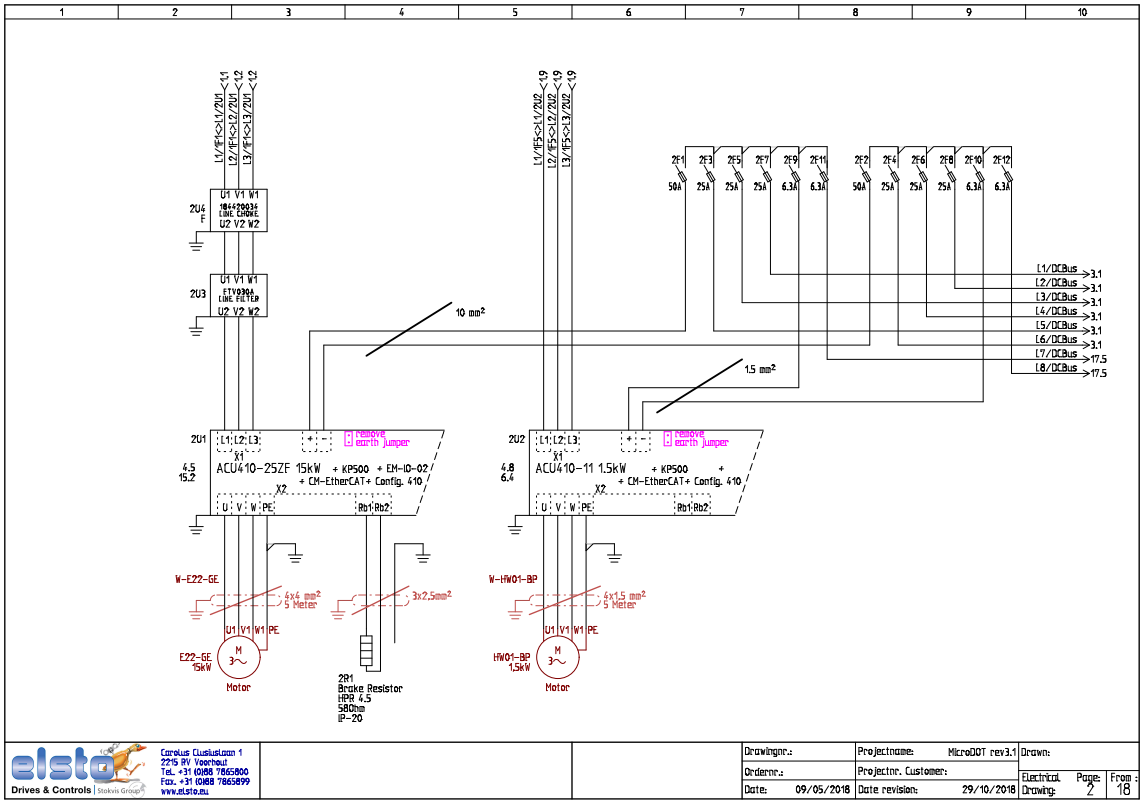
L1/1F4<>L1/2U1
L2/1F4<>L2/2U1
L3/1F4<>L3/2U1
L1/1F5<>L1/2U2
L2/1F5<>L2/2U2
L3/1F5<>L3/2U2
2U4
F
2U3
ETV030A
LINE FILTER
2E1
2E2
2E3
2E4
2E5
2E6
2E7
2E8
2E9
2E10
2E11
2E12
50A
25A
6.3A
L1/DCBus >3.1
L2/DCBus >3.1
L3/DCBus >3.1
L4/DCBus >3.1
L5/DCBus >3.1
L6/DCBus >3.1
L7/DCBus >17.5
L8/DCBus >17.5
10 mm²
1.5 mm²
2U1
2U2
ACU410-25ZF 15kW + KP500 + EM-IO-02
+ CM-EtherCAT+ Config. 410
ACU410-11 1.5kW + KP500 +
+ CM-EtherCAT+ Config. 410
remove earth jumper
W-E22-GE
4x4 mm²
5 Meter
3x2.5mm²
W-HW01-BP
4x1.5 mm²
E22-GE
15kW
HW01-BP
1,5kW
Motor
2R1
Brake Resistor
HPR 4.5
560hm
IP-20
Carelus Cluiskuiaan 1
2215 BV Voorhout
Tel. +31 (0)88 7865800
Fax. +31 (0)88 7865899
www.elsto.eu
Drawingnr.:
Ordernr.:
Date: 09/05/2018
Projectname: MicroDOT rev3.1
Projectnr. Customer:
Date revision: 29/10/2018
Drawn:
Electrical Drawing: Page: 2 From: 18

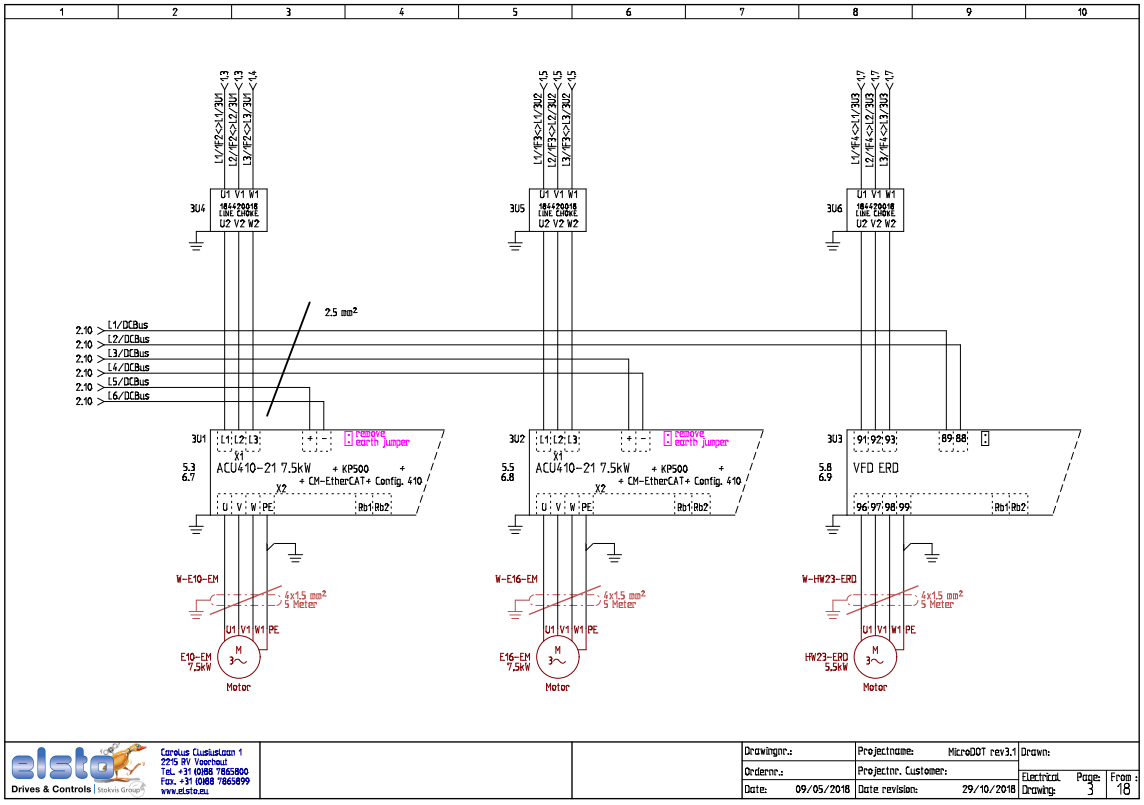
3U4
3U5
3U6
3U1
3U2
3U3
ACU410-21 7.5kW + KP500 + CM-EtherCAT+ Config. 410
VFD ERD
2.5 mm²
L1/DCBus
L2/DCBus
L3/DCBus
L4/DCBus
L5/DCBus
L6/DCBus
W-E10-EM
W-E16-EM
W-HW23-ERD
E10-EM 7,5kW
E16-EM 7,5kW
HW23-ERD 5,5kW
Motor
Drives & Controls
Drawingnr.:
Ordernr.:
Date: 09/05/2018
Projectname: MicroDOT rev3.1
Projectnr. Customer:
Date revision: 29/10/2018
Drawn:
Electrical Drawing: Page: 3 From: 18

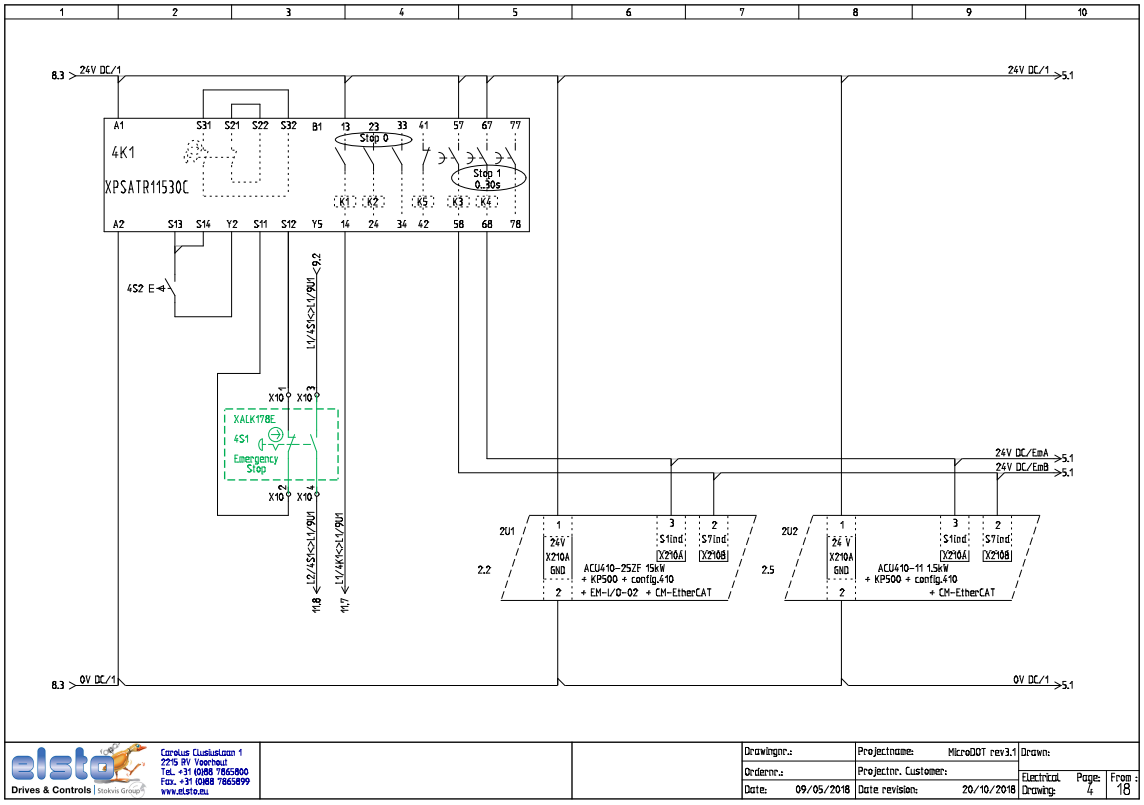
24V DC/1
0V DC/1
4K1
XPSATR11530C
Stop 0
Stop 1 0..30s
4S2
XALK178E
4S1
Emergency Stop
2U1
2U2
ACU410-25ZF 15kW + KP500 + config.410 + EM-I/O-02 + CM-EtherCAT
ACU410-11 1.5kW + KP500 + config.410 + CM-EtherCAT
24V DC/EmA
24V DC/EmB
Drives & Controls
Drawingnr.:
Ordernr.:
Date: 09/05/2018
Projectname: MicroDOT rev3.1
Projectnr. Customer:
Date revision: 20/10/2018
Drawn:
Electrical Drawing: Page: 4 From: 18

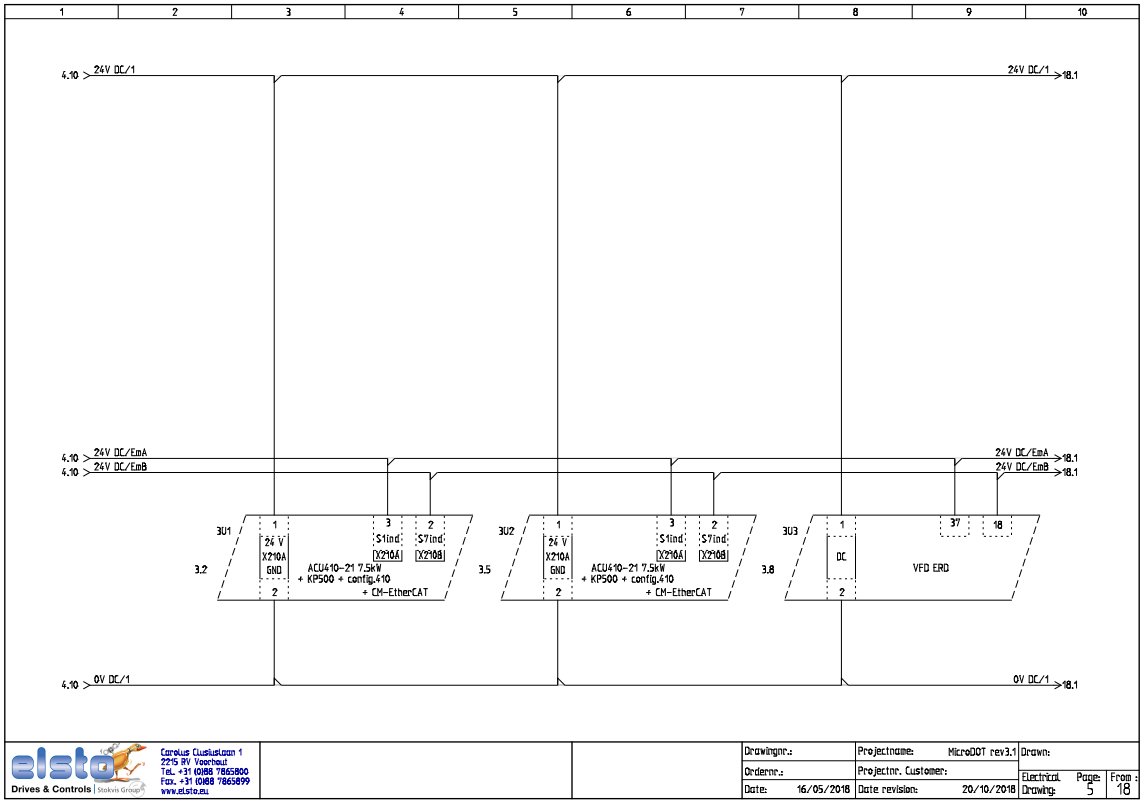
1 2 3 4 5 6 7 8 9 10
4.10 24V DC/1
24V DC/1 18.1
4.10 24V DC/EmA
4.10 24V DC/EmB
24V DC/EmA 18.1
24V DC/EmB 18.1
3U1
3.2
24 V
X210A
GND
S1ind
S2ind
X210B
ACU410-21 7.5kW
+ KP500 + config.410
+ CM-EtherCAT
3U2
3.5
3U3
3.8
DC
37
18
VFD ERD
4.10 0V DC/1
0V DC/1 18.1
Carelus Cluiskuilaan 1
2215 BV Voorhout
Tel. +31 (0)88 7865800
Fax. +31 (0)88 7865899
www.elsto.eu
Drawingnr.:
Ordernr.:
Date: 16/05/2018
Projectname: MicroDOT rev3.1
Projectnr. Customer:
Date revision: 20/10/2018
Drawn:
Electrical Drawing: Page: 5 From: 18

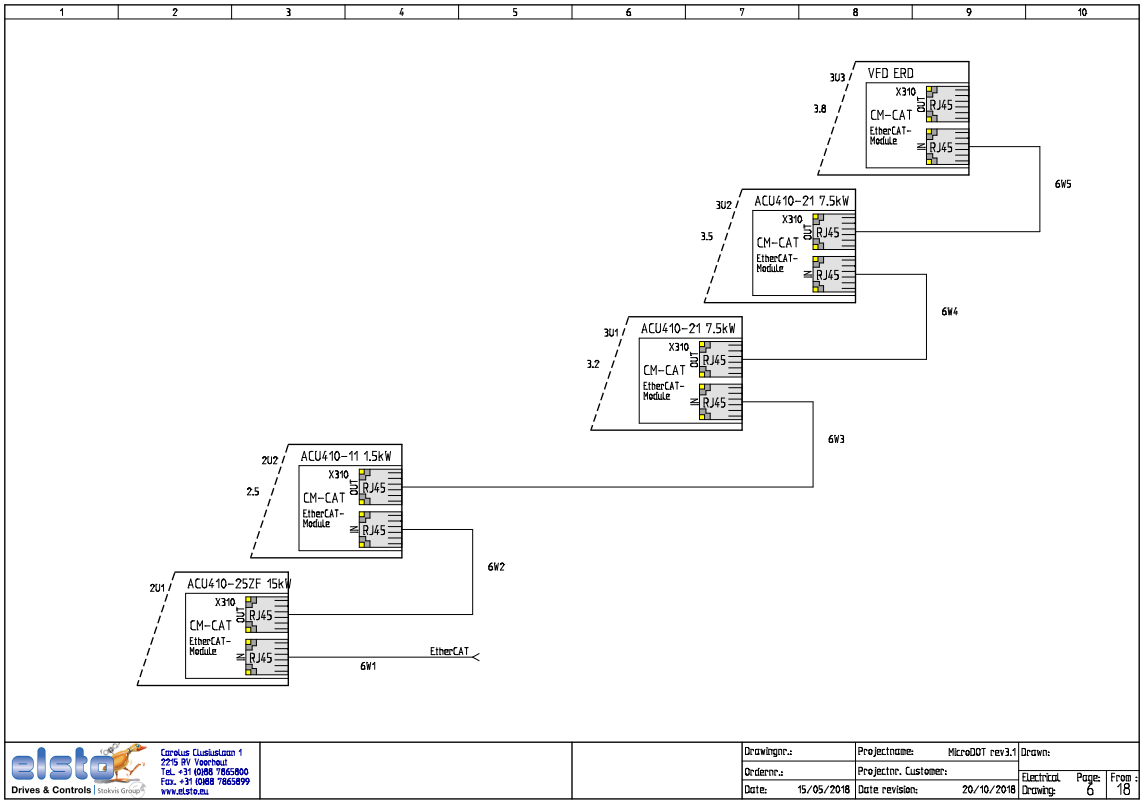
1 2 3 4 5 6 7 8 9 10
3U3
3.8
VFD ERD
X310
CM-CAT
EtherCAT-Module
OUT
IN
RJ45
6W5
3U2
3.5
ACU410-21 7.5kW
6W4
3U1
3.2
6W3
2U2
2.5
ACU410-11 1.5kW
6W2
2U1
ACU410-25ZF 15kW
EtherCAT
6W1
Carelus Cluiskuilaan 1
2215 BV Voorhout
Tel. +31 (0)88 7865800
Fax. +31 (0)88 7865899
www.elsto.eu
Drawingnr.:
Ordernr.:
Date: 15/05/2018
Projectname: MicroDOT rev3.1
Projectnr. Customer:
Date revision: 20/10/2018
Drawn:
Electrical Drawing: Page: 6 From: 18

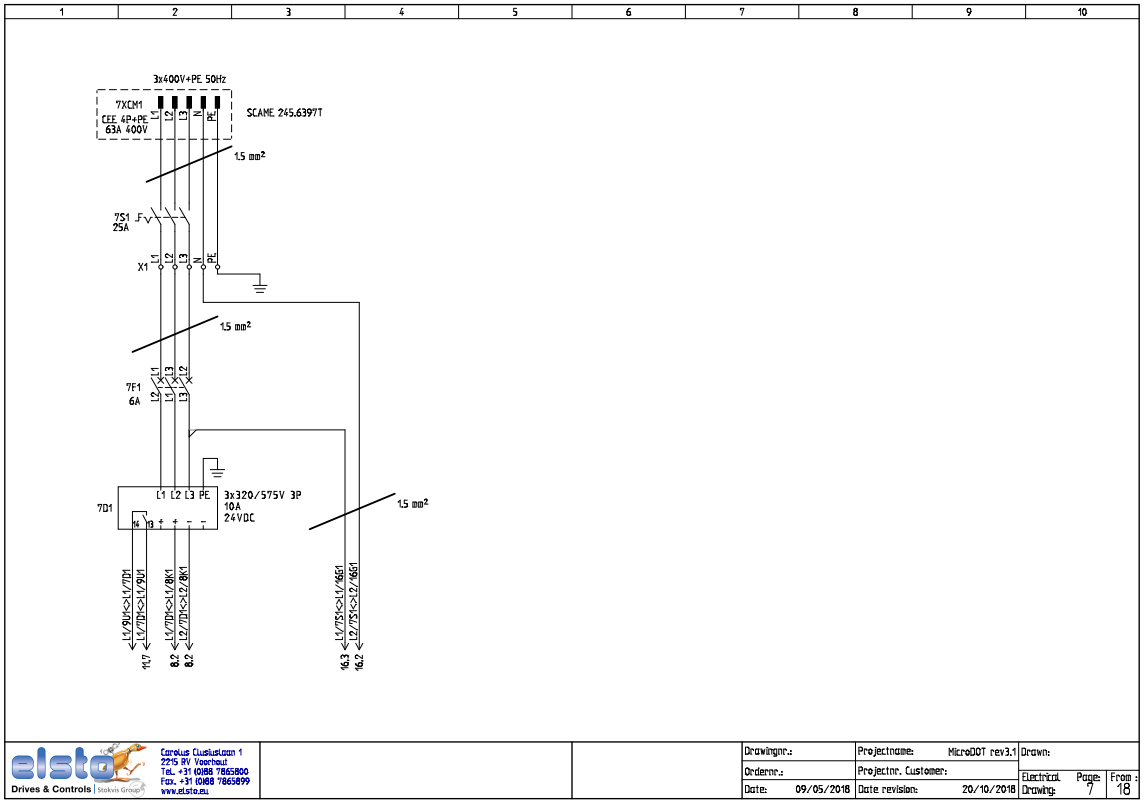
3x400V+PE 50Hz
7XCM1
CEE 4P+PE
63A 400V
SCAME 245.6397T
1.5 mm²
7S1
25A
X1
7F1
6A
7D1
3x320/575V 3P
10A
24VDC
1.5 mm²
Carolus Clusiuslaan 1
2215 BV Voorhout
Tel. +31 (0)88 7865800
Fax. +31 (0)88 7865899
www.elsto.eu
Drawingnr.:
Ordernr.:
Date: 09/05/2018
Projectname: MicroDOT rev3.1
Projectnr. Customer:
Date revision: 20/10/2018
Drawn:
Electrical Page: 7 From: 18
Drawing:

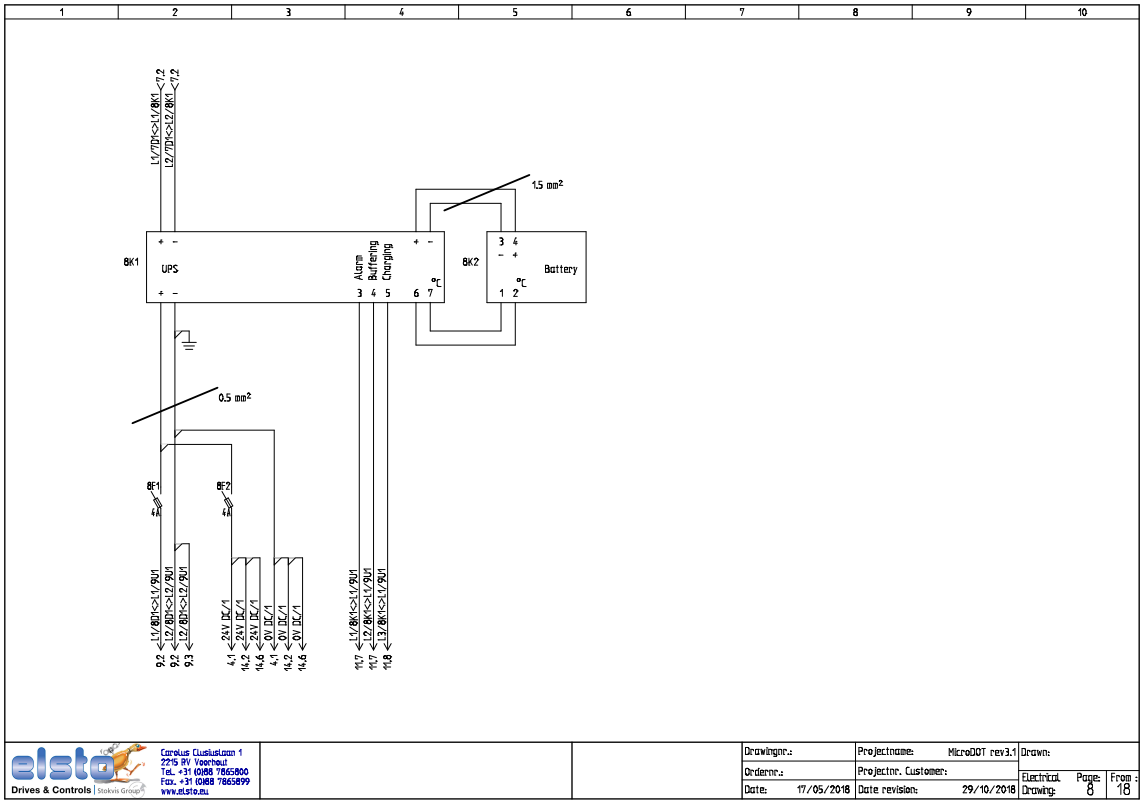
8K1
UPS
Alarm
Buffering
Charging
8K2
Battery
1.5 mm²
0.5 mm²
8F1
4A
8F2
4A
24V DC/1
Carolus Clusiuslaan 1
2215 BV Voorhout
Tel. +31 (0)88 7865800
Fax. +31 (0)88 7865899
www.elsto.eu
Drawingnr.:
Ordernr.:
Date: 17/05/2018
Projectname: MicroDOT rev3.1
Projectnr. Customer:
Date revision: 29/10/2018
Drawn:
Electrical Page: 8 From: 18
Drawing:

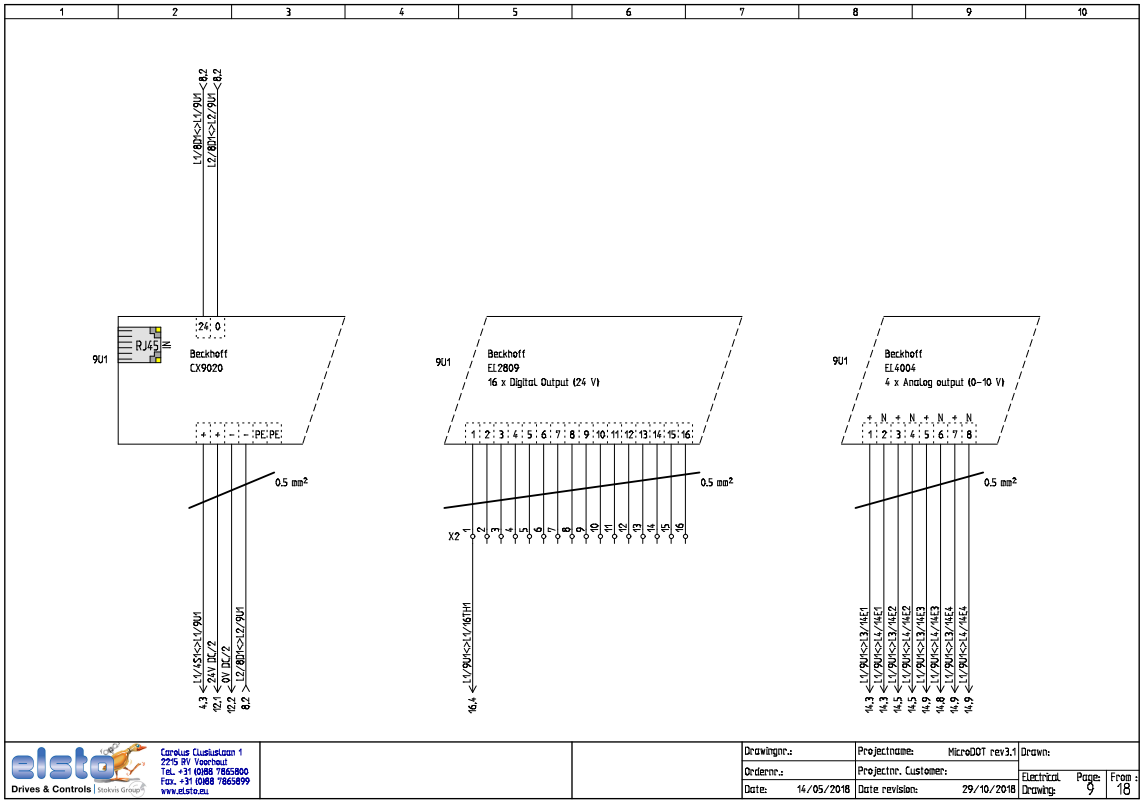
9U1
Beckhoff
CX9020
RJ45
24V 0
+ + - - PE PE
0.5 mm²
9U1
Beckhoff
EL2809
16 x Digital Output (24 V)
X2
9U1
Beckhoff
EL4004
4 x Analog output (0-10 V)
Carolus Clusiuslaan 1
2215 BV Voorhout
Tel. +31 (0)88 7865800
Fax. +31 (0)88 7865899
www.elsto.eu
Drawingnr.:
Ordernr.:
Date: 14/05/2018
Projectname: MicroDOT rev3.1
Projectnr. Customer:
Date revision: 29/10/2018
Drawn:
Electrical Drawing: Page: 9 From: 18

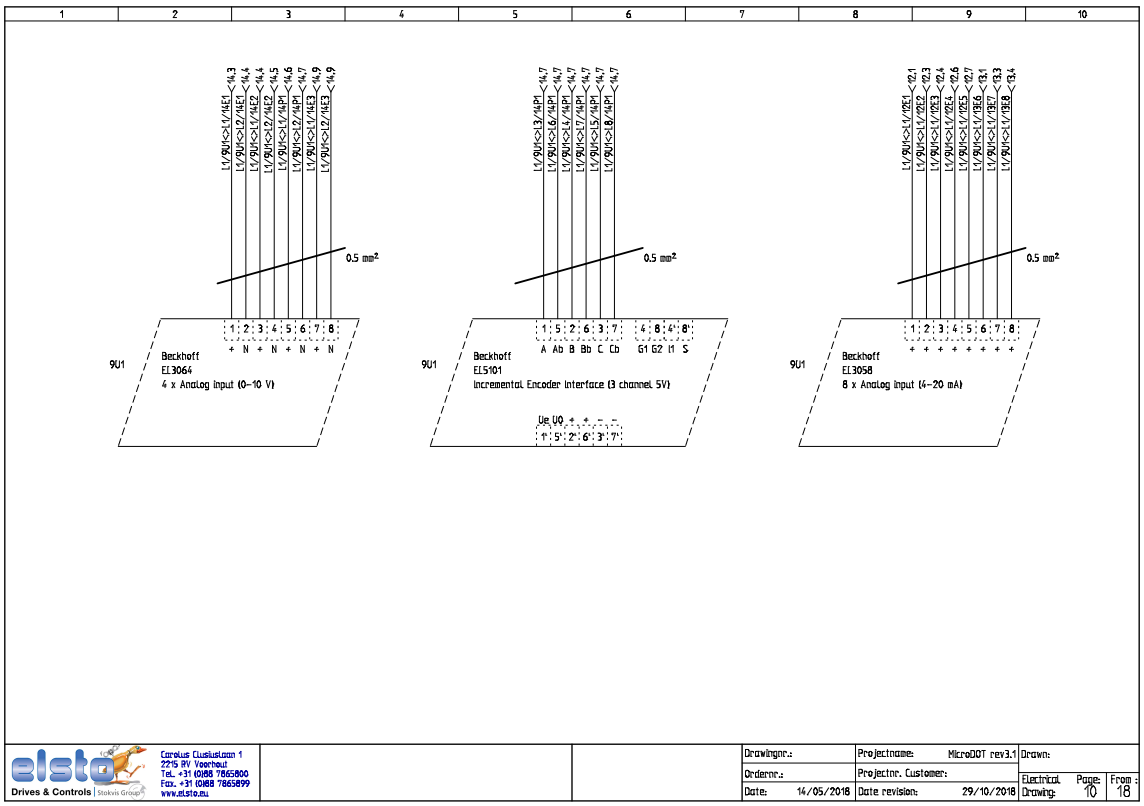
9U1
Beckhoff
EL3064
4 x Analog input (0-10 V)
0.5 mm²
9U1
Beckhoff
EL5101
Incremental Encoder interface (3 channel 5V)
A Ab B Bb C Cb G1 G2 M S
Ue U0
9U1
Beckhoff
EL3058
8 x Analog input (4-20 mA)
Carolus Clusiuslaan 1
2215 BV Voorhout
Tel. +31 (0)88 7865800
Fax. +31 (0)88 7865899
www.elsto.eu
Drawingnr.:
Ordernr.:
Date: 14/05/2018
Projectname: MicroDOT rev3.1
Projectnr. Customer:
Date revision: 29/10/2018
Drawn:
Electrical Drawing: Page: 10 From: 18

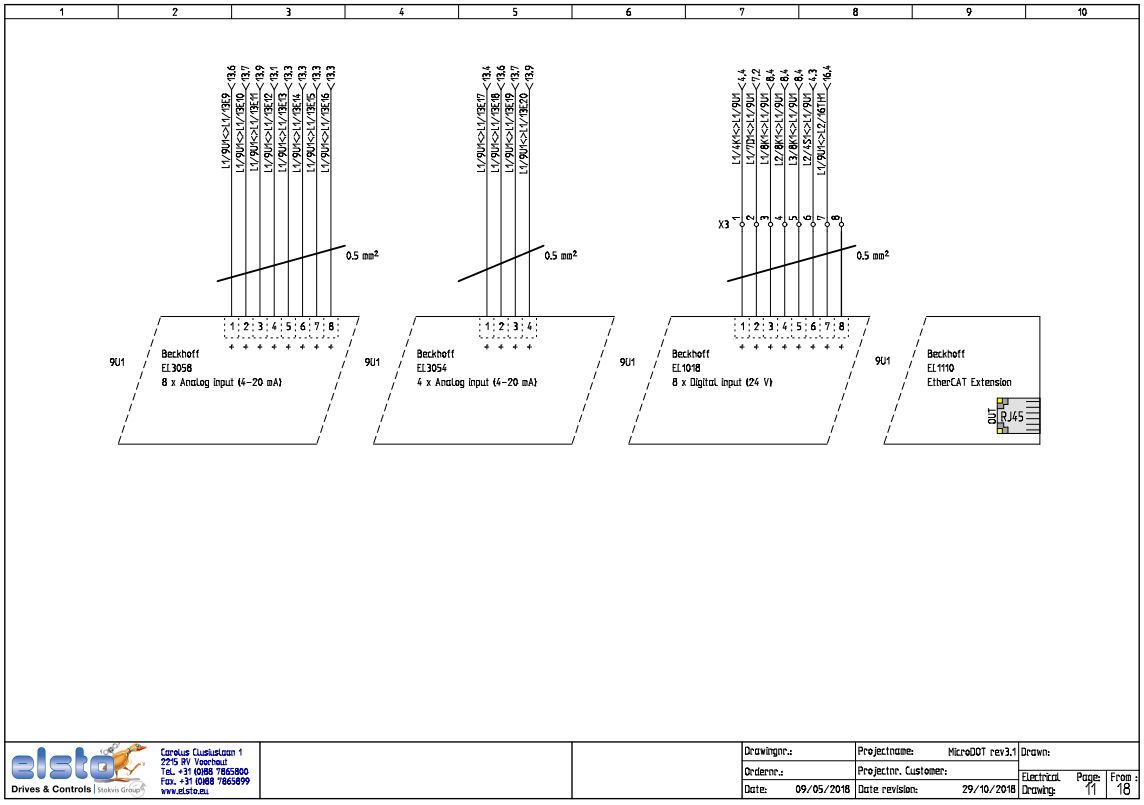
1 2 3 4 5 6 7 8 9 10
L1/9U1<>L1/12E9 13.6
L1/9U1<>L1/12E10 13.7
L1/9U1<>L1/12E11 13.9
L1/9U1<>L1/12E12 13.1
L1/9U1<>L1/12E13 13.3
L1/9U1<>L1/12E14 13.3
L1/9U1<>L1/12E15 13.3
L1/9U1<>L1/12E16 13.3
0.5 mm²
1 2 3 4 5 6 7 8
9U1
Beckhoff
EL3058
8 x Analog Input (4-20 mA)
L1/9U1<>L1/12E17 13.4
L1/9U1<>L1/12E18 13.6
L1/9U1<>L1/12E19 13.7
L1/9U1<>L1/12E20 13.9
0.5 mm²
1 2 3 4
9U1
Beckhoff
EL3054
4 x Analog Input (4-20 mA)
L1/4K1<>L1/9U1 4.4
L1/7D1<>L1/9U1 7.2
L1/8K1<>L1/9U1 8.4
L2/8K1<>L1/9U1 8.4
L3/8K1<>L1/9U1 8.4
L2/4S1<>L1/9U1 4.3
L1/9U1<>L2/4S1H1 16.4
X3
0.5 mm²
1 2 3 4 5 6 7 8
9U1
Beckhoff
EL1018
8 x Digital Input (24 V)
9U1
Beckhoff
EL1110
EtherCAT Extension
OUT
RJ45
Drawingnr.:
Ordernr.:
Date: 09/05/2018
Projectname: MicroDOT rev3.1
Projectnr. Customer:
Date revision: 29/10/2018
Drawn:
Electrical Page: 11 From: 18
Drawing:

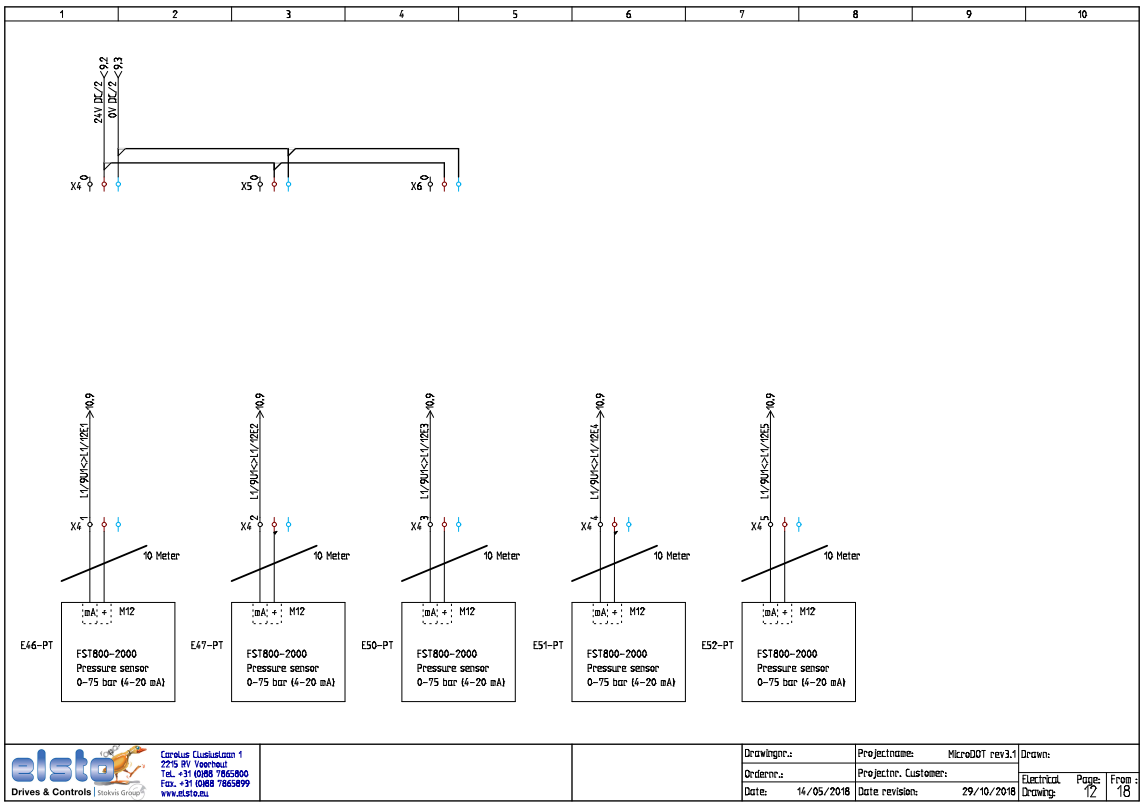
1 2 3 4 5 6 7 8 9 10
24V DC/2 0.2
0V DC/2 0.3
X4 9
X5 9
X6 9
L1/9U1<>L1/12E1 10.9
L1/9U1<>L1/12E2 10.9
L1/9U1<>L1/12E3 10.9
L1/9U1<>L1/12E4 10.9
L1/9U1<>L1/12E5 10.9
X4 1
X4 2
X4 3
X4 4
X4 5
10 Meter
mA + M12
E46-PT
E47-PT
E50-PT
E51-PT
E52-PT
FST800-2000
Pressure sensor
0-75 bar (4-20 mA)
Drawingnr.:
Ordernr.:
Date: 14/05/2018
Projectname: MicroDOT rev3.1
Projectnr. Customer:
Date revision: 29/10/2018
Drawn:
Electrical Page: 12 From: 18
Drawing:

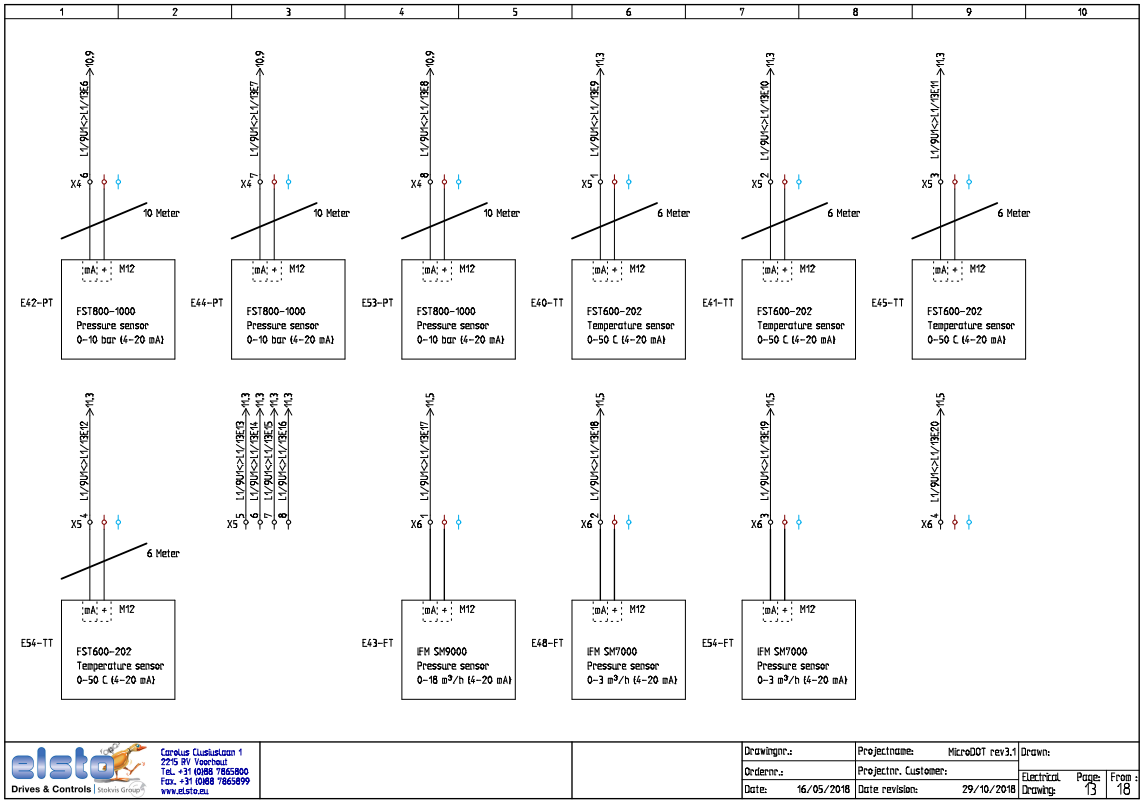
E42-PT
FST800-1000
Pressure sensor
0-10 bar (4-20 mA)
10 Meter
E44-PT
FST800-1000
Pressure sensor
0-10 bar (4-20 mA)
10 Meter
E53-PT
FST800-1000
Pressure sensor
0-10 bar (4-20 mA)
10 Meter
E40-TT
FST600-202
Temperature sensor
0-50 C (4-20 mA)
6 Meter
E41-TT
FST600-202
Temperature sensor
0-50 C (4-20 mA)
6 Meter
E45-TT
FST600-202
Temperature sensor
0-50 C (4-20 mA)
6 Meter
E54-TT
FST600-202
Temperature sensor
0-50 C (4-20 mA)
6 Meter
E43-FT
IFM SM9000
Pressure sensor
0-18 m³/h (4-20 mA)
E48-FT
IFM SM7000
Pressure sensor
0-3 m³/h (4-20 mA)
E54-FT
IFM SM7000
Pressure sensor
0-3 m³/h (4-20 mA)
Drawingnr.:
Projectname: MicroDOT rev3.1
Drawn:
Ordernr.:
Projectnr. Customer:
Date: 16/05/2018
Date revision: 29/10/2018
Electrical Drawing: Page: 13 From: 18

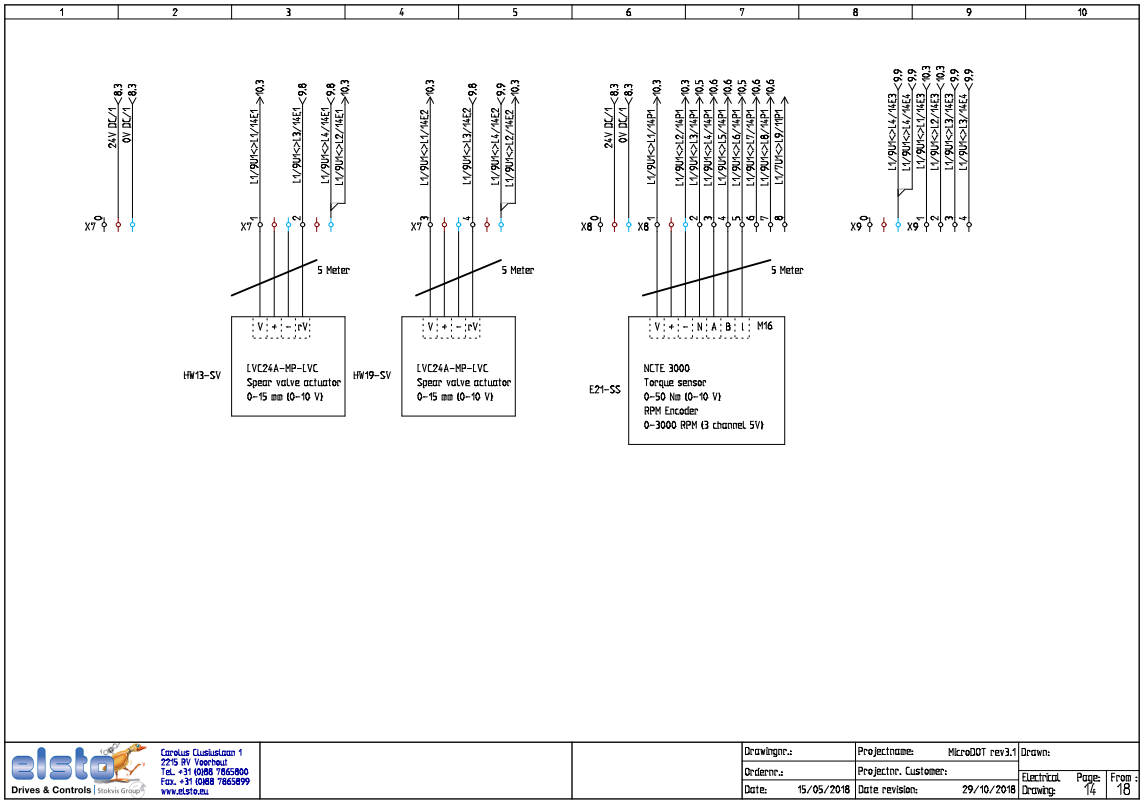
HW13-SV
LVC24A-MP-LVC
Spear valve actuator
0-15 mm (0-10 V)
5 Meter
HW19-SV
LVC24A-MP-LVC
Spear valve actuator
0-15 mm (0-10 V)
5 Meter
E21-SS
NCTE 3000
Torque sensor
0-50 Nm (0-10 V)
RPM Encoder
0-3000 RPM (3 channel 5V)
5 Meter
Drawingnr.:
Projectname: MicroDOT rev3.1
Drawn:
Ordernr.:
Projectnr. Customer:
Date: 15/05/2018
Date revision: 29/10/2018
Electrical Drawing: Page: 14 From: 18

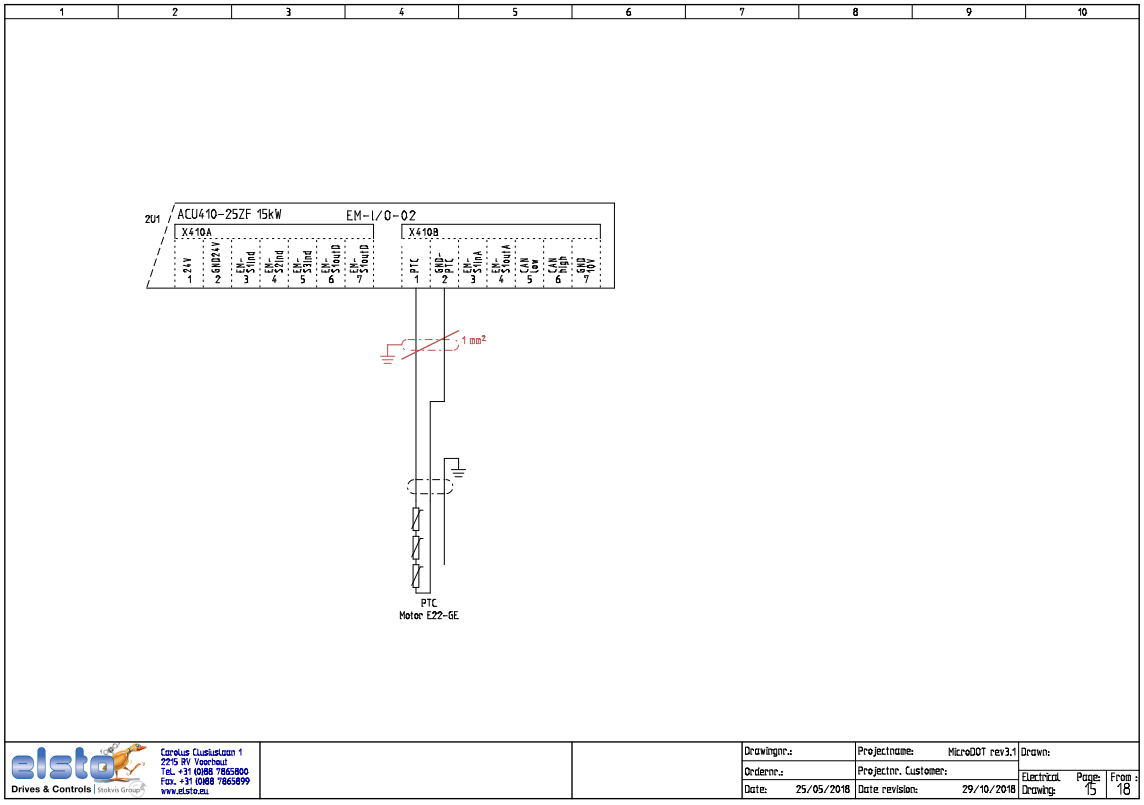
1 2 3 4 5 6 7 8 9 10
2U1
ACU410-25ZF 15kW
EM-I/O-02
X410A
X410B
1 24V
2 GND24V
3 EM-Sl1nd
4 EM-Sl2nd
5 EM-Sl3nd
6 EM-Shield
7 EM-Shield
1 PTC
2 GND-PTC
3 EM-Sl0ut
4 EM-Sl0ut\
5 CAN low
6 CAN high
7 GND 10V
1 mm²
PTC
Motor E22-6E
Carelus Cluiskuilaan 1
2215 BV Voorhout
Tel. +31 (0)88 7865800
Fax. +31 (0)88 7865899
www.elsto.eu
Drives & Controls | Stokvis Group
Drawingnr.:
Ordernr.:
Date: 25/05/2018
Projectname: MicroDOT rev3.1
Projectnr. Customer:
Date revision: 29/10/2018
Drawn:
Electrical Drawing
Page: 15
From: 18

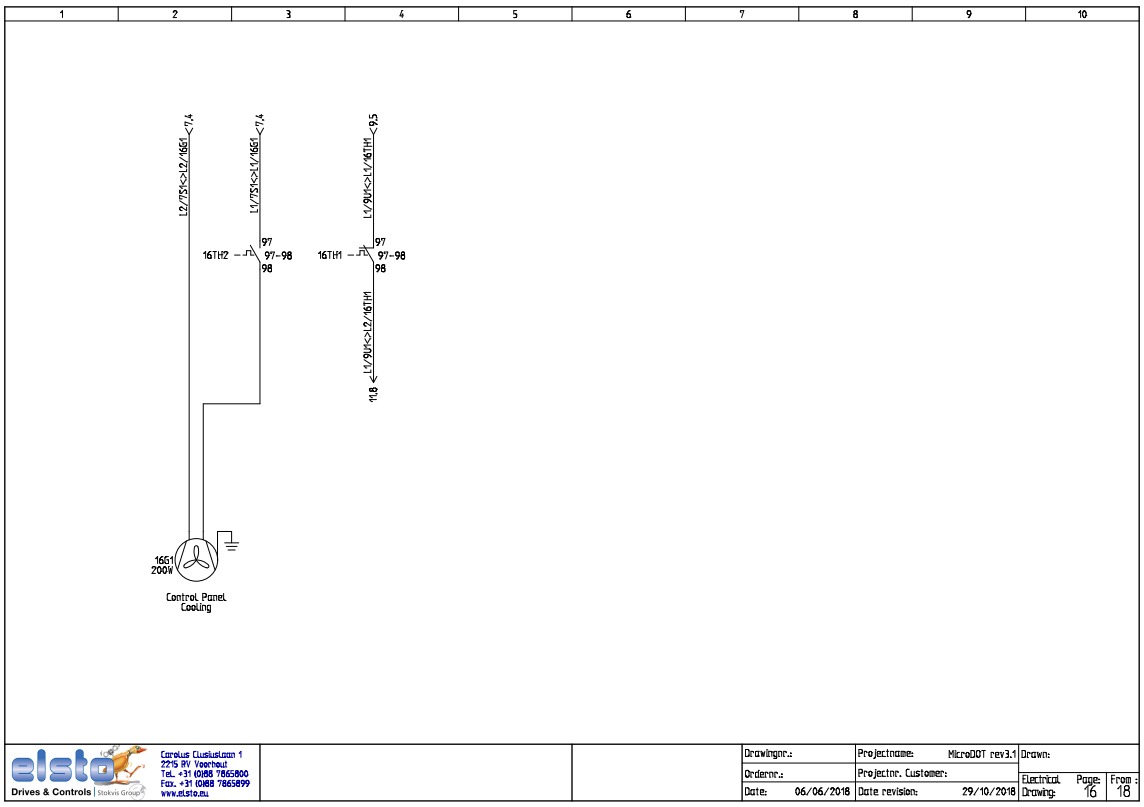
1 2 3 4 5 6 7 8 9 10
L2/75K>>L2/16SF 17.4
L1/75K>>L1/16SF 17.4
L1/90K>>L1/16TH1 19.5
97
97-98
98
16TH2
16TH1
L1/90K>>L2/16TH1
11.8
16SF
200W
Control Panel
Cooling
Carelus Cluiskuilaan 1
2215 BV Voorhout
Tel. +31 (0)88 7865800
Fax. +31 (0)88 7865899
www.elsto.eu
Drives & Controls | Stokvis Group
Drawingnr.:
Ordernr.:
Date: 06/06/2018
Projectname: MicroDOT rev3.1
Projectnr. Customer:
Date revision: 29/10/2018
Drawn:
Electrical Drawing
Page: 16
From: 18

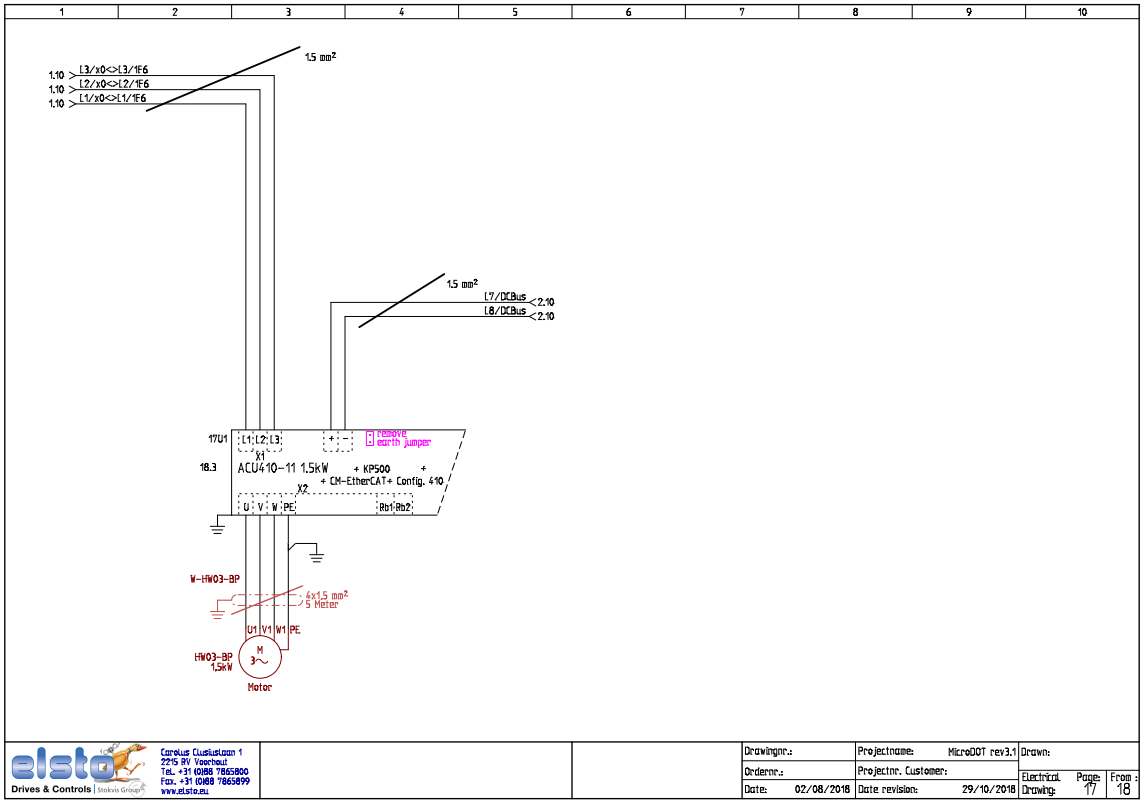
1 2 3 4 5 6 7 8 9 10
1.5 mm²
1.10 L3/x0<>L3/1F6
1.10 L2/x0<>L2/1F6
1.10 L1/x0<>L1/1F6
1.5 mm²
L7/DCBus 2.10
L8/DCBus 2.10
17U1
L1 L2 L3
X1
18.3
ACU410-11 1.5kW + KP500 + CM-EtherCAT+ Config. 410
X2
U V W PE Rb1 Rb2
Remove earth jumper
W-HW03-BP
4x1.5 mm²
5 Meter
U1 V1 W1 PE
HW03-BP
1.5kW
M
3~
Motor
Drawingnr.:
Ordernr.:
Date: 02/08/2018
Projectname: MicroDOT rev3.1
Projectnr. Customer:
Date revision: 29/10/2018
Drawn:
Electrical Page: 17 From: 18
Drawing:

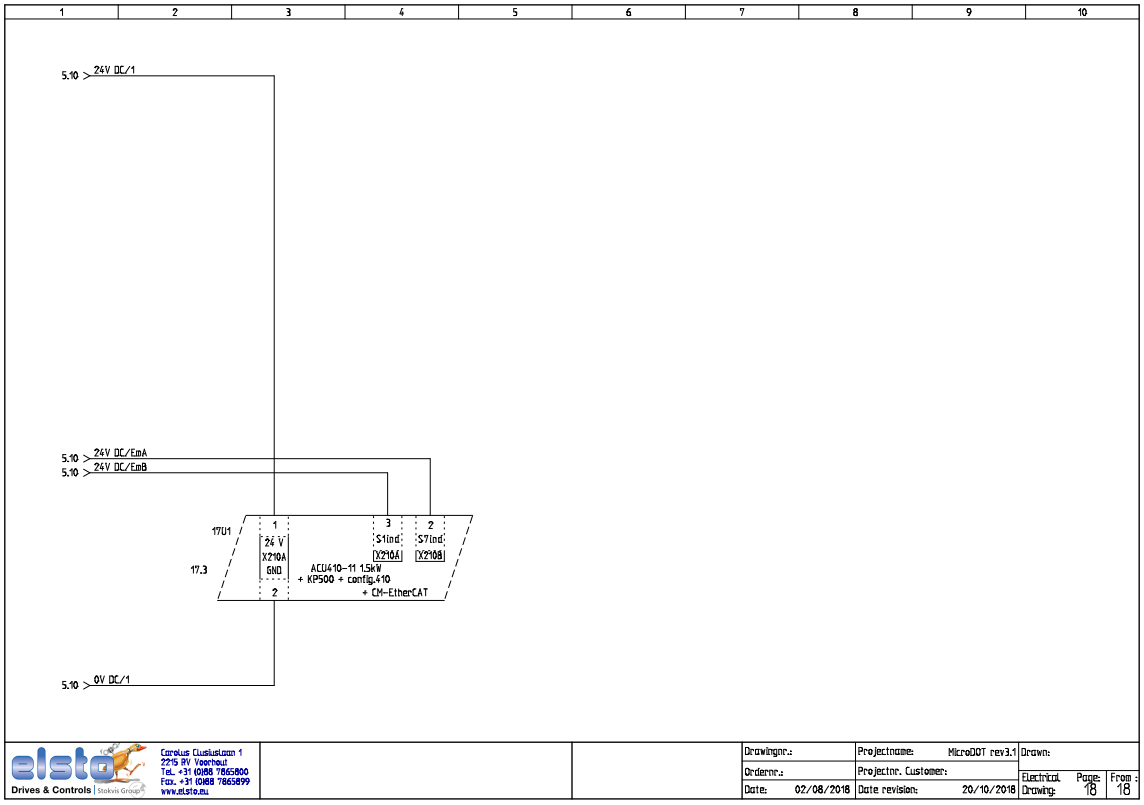
1 2 3 4 5 6 7 8 9 10
5.10 24V DC/1
5.10 24V DC/EmA
5.10 24V DC/EmB
17U1
1
24 V
X210A
GND
2
3
S1ind
X2104
2
S7ind
X2108
17.3
ACU410-11 1.5kW
+ KP500 + config.410
+ CM-EtherCAT
5.10 0V DC/1
Drawingnr.:
Ordernr.:
Date: 02/08/2018
Projectname: MicroDOT rev3.1
Projectnr. Customer:
Date revision: 20/10/2018
Drawn:
Electrical Page: 18 From: 18
Drawing:

Material-Detail

Comp	Type	Quantity	Description	Manufacturer
AKR1	NLS-CU 3/10 SN	270.00	7600984 Shield Collector rail , 3 mm X 10 mm	Phoenix Contact
ARS1	AB/SS-M	1.00	1730246 Support Foot Rack For Collector Rail	Phoenix Contact
ARS2	AB/SS-M	1.00	1730246 Support Foot Rack For Collector Rail	Phoenix Contact
E21-SS	NCTE 3000	1.00	Torque sensor with RPM encoder	NCTE
E40-TT	FST600-202	1.00	Temperature sensor	FirstRate
E41-TT	FST600-202	1.00	Temperature sensor	FirstRate
E42-PT	FST800-1000	1.00	Low pressure sensor	FirstRate
E43-FT	IFM SM9000	1.00		
E44-PT	FST800-1000	1.00	Low pressure sensor	FirstRate
E45-TT	FST600-202	1.00	Temperature sensor	FirstRate
E46-PT	FST800-2000	1.00	High pressure sensor	FirstRate
E47-PT	FST800-2000	1.00	High pressure sensor	FirstRate
E48-FT	IFM SM7000	1.00		
E50-PT	FST800-2000	1.00	High pressure sensor	FirstRate
E51-PT	FST800-2000	1.00	High pressure sensor	FirstRate
E52-PT	FST800-2000	1.00	High pressure sensor	FirstRate
E53-PT	FST800-1000	1.00	Low pressure sensor	FirstRate
E54-FT	IFM SM7000	1.00		
E54-TT	FST600-202	1.00	Temperature sensor	FirstRate
G3	NSYCAG294LPF	1.00	Exit Grill 336x316mm RAL7035	Schneider Electric
G4	ESG9/17K	1.00	1674760000 Label 9x17mm Adhesive For Transformer	WEIDMULLER B.V.
G4	NSYCAG294LPF	1.00	Exit Grill 336x316mm RAL7035	Schneider Electric
G4	NSYCVFB50M230PF	1.00	Ventilator 850m³/h 230VAC RAL7035	Schneider Electric
HW13-SV	LVC24A-NP-LVC	1.00	Spear valve actuator	Belimo
HW19-SV	LVC24A-NP-LVC	1.00	Spear valve actuator	Belimo
KK1	SK 35	1.00	1729829 Shielding 35mm Connector for rail	TU
KK2	SK 20	1.00	1728346 Shielding 20mm Connector for rail	TU
KK3	SK 20	1.00	1728346 Shielding 20mm Connector for rail	TU
KK4	SK 20	1.00	1728346 Shielding 20mm Connector for rail	TU
KK5	SK 20	1.00	1728346 Shielding 20mm Connector for rail	TU
KK6	SK 20	1.00	1728346 Shielding 20mm Connector for rail	TU

elsto Drives & Controls | Stokvis Groep
Cornelius Claeslaan 1
2215 BV Voorhout
Tel. +31 (0)88 7865800
Fax. +31 (0)88 7865899
www.elsto.eu

Drawingnr.:	Projectname: MicroDOT rev3.1	Drawn:	
Ordernr.:	Projectnr. Customer:	Mat. List	Page: 1 / From: 12
Date: 29/10/2018	Date revision:	Detail:	

Material-Detail

Comp	Type	Quantity	Description	Manufacturer
U7	34TS35F6	350.00	Din-Rail Perforated	Caipe
U8	34TS35F6	350.00	Din-Rail Perforated	Caipe
U11	34TS35F6	500.00	Din-Rail Perforated	Caipe
U14	34TS35F6	150.00	Din-Rail Perforated	Caipe
U25	34TS35F6	270.00	Din-Rail Perforated	Caipe
U27	B1465	1540.00	Wiring Gutter 60x60mm	Licatec
U28	B1465	1420.00	Wiring Gutter 60x60mm	Licatec
U30	B1465	232.50	Wiring Gutter 60x60mm	Licatec
U31	B1465	1540.00	Wiring Gutter 60x60mm	Licatec
U32	B1465	1300.00	Wiring Gutter 60x60mm	Licatec
U33	B1465	760.00	Wiring Gutter 60x60mm	Licatec
U34	B1465	1300.00	Wiring Gutter 60x60mm	Licatec
U39	B1464	1095.00	Wiring Gutter 60x40mm	Licatec
U40	34TS35F6	500.00	Din-Rail Perforated	Caipe
U41	34TS35F6	500.00	Din-Rail Perforated	Caipe
U42	B1464	500.00	Wiring Gutter 60x40mm	Licatec
U43	B1465	500.00	Wiring Gutter 60x60mm	Licatec
U44	B1465	760.00	Wiring Gutter 60x60mm	Licatec
U45	B1465	500.00	Wiring Gutter 60x60mm	Licatec
U46	34TS35F6	580.00	Din-Rail Perforated	Caipe
X0	DEK5/5MC	5.00	1609801044 Label 5x5mm For Terminal	WEIDMULLER B.V.
X0	ZDU35	5.00	1739620000 ZDU 35	WEIDMULLER B.V.
X1	DEK5/5MC	5.00	1609801044 Label 5x5mm For Terminal	WEIDMULLER B.V.
X1	ZDU4	3.00	1632050000 ZDU 4	WEIDMULLER B.V.
X1	ZDU4BL	1.00	1632060000 ZDU 4 BLUE	WEIDMULLER B.V.
X1	ZPE4	1.00	1632080000 ZPE 4	WEIDMULLER B.V.
X2	DEK5/5MC	16.00	1609801044 Label 5x5mm For Terminal	WEIDMULLER B.V.
X2	ZDU2.5	16.00	1608510000 ZDU 2.5/E	WEIDMULLER B.V.
X3	DEK5/5MC	22.00	1609801044 Label 5x5mm For Terminal	WEIDMULLER B.V.
X3	ZDU2.5	10.00	1608510000 ZDU 2.5/E	WEIDMULLER B.V.
X3	ZIA1.5/3L-1S	6.00	1651980000 ZIA 1.5/3L-1S	WEIDMULLER B.V.

elsto Drives & Controls | Stokvis Groep
Cornelius Claeslaan 1
2215 BV Voorhout
Tel. +31 (0)88 7865800
Fax. +31 (0)88 7865899
www.elsto.eu

Drawingnr.:	Projectname: MicroDOT rev3.1	Drawn:	
Ordernr.:	Projectnr. Customer:	Mat. List	Page: 2 / From: 12
Date: 29/10/2018	Date revision:	Detail:	

Material-Detail

Comp	Type	Quantity	Description	Manufacturer
X3	ZVL1.5BL	6.00	1650360000 ZVL1.5BL	WEIDMULLER B.V.
X3	ZVL1.5BR	6.00	1650370000 ZVL1.5BR	WEIDMULLER B.V.
X4	DEK5/5MC	2.00	1609801044 Label 5x5mm For Terminal	WEIDMULLER B.V.
X4	DEK5/5MC	2.00	1609801044 Label 5x5mm For Terminal	WEIDMULLER B.V.
X4	DEK5/5MC	2.00	1609801044 Label 5x5mm For Terminal	WEIDMULLER B.V.
X4	DEK5/5MC	2.00	1609801044 Label 5x5mm For Terminal	WEIDMULLER B.V.
X4	DEK5/5MC	2.00	1609801044 Label 5x5mm For Terminal	WEIDMULLER B.V.
X4	DEK5/5MC	2.00	1609801044 Label 5x5mm For Terminal	WEIDMULLER B.V.
X4	DEK5/5MC	2.00	1609801044 Label 5x5mm For Terminal	WEIDMULLER B.V.
X4	DEK5/5MC	2.00	1609801044 Label 5x5mm For Terminal	WEIDMULLER B.V.
X4	ZIA1.5/3L-1S	1.00	1651980000 ZIA 1.5/3L-1S	WEIDMULLER B.V.
X4	ZIA1.5/3L-1S	1.00	1651980000 ZIA 1.5/3L-1S	WEIDMULLER B.V.
X4	ZIA1.5/3L-1S	1.00	1651980000 ZIA 1.5/3L-1S	WEIDMULLER B.V.
X4	ZIA1.5/3L-1S	1.00	1651980000 ZIA 1.5/3L-1S	WEIDMULLER B.V.
X4	ZIA1.5/3L-1S	1.00	1651980000 ZIA 1.5/3L-1S	WEIDMULLER B.V.
X4	ZIA1.5/3L-1S	1.00	1651980000 ZIA 1.5/3L-1S	WEIDMULLER B.V.
X4	ZIA1.5/3L-1S	1.00	1651980000 ZIA 1.5/3L-1S	WEIDMULLER B.V.
X4	ZIA1.5/3L-1S	1.00	1651980000 ZIA 1.5/3L-1S	WEIDMULLER B.V.
X4	ZIA1.5/3L-1S	1.00	1651980000 ZIA 1.5/3L-1S	WEIDMULLER B.V.
X4	ZVL1.5BL	1.00	1650360000 ZVL1.5BL	WEIDMULLER B.V.
X4	ZVL1.5BL	1.00	1650360000 ZVL1.5BL	WEIDMULLER B.V.
X4	ZVL1.5BL	1.00	1650360000 ZVL1.5BL	WEIDMULLER B.V.
X4	ZVL1.5BL	1.00	1650360000 ZVL1.5BL	WEIDMULLER B.V.
X4	ZVL1.5BL	1.00	1650360000 ZVL1.5BL	WEIDMULLER B.V.
X4	ZVL1.5BL	1.00	1650360000 ZVL1.5BL	WEIDMULLER B.V.
X4	ZVL1.5BL	1.00	1650360000 ZVL1.5BL	WEIDMULLER B.V.
X4	ZVL1.5BL	1.00	1650360000 ZVL1.5BL	WEIDMULLER B.V.
X4	ZVL1.5BL	1.00	1650360000 ZVL1.5BL	WEIDMULLER B.V.
X4	ZVL1.5BR	1.00	1650370000 ZVL1.5BR	WEIDMULLER B.V.
X4	ZVL1.5BR	1.00	1650370000 ZVL1.5BR	WEIDMULLER B.V.

elsto Drives & Controls | Stokvis Groep
Cornelius Claeslaan 1
2215 BV Voorhout
Tel. +31 (0)88 7865800
Fax. +31 (0)88 7865899
www.elsto.eu

Drawingnr.:	Projectname: MicroDOT rev3.1	Drawn:	
Ordernr.:	Projectnr. Customer:	Mat. List	Page: 3 / From: 12
Date: 29/10/2018	Date revision:	Detail:	

Material-Detail

Comp	Type	Quantity	Description	Manufacturer
X4	ZVL1.5BR	1.00	1650370000 ZVL1.5BR	WEIDMULLER B.V.
X4	ZVL1.5BR	1.00	1650370000 ZVL1.5BR	WEIDMULLER B.V.
X4	ZVL1.5BR	1.00	1650370000 ZVL1.5BR	WEIDMULLER B.V.
X4	ZVL1.5BR	1.00	1650370000 ZVL1.5BR	WEIDMULLER B.V.
X4	ZVL1.5BR	1.00	1650370000 ZVL1.5BR	WEIDMULLER B.V.
X4	ZVL1.5BR	1.00	1650370000 ZVL1.5BR	WEIDMULLER B.V.
X4	ZVL1.5BR	1.00	1650370000 ZVL1.5BR	WEIDMULLER B.V.
X5	DEK5/5MC	2.00	1609801044 Label 5x5mm For Terminal	WEIDMULLER B.V.
X5	DEK5/5MC	1.00	1609801044 Label 5x5mm For Terminal	WEIDMULLER B.V.
X5	DEK5/5MC	2.00	1609801044 Label 5x5mm For Terminal	WEIDMULLER B.V.
X5	DEK5/5MC	2.00	1609801044 Label 5x5mm For Terminal	WEIDMULLER B.V.
X5	DEK5/5MC	2.00	1609801044 Label 5x5mm For Terminal	WEIDMULLER B.V.
X5	DEK5/5MC	2.00	1609801044 Label 5x5mm For Terminal	WEIDMULLER B.V.
X5	DEK5/5MC	2.00	1609801044 Label 5x5mm For Terminal	WEIDMULLER B.V.
X5	DEK5/5MC	4.00	1609801044 Label 5x5mm For Terminal	WEIDMULLER B.V.
X5	DEK5/5MC	2.00	1609801044 Label 5x5mm For Terminal	WEIDMULLER B.V.
X5	DEK5/5MC	2.00	1609801044 Label 5x5mm For Terminal	WEIDMULLER B.V.
X5	ZDU2.5	1.00	1608510000 ZDU 2.5/E	WEIDMULLER B.V.
X5	ZIA1.5/3L-1S	2.00	1651980000 ZIA 1.5/3L-1S	WEIDMULLER B.V.
X5	ZIA1.5/3L-1S	1.00	1651980000 ZIA 1.5/3L-1S	WEIDMULLER B.V.
X5	ZIA1.5/3L-1S	1.00	1651980000 ZIA 1.5/3L-1S	WEIDMULLER B.V.
X5	ZIA1.5/3L-1S	1.00	1651980000 ZIA 1.5/3L-1S	WEIDMULLER B.V.
X5	ZIA1.5/3L-1S	1.00	1651980000 ZIA 1.5/3L-1S	WEIDMULLER B.V.
X5	ZIA1.5/3L-1S	1.00	1651980000 ZIA 1.5/3L-1S	WEIDMULLER B.V.
X5	ZIA1.5/3L-1S	1.00	1651980000 ZIA 1.5/3L-1S	WEIDMULLER B.V.
X5	ZIA1.5/3L-1S	1.00	1651980000 ZIA 1.5/3L-1S	WEIDMULLER B.V.
X5	ZVL1.5BL	1.00	1650360000 ZVL1.5BL	WEIDMULLER B.V.
X5	ZVL1.5BL	2.00	1650360000 ZVL1.5BL	WEIDMULLER B.V.
X5	ZVL1.5BL	1.00	1650360000 ZVL1.5BL	WEIDMULLER B.V.
X5	ZVL1.5BL	1.00	1650360000 ZVL1.5BL	WEIDMULLER B.V.

elsto Drives & Controls | Stokvis Groep
Cornelius Claeslaan 1
2215 BV Voorhout
Tel. +31 (0)88 7865800
Fax. +31 (0)88 7865899
www.elsto.eu

Drawingnr.:	Projectname: MicroDOT rev3.1	Drawn:	
Ordernr.:	Projectnr. Customer:	Mat. List	Page: 4 / From: 12
Date: 29/10/2018	Date revision:	Detail:	

Material-Detail

Comp	Type	Quantity	Description	Manufacturer
X5	ZVL1.5BL	1.00	1650360000 ZVL1.5BL	WEIDMULLER B.V.
X5	ZVL1.5BL	1.00	1650360000 ZVL1.5BL	WEIDMULLER B.V.
X5	ZVL1.5BL	1.00	1650360000 ZVL1.5BL	WEIDMULLER B.V.
X5	ZVL1.5BL	1.00	1650360000 ZVL1.5BL	WEIDMULLER B.V.
X5	ZVL1.5BL	1.00	1650360000 ZVL1.5BL	WEIDMULLER B.V.
X5	ZVL1.5BR	1.00	1650370000 ZVL1.5BR	WEIDMULLER B.V.
X5	ZVL1.5BR	1.00	1650370000 ZVL1.5BR	WEIDMULLER B.V.
X5	ZVL1.5BR	1.00	1650370000 ZVL1.5BR	WEIDMULLER B.V.
X5	ZVL1.5BR	2.00	1650370000 ZVL1.5BR	WEIDMULLER B.V.
X5	ZVL1.5BR	1.00	1650370000 ZVL1.5BR	WEIDMULLER B.V.
X5	ZVL1.5BR	1.00	1650370000 ZVL1.5BR	WEIDMULLER B.V.
X5	ZVL1.5BR	1.00	1650370000 ZVL1.5BR	WEIDMULLER B.V.
X5	ZVL1.5BR	1.00	1650370000 ZVL1.5BR	WEIDMULLER B.V.
X5	ZVL1.5BR	1.00	1650370000 ZVL1.5BR	WEIDMULLER B.V.
X6	DEK5/5MC	2.00	1609801044 Label 5x5mm For Terminal	WEIDMULLER B.V.
X6	DEK5/5MC	2.00	1609801044 Label 5x5mm For Terminal	WEIDMULLER B.V.
X6	DEK5/5MC	2.00	1609801044 Label 5x5mm For Terminal	WEIDMULLER B.V.
X6	DEK5/5MC	4.00	1609801044 Label 5x5mm For Terminal	WEIDMULLER B.V.
X6	DEK5/5MC	2.00	1609801044 Label 5x5mm For Terminal	WEIDMULLER B.V.
X6	ZIA1.5/3L-1S	2.00	1651980000 ZIA 1.5/3L-1S	WEIDMULLER B.V.
X6	ZIA1.5/3L-1S	1.00	1651980000 ZIA 1.5/3L-1S	WEIDMULLER B.V.
X6	ZIA1.5/3L-1S	1.00	1651980000 ZIA 1.5/3L-1S	WEIDMULLER B.V.
X6	ZIA1.5/3L-1S	1.00	1651980000 ZIA 1.5/3L-1S	WEIDMULLER B.V.
X6	ZIA1.5/3L-1S	1.00	1651980000 ZIA 1.5/3L-1S	WEIDMULLER B.V.
X6	ZVL1.5BL	2.00	1650360000 ZVL1.5BL	WEIDMULLER B.V.
X6	ZVL1.5BL	1.00	1650360000 ZVL1.5BL	WEIDMULLER B.V.
X6	ZVL1.5BL	1.00	1650360000 ZVL1.5BL	WEIDMULLER B.V.
X6	ZVL1.5BL	1.00	1650360000 ZVL1.5BL	WEIDMULLER B.V.
X6	ZVL1.5BL	1.00	1650360000 ZVL1.5BL	WEIDMULLER B.V.
X6	ZVL1.5BR	1.00	1650370000 ZVL1.5BR	WEIDMULLER B.V.
X6	ZVL1.5BR	1.00	1650370000 ZVL1.5BR	WEIDMULLER B.V.

elsto Drives & Controls | Stokvis Groep
Cornelius Claeslaan 1
2215 BV Voorhout
Tel. +31 (0)88 7865800
Fax. +31 (0)88 7865899
www.elsto.eu

Drawingnr.:	Projectname: MicroDOT rev3.1	Drawn:	
Ordernr.:	Projectnr. Customer:	Mat. List	Page: 5 / From: 12
Date: 29/10/2018	Date revision:	Detail:	

Material-Detail

Comp	Type	Quantity	Description	Manufacturer
X6	ZVL1.5BR	1.00	1650370000 ZVL1.5BR	WEIDMULLER B.V.
X6	ZVL1.5BR	1.00	1650370000 ZVL1.5BR	WEIDMULLER B.V.
X6	ZVL1.5BR	2.00	1650370000 ZVL1.5BR	WEIDMULLER B.V.
X7	DEK5/5MC	2.00	1609801044 Label 5x5mm For Terminal	WEIDMULLER B.V.
X7	DEK5/5MC	2.00	1609801044 Label 5x5mm For Terminal	WEIDMULLER B.V.
X7	DEK5/5MC	2.00	1609801044 Label 5x5mm For Terminal	WEIDMULLER B.V.
X7	DEK5/5MC	2.00	1609801044 Label 5x5mm For Terminal	WEIDMULLER B.V.
X7	DEK5/5MC	2.00	1609801044 Label 5x5mm For Terminal	WEIDMULLER B.V.
X7	ZIA1.5/3L-1S	1.00	1651980000 ZIA 1.5/3L-1S	WEIDMULLER B.V.
X7	ZIA1.5/3L-1S	1.00	1651980000 ZIA 1.5/3L-1S	WEIDMULLER B.V.
X7	ZIA1.5/3L-1S	1.00	1651980000 ZIA 1.5/3L-1S	WEIDMULLER B.V.
X7	ZIA1.5/3L-1S	1.00	1651980000 ZIA 1.5/3L-1S	WEIDMULLER B.V.
X7	ZIA1.5/3L-1S	1.00	1651980000 ZIA 1.5/3L-1S	WEIDMULLER B.V.
X7	ZVL1.5BL	1.00	1650360000 ZVL1.5BL	WEIDMULLER B.V.
X7	ZVL1.5BL	1.00	1650360000 ZVL1.5BL	WEIDMULLER B.V.
X7	ZVL1.5BL	1.00	1650360000 ZVL1.5BL	WEIDMULLER B.V.
X7	ZVL1.5BL	1.00	1650360000 ZVL1.5BL	WEIDMULLER B.V.
X7	ZVL1.5BL	1.00	1650360000 ZVL1.5BL	WEIDMULLER B.V.
X7	ZVL1.5BR	1.00	1650370000 ZVL1.5BR	WEIDMULLER B.V.
X7	ZVL1.5BR	1.00	1650370000 ZVL1.5BR	WEIDMULLER B.V.
X7	ZVL1.5BR	1.00	1650370000 ZVL1.5BR	WEIDMULLER B.V.
X7	ZVL1.5BR	1.00	1650370000 ZVL1.5BR	WEIDMULLER B.V.
X7	ZVL1.5BR	1.00	1650370000 ZVL1.5BR	WEIDMULLER B.V.
X8	DEK5/5MC	8.00	1609801044 Label 5x5mm For Terminal	WEIDMULLER B.V.
X8	DEK5/5MC	2.00	1609801044 Label 5x5mm For Terminal	WEIDMULLER B.V.
X8	DEK5/5MC	2.00	1609801044 Label 5x5mm For Terminal	WEIDMULLER B.V.
X8	DEK5/5MC	2.00	1609801044 Label 5x5mm For Terminal	WEIDMULLER B.V.
X8	DEK5/5MC	2.00	1609801044 Label 5x5mm For Terminal	WEIDMULLER B.V.
X8	DEK5/5MC	2.00	1609801044 Label 5x5mm For Terminal	WEIDMULLER B.V.
X8	DEK5/5MC	2.00	1609801044 Label 5x5mm For Terminal	WEIDMULLER B.V.
X8	ZIA1.5/3L-1S	1.00	1651980000 ZIA 1.5/3L-1S	WEIDMULLER B.V.

elsto Drives & Controls | Stokvis Groep
Cornelius Claeslaan 1
2215 BV Voorhout
Tel. +31 (0)88 7865800
Fax. +31 (0)88 7865899
www.elsto.eu

Drawingnr.:	Projectname: MicroDOT rev3.1	Drawn:	
Ordernr.:	Projectnr. Customer:	Mat. List	Page: 6 / From: 12
Date: 29/10/2018	Date revision:	Detail:	

Material-Detail

Comp	Type	Quantity	Description	Manufacturer
X8	ZIA1.5/3L-1S	1.00	1651980000 ZIA 1.5/3L-1S	WEIDMULLER B.V.
X8	ZIA1.5/3L-1S	4.00	1651980000 ZIA 1.5/3L-1S	WEIDMULLER B.V.
X8	ZIA1.5/3L-1S	1.00	1651980000 ZIA 1.5/3L-1S	WEIDMULLER B.V.
X8	ZIA1.5/3L-1S	1.00	1651980000 ZIA 1.5/3L-1S	WEIDMULLER B.V.
X8	ZIA1.5/3L-1S	1.00	1651980000 ZIA 1.5/3L-1S	WEIDMULLER B.V.
X8	ZIA1.5/3L-1S	1.00	1651980000 ZIA 1.5/3L-1S	WEIDMULLER B.V.
X8	ZVL1.5BL	1.00	1650360000 ZVL1.5BL	WEIDMULLER B.V.
X8	ZVL1.5BL	1.00	1650360000 ZVL1.5BL	WEIDMULLER B.V.
X8	ZVL1.5BL	1.00	1650360000 ZVL1.5BL	WEIDMULLER B.V.
X8	ZVL1.5BL	1.00	1650360000 ZVL1.5BL	WEIDMULLER B.V.
X8	ZVL1.5BL	1.00	1650360000 ZVL1.5BL	WEIDMULLER B.V.
X8	ZVL1.5BL	1.00	1650360000 ZVL1.5BL	WEIDMULLER B.V.
X8	ZVL1.5BL	4.00	1650360000 ZVL1.5BL	WEIDMULLER B.V.
X8	ZVL1.5BR	1.00	1650370000 ZVL1.5BR	WEIDMULLER B.V.
X8	ZVL1.5BR	1.00	1650370000 ZVL1.5BR	WEIDMULLER B.V.
X8	ZVL1.5BR	1.00	1650370000 ZVL1.5BR	WEIDMULLER B.V.
X8	ZVL1.5BR	4.00	1650370000 ZVL1.5BR	WEIDMULLER B.V.
X8	ZVL1.5BR	1.00	1650370000 ZVL1.5BR	WEIDMULLER B.V.
X8	ZVL1.5BR	1.00	1650370000 ZVL1.5BR	WEIDMULLER B.V.
X8	ZVL1.5BR	1.00	1650370000 ZVL1.5BR	WEIDMULLER B.V.
X9	DEK5/5MC	2.00	1609801044 Label 5x5mm For Terminal	WEIDMULLER B.V.
X9	DEK5/5MC	2.00	1609801044 Label 5x5mm For Terminal	WEIDMULLER B.V.
X9	DEK5/5MC	2.00	1609801044 Label 5x5mm For Terminal	WEIDMULLER B.V.
X9	DEK5/5MC	2.00	1609801044 Label 5x5mm For Terminal	WEIDMULLER B.V.
X9	DEK5/5MC	2.00	1609801044 Label 5x5mm For Terminal	WEIDMULLER B.V.
X9	ZIA1.5/3L-1S	1.00	1651980000 ZIA 1.5/3L-1S	WEIDMULLER B.V.
X9	ZIA1.5/3L-1S	1.00	1651980000 ZIA 1.5/3L-1S	WEIDMULLER B.V.
X9	ZIA1.5/3L-1S	1.00	1651980000 ZIA 1.5/3L-1S	WEIDMULLER B.V.
X9	ZIA1.5/3L-1S	1.00	1651980000 ZIA 1.5/3L-1S	WEIDMULLER B.V.
X9	ZIA1.5/3L-1S	1.00	1651980000 ZIA 1.5/3L-1S	WEIDMULLER B.V.
X9	ZVL1.5BL	1.00	1650360000 ZVL1.5BL	WEIDMULLER B.V.

elsto Drives & Controls | Stokvis Group
Cornelius Claeslaan 1
2215 BV Voorhout
Tel. +31 (0)88 7865800
Fax. +31 (0)88 7865899
www.elsto.eu

Drawingnr.:	Projectname: MicroDOT rev3.1	Drawn:	
Ordernr.:	Projectnr. Customer:	Mat. List	Page: 7 / From: 12
Date: 29/10/2018	Date revision:	Detail:	

Material-Detail

Comp	Type	Quantity	Description	Manufacturer
X9	ZVL1.5BL	1.00	1650360000 ZVL1.5BL	WEIDMULLER B.V.
X9	ZVL1.5BL	1.00	1650360000 ZVL1.5BL	WEIDMULLER B.V.
X9	ZVL1.5BL	1.00	1650360000 ZVL1.5BL	WEIDMULLER B.V.
X9	ZVL1.5BL	1.00	1650360000 ZVL1.5BL	WEIDMULLER B.V.
X9	ZVL1.5BR	1.00	1650370000 ZVL1.5BR	WEIDMULLER B.V.
X9	ZVL1.5BR	1.00	1650370000 ZVL1.5BR	WEIDMULLER B.V.
X9	ZVL1.5BR	1.00	1650370000 ZVL1.5BR	WEIDMULLER B.V.
X9	ZVL1.5BR	1.00	1650370000 ZVL1.5BR	WEIDMULLER B.V.
X9	ZVL1.5BR	1.00	1650370000 ZVL1.5BR	WEIDMULLER B.V.
X10	DEK5/5MC	4.00	1609801044 Label 5x5mm For Terminal	WEIDMULLER B.V.
X10	ZDU2.5	4.00	1608510000 ZDU 2.5/E	WEIDMULLER B.V.
X12	DEK5/5MC	1.00	1609801044 Label 5x5mm For Terminal	WEIDMULLER B.V.
X12	ZPE2.5	1.00	1608640000 ZPE 2.5	WEIDMULLER B.V.
XCA2	NSYSPF16200	1.00	Pedestal Front Plinth 200mm For 1600	Schneider Electric
XCA2	NSYSPS42200	1.00	Pedestal 2 Plinth Side Panels 200x400	Schneider Electric
XCC1	NSYSM18164020P	1.00	Floor Mounted Cabinet 1800 x 1600 x 400 With Mountingplate	Schneider Electric
XCC1	TEMBJ16-200	2.00	Groundlearch 16mm² - 200mm² 449017	Erico
XCM13	M20736	1.00	CEE Plug IP67 3P+N+PE 63A 400V Male	Scame
XCM14	M22746	1.00	CEE Connectionplug IP67 3P+PE+N 125A 400V Female	Scame
XCM15	M22736	1.00	CEE Connectionplug IP67 3P+PE+N 63A 400V Female	Scame
1F1	ESG8/17MC	1.00	1674740000 Label 8x17mm For Relais ETC.	WEIDMULLER B.V.
1F1	GV3L40	1.00	Magnetic Circuit Breaker EverLink 40A Turn Knob	Schneider Electric
1F1	GV7AC021	2.00	clip-on connector - up to 150 A - 1.5...95 mm2	Schneider Electric
1F2	ESG8/17MC	1.00	1674740000 Label 8x17mm For Relais ETC.	WEIDMULLER B.V.
1F2	GV2L22	1.00	Magnetic Circuit Breaker 25A Turn Knob	Schneider Electric
1F2	GV7AC021	2.00	clip-on connector - up to 150 A - 1.5...95 mm2	Schneider Electric
1F3	ESG8/17MC	1.00	1674740000 Label 8x17mm For Relais ETC.	WEIDMULLER B.V.
1F3	GV2L22	1.00	Magnetic Circuit Breaker 25A Turn Knob	Schneider Electric
1F3	GV7AC021	2.00	clip-on connector - up to 150 A - 1.5...95 mm2	Schneider Electric
1F4	ESG8/17MC	1.00	1674740000 Label 8x17mm For Relais ETC.	WEIDMULLER B.V.
1F4	GV2L22	1.00	Magnetic Circuit Breaker 25A Turn Knob	Schneider Electric

elsto Drives & Controls | Stokvis Group
Cornelius Claeslaan 1
2215 BV Voorhout
Tel. +31 (0)88 7865800
Fax. +31 (0)88 7865899
www.elsto.eu

Drawingnr.:	Projectname: MicroDOT rev3.1	Drawn:	
Ordernr.:	Projectnr. Customer:	Mat. List	Page: 8 / From: 12
Date: 29/10/2018	Date revision:	Detail:	

Material-Detail

Comp	Type	Quantity	Description	Manufacturer
1F4	GV7AC021	2.00	clip-on connector - up to 150 A - 1.5...95 mm2	Schneider Electric
1F5	ESG8/17MC	1.00	1674740000 Label 8x17mm For Relais ETC.	WEIDMULLER B.V.
1F5	GV2L10	1.00	Magnetic Circuit Breaker 6,3A Turn Knob	Schneider Electric
1F5	GV7AC021	2.00	clip-on connector - up to 150 A - 1.5...95 mm2	Schneider Electric
1S1	ESG9/17K	1.00	1674760000 Label 9x17mm Adhesive For Transformer	WEIDMULLER B.V.
1S1	VBF5	1.00	Main Switch Disconnector 125A 3P	Schneider Electric
1S1	VZ13	1.00	Neutral Contact For Vario 175A V5-V6	Schneider Electric
1XCM1	24512597T	1.00	APPLIANCE INLET 3P+N+E IP66/IP67 125A 6h	Scame
1XL1	CC15/60KMC	1.00	1877310000 Label 15x60mm Adhesive	WEIDMULLER B.V.
1XL2	CC15/60KMC	1.00	1877310000 Label 15x60mm Adhesive	WEIDMULLER B.V.
2F1	ESG9/17K	1.00	1674760000 Label 9x17mm Adhesive For Transformer	WEIDMULLER B.V.
2F1	Ferrule27x60/50	1.00	Fuse 27x60, 50A	Ferraz Shawmut
2F1	US2711	1.00	UltraSafe Fuse holder with indicator (1P)	Modulostar
2F2	ESG9/17K	1.00	1674760000 Label 9x17mm Adhesive For Transformer	WEIDMULLER B.V.
2F2	Ferrule27x60/50	1.00	Fuse 27x60, 50A	Ferraz Shawmut
2F2	US2711	1.00	UltraSafe Fuse holder with indicator (1P)	Modulostar
2F3	ESG9/17K	1.00	1674760000 Label 9x17mm Adhesive For Transformer	WEIDMULLER B.V.
2F3	Ferrule27x60/25	1.00	Fuse 27x60, 25A	Ferraz Shawmut
2F3	US2711	1.00	UltraSafe Fuse holder with indicator (1P)	Modulostar
2F4	ESG9/17K	1.00	1674760000 Label 9x17mm Adhesive For Transformer	WEIDMULLER B.V.
2F4	Ferrule27x60/25	1.00	Fuse 27x60, 25A	Ferraz Shawmut
2F4	US2711	1.00	UltraSafe Fuse holder with indicator (1P)	Modulostar
2F5	ESG9/17K	1.00	1674760000 Label 9x17mm Adhesive For Transformer	WEIDMULLER B.V.
2F5	Ferrule27x60/25	1.00	Fuse 27x60, 25A	Ferraz Shawmut
2F5	US2711	1.00	UltraSafe Fuse holder with indicator (1P)	Modulostar
2F6	ESG9/17K	1.00	1674760000 Label 9x17mm Adhesive For Transformer	WEIDMULLER B.V.
2F6	Ferrule27x60/25	1.00	Fuse 27x60, 25A	Ferraz Shawmut
2F6	US2711	1.00	UltraSafe Fuse holder with indicator (1P)	Modulostar
2F7	ESG9/17K	1.00	1674760000 Label 9x17mm Adhesive For Transformer	WEIDMULLER B.V.
2F7	Ferrule27x60/25	1.00	Fuse 27x60, 25A	Ferraz Shawmut
2F7	US2711	1.00	UltraSafe Fuse holder with indicator (1P)	Modulostar

elsto Drives & Controls | Stokvis Groep
Cornelius Claeslaan 1
2215 BV Voorhout
Tel. +31 (0)88 7865800
Fax. +31 (0)88 7865899
www.elsto.eu

Drawingnr.:	Projectname: MicroDOT rev3.1	Drawn:	
Ordernr.:	Projectnr. Customer:	Mat. List	Page: 9 / From: 12
Date: 29/10/2018	Date revision:	Detail:	

Material-Detail

Comp	Type	Quantity	Description	Manufacturer
2F8	ESG9/17K	1.00	1674760000 Label 9x17mm Adhesive For Transformer	WEIDMULLER B.V.
2F8	Ferrule27x60/25	1.00	Fuse 27x60, 25A	Ferraz Shawmut
2F8	US2711	1.00	UltraSafe Fuse holder with indicator (1P)	Modulostar
2F9	ESG9/17K	1.00	1674760000 Label 9x17mm Adhesive For Transformer	WEIDMULLER B.V.
2F9	Ferrule27x60/6.3	1.00	Fuse 27x60, 6.3A	Ferraz Shawmut
2F9	US2711	1.00	UltraSafe Fuse holder with indicator (1P)	Modulostar
2F10	ESG9/17K	1.00	1674760000 Label 9x17mm Adhesive For Transformer	WEIDMULLER B.V.
2F10	Ferrule27x60/6.3	1.00	Fuse 27x60, 6.3A	Ferraz Shawmut
2F10	US2711	1.00	UltraSafe Fuse holder with indicator (1P)	Modulostar
2F11	ESG9/17K	1.00	1674760000 Label 9x17mm Adhesive For Transformer	WEIDMULLER B.V.
2F11	Ferrule27x60/6.3	1.00	Fuse 27x60, 6.3A	Ferraz Shawmut
2F11	US2711	1.00	UltraSafe Fuse holder with indicator (1P)	Modulostar
2F12	ESG9/17K	1.00	1674760000 Label 9x17mm Adhesive For Transformer	WEIDMULLER B.V.
2F12	Ferrule27x60/6.3	1.00	Fuse 27x60, 6.3A	Ferraz Shawmut
2F12	US2711	1.00	UltraSafe Fuse holder with indicator (1P)	Modulostar
2R1	HPR-4,5	1.00	Brake Resistor 4500 Watt	HPR
2U1	179675001	1.00	I/O-Extension Module EM-IO-02	Bonfiglioli Vectron
2U1	179675207	2.00	Ethercat Module	Bonfiglioli Vectron
2U1	179675500	2.00	Operating Unit KP-500	Bonfiglioli Vectron
2U1	ACU410-25ZF	2.00	ACU410-25ZF 15,0 KW 3X400V Without Filter Framesize 4	Bonfiglioli Vectron
2U1	ESG9/17K	4.00	1674760000 Label 9x17mm Adhesive For Transformer	WEIDMULLER B.V.
2U2	179675207	1.00	Ethercat Module	Bonfiglioli Vectron
2U2	179675500	1.00	Operating Unit KP-500	Bonfiglioli Vectron
2U2	ACU410-11	1.00	ACU410-11 1,5 KW 3X400V With Intern Filter Framesize 1	Bonfiglioli Vectron
2U2	ESG9/17K	2.00	1674760000 Label 9x17mm Adhesive For Transformer	WEIDMULLER B.V.
2U3	185691030	1.00	EMI Filter for ACU401-22,23,25 FTV030A	Bonfiglioli Vectron
2U3	ESG9/17K	1.00	1674760000 Label 9x17mm Adhesive For Transformer	WEIDMULLER B.V.
2U4	184420034	1.00	Line Choke for ACU401-25 LCVT034	Bonfiglioli Vectron
3U1	179675207	1.00	Ethercat Module	Bonfiglioli Vectron
3U1	179675500	1.00	Operating Unit KP-500	Bonfiglioli Vectron
3U1	ACU410-21	1.00	ACU410-21 7,5 KW 3X400V With Intern Filter Framesize 3	Bonfiglioli Vectron

elsto Drives & Controls | Stokvis Groep
Cornelius Claeslaan 1
2215 BV Voorhout
Tel. +31 (0)88 7865800
Fax. +31 (0)88 7865899
www.elsto.eu

Drawingnr.:	Projectname: MicroDOT rev3.1	Drawn:	
Ordernr.:	Projectnr. Customer:	Mat. List	Page: 10 / From: 12
Date: 29/10/2018	Date revision:	Detail:	

Material-Detail

Comp	Type	Quantity	Description	Manufacturer
3U1	ESG9/17K	2.00	16747600000 Label 9x17mm Adhesive For Transformer	WEIDMULLER B.V.
3U2	1796752O7	1.00	Ethercat Module	Bonfiglioli Vectron
3U2	179675500	1.00	Operating Unit KP-500	Bonfiglioli Vectron
3U2	ACU410-21	1.00	ACU410-21 7,5 KW 3X400V With Intern Filter Framesize 3	Bonfiglioli Vectron
3U2	ESG9/17K	2.00	16747600000 Label 9x17mm Adhesive For Transformer	WEIDMULLER B.V.
3U3	ERD	1.00	Frequency Drive Energy Recovery Device	Lenntech
3U4	184420018	1.00	Line Choke for ACU401-21 FA LCVT018	Bonfiglioli Vectron
3U5	184420018	1.00	Line Choke for ACU401-21 FA LCVT018	Bonfiglioli Vectron
3U6	184420018	1.00	Line Choke for ACU401-21 FA LCVT018	Bonfiglioli Vectron
4K1	ESG9/17K	1.00	16747600000 Label 9x17mm Adhesive For Transformer	WEIDMULLER B.V.
4K1	XPSATR11530C	1.00	EMERGENCY STOP RELAIS	Schneider Electric
4S1	ESG9/17K	1.00	16747600000 Label 9x17mm Adhesive For Transformer	WEIDMULLER B.V.
4S1	XALK178E	1.00	Emergency Stop Control Box	Schneider Electric
4S1	ZB5AZ1025	1.00	CONNECT TERMINAL CONT NC BOD SPRING	Schneider Electric
4S1	ZBE1015	1.00	TERMINAL CONTACT NO SPRING	Schneider Electric
4S2	ESG9/17K	1.00	16747600000 Label 9x17mm Adhesive For Transformer	WEIDMULLER B.V.
4S2	SM27/18	1.00	16998600000 Label 18x27mm	WEIDMULLER B.V.
4S2	ZB5AA1	1.00	Head Pushbutton White	Schneider Electric
4S2	ZB5AZ1015	1.00	CONNECT TERMINAL CONT NO BODY SPRING	Schneider Electric
4S2	ZBZ35	1.00	LEGEND CARRIER 30X50	Schneider Electric
6W1	ZB9010	1.00	EtherCAT cable	Beckhoff
6W2	ZB9010	1.00	EtherCAT cable	Beckhoff
6W3	ZB9010	1.00	EtherCAT cable	Beckhoff
6W4	ZB9010	1.00	EtherCAT cable	Beckhoff
6W5	ZB9010	1.00	EtherCAT cable	Beckhoff
7D1	ESG9/17K	1.00	16747600000 Label 9x17mm Adhesive For Transformer	WEIDMULLER B.V.
7D1	PROECO3240W24V10A	1.00	1469540000 PRO ECO3 240W 3x400VAC 24VDC 10A	Weidmüller B.V.
7F1	D3306	1.00	Circuit Breaker 3P 6A/400VAC C-Characteristic	Kopp
7F1	ESG9/17K	1.00	16747600000 Label 9x17mm Adhesive For Transformer	WEIDMULLER B.V.
7S1	ESG9/17K	1.00	16747600000 Label 9x17mm Adhesive For Transformer	WEIDMULLER B.V.
7S1	VBD0	1.00	Main Switch Disconnector 25A 3P	Schneider Electric

elsto Drives & Controls | Stokvis Group
Cornelius Claeslaan 1
2215 BV Voorhout
Tel. +31 (0)88 7865800
Fax. +31 (0)88 7865899
www.elsto.eu

Drawingnr.:	Projectname: MicroDOT rev3.1	Drawn:	
Ordernr.:	Projectnr. Customer:	Mat. List	Page: 11 / From: 12
Date: 29/10/2018	Date revision:	Detail:	

Material-Detail

Comp	Type	Quantity	Description	Manufacturer
7XCM1	2456397T	1.00	APPLIANCE INLET 3P+N+E IP66/IP67 63A 6h	Scame
7XL1	CC15/60KMC	1.00	1877310000 Label 15x60mm Adhesive	WEIDMULLER B.V.
7XL2	CC15/60KMC	1.00	1877310000 Label 15x60mm Adhesive	WEIDMULLER B.V.
8F1	DF101	1.00	Fuse Holder 1P 32A For Fuse 10x38mm	Schneider Electric
8F1	DF2CA02	1.00	Fuse 10x38 aM 2A	Schneider Electric
8F1	ESG9/17K	1.00	16747600000 Label 9x17mm Adhesive For Transformer	WEIDMULLER B.V.
8F2	DF101	1.00	Fuse Holder 1P 32A For Fuse 10x38mm	Schneider Electric
8F2	DF2CA02	1.00	Fuse 10x38 aM 2A	Schneider Electric
8F2	ESG9/17K	1.00	16747600000 Label 9x17mm Adhesive For Transformer	WEIDMULLER B.V.
8K1	UPS 24V 20A/10A	1.00	1370050010 WM UPS 20A/10A	Weidmüller B.V.
8K2	Battery 24V 3.4Ah	1.00	1251070000 WM Battery 3.4Ah	Weidmüller B.V.
9U1	CX9020	1.00	PLC	Beckhoff
16B1	NSYCFP80	2.00	Cable Support Rail 800mm	Schneider Electric
16G1	ESG9/17K	1.00	16747600000 Label 9x17mm Adhesive For Transformer	WEIDMULLER B.V.
16G1	NSYCAG294LPF	1.00	Exit Grill 336x316mm RAL7035	Schneider Electric
16G1	NSYCVF850M230PF	1.00	Ventilator 850m³/h 230VAC RAL7035	Schneider Electric
16K1	K8AB-VS3 200-230VAC	1.00	Single-Phase Voltage Relay 230V	OMRON
16TH1	ESG9/17K	1.00	16747600000 Label 9x17mm Adhesive For Transformer	WEIDMULLER B.V.
16TH1	NSYCCOTHC	1.00	Thermostat For Heating NC	Schneider Electric
16TH2	ESG9/17K	1.00	16747600000 Label 9x17mm Adhesive For Transformer	WEIDMULLER B.V.
16TH2	NSYCCOTHO	1.00	Thermostat For Cooling NO	Schneider Electric
17F1	ESG8/17MC	1.00	16747400000 Label 8x17mm For Relais ETC.	WEIDMULLER B.V.
17F1	GV2L10	1.00	Magnetic Circuit Breaker 6,3A Turn Knob	Schneider Electric
17F1	GV7AC021	2.00	clip-on connector – up to 150 A – 1.5...95 mm2	Schneider Electric
17U1	1796752O7	1.00	Ethercat Module	Bonfiglioli Vectron
17U1	179675500	1.00	Operating Unit KP-500	Bonfiglioli Vectron
17U1	ACU410-11	1.00	ACU410-11 1,5 KW 3X400V With Intern Filter Framesize 1	Bonfiglioli Vectron
17U1	ESG9/17K	2.00	16747600000 Label 9x17mm Adhesive For Transformer	WEIDMULLER B.V.

elsto Drives & Controls | Stokvis Group
Cornelius Claeslaan 1
2215 BV Voorhout
Tel. +31 (0)88 7865800
Fax. +31 (0)88 7865899
www.elsto.eu

Drawingnr.:	Projectname: MicroDOT rev3.1	Drawn:	
Ordernr.:	Projectnr. Customer:	Mat. List	Page: 12 / From: 12
Date: 29/10/2018	Date revision:	Detail:	

Bibliography

[1] A. Ho and A. Mbistrova, "The European offshore wind industry - Key trends and statistics 2016," *Wind Europe: Brussels, Belgium*, 1 2017.

[2] T. Remy and A. Mbistrova, "Offshore wind in Europe - Key trends and statistics 2017," *Wind Europe: Brussels, Belgium*, 2 2018.

[3] J. Moccia and A. Arapogianni, *Pure power-wind energy targets for 2020 and 2030*. European Wind Energy Association, 2011.

[4] N. F. B. Diepeveen, *On the application of fluid power transmission in offshore wind turbines*. PhD thesis, Delft University of Technology, 2013.

[5] A. Jarquin Laguna, *Centralized electricity generation in offshore wind farms using hydraulic networks*. PhD thesis, Delft University of Technology, 2017.

[6] T. Burton, N. Jenkins, D. Sharpe, and E. Bossanyi, *Wind energy handbook*. John Wiley & Sons, 2011.

[7] N. Fichaux, J. Beurskens, P. Jensen, and P. Wilkes, "Design limits and solutions for very large wind turbines - a 20 MW turbine is feasible," tech. rep., UpWind, 2011.

[8] Wind Europe, "World's first offshore wind farm without subsidies to be built in the Netherlands." https://windeurope.org/newsroom/press-releases/, 3 2018. Last accessed: 16-07-2018.

[9] L. Fingersh, M. Hand, and A. Laxson, "Wind turbine design cost and scaling model," tech. rep., National Renewable Energy Laboratory (NREL), Golden, CO., 2006.

[10] W. Musial, S. Butterfield, B. Ram, *et al.*, "Energy from offshore wind," in *Offshore technology conference*, Offshore Technology Conference, 2006.

[11] F. Spinato, P. J. Tavner, G. Van Bussel, and E. Koutoulakos, "Reliability of wind turbine subassemblies," *IET Renewable Power Generation*, vol. 3, no. 4, pp. 387–401, 2009.

[12] A. Ragheb and M. Ragheb, "Wind turbine gearbox technologies," in *Nuclear & Renewable Energy Conference (INREC), 2010 1st International*, pp. 1–8, IEEE, 2010.

[13] H. E. Merritt, *Hydraulic control systems*. John Wiley & Sons, 1967.

[14] S. Salter and M. Rea, "Hydraulics for wind," in *European Wind Energy Conference, Hamburg, Germany, Oct*, pp. 22–26, 1984.

[15] J. Schmitz, N. Vatheuer, and H. Murrenhoff, "Hydrostatic drive train in wind energy plants," *RWTH Aachen University, IFAS Aachen, Germany*, 2011.

[16] C. Qin, E. Innes-Wimsatt, and E. Loth, "Hydraulic-electric hybrid wind turbines: Tower mass saving and energy storage capacity," *Renewable Energy*, vol. 99, pp. 69–79, 2016.

[17] B. Skaare, B. Hörnsten, and F. G. Nielsen, "Energy considerations for wind turbines with hydraulic transmission systems," *Proceedings of EWEA Offshore 2011*, 2011.

[18] I. Piña Rodriguez, "Hydraulic drivetrains for wind turbines: Radial piston digital machines," Master's thesis, Delft University of Technology, 2012.

[19] B. Skaare, B. Hörnsten, and F. G. Nielsen, "Modeling, simulation and control of a wind turbine with a hydraulic transmission system," *Wind Energy*, vol. 16, no. 8, pp. 1259–1276, 2013.

[20] J. Schmitz, N. Diepeveen, N. Vatheuer, and H. Murrenhoff, "Dynamic transmission response of a hydrostatic transmission measured on a test bench," in *Innovating today shaping tomorrow: Scientific proceedings of the European wind energy conference and exhibition (EWEA 2012), Copenhagen, Denmark, 16-19 April, 2012*, EWEA, 2012.

[21] M. Umaya, T. Noguchi, M. Uchida, M. Shibata, Y. Kawai, and R. Notomi, "Wind power generation-development status of offshore wind turbines," *Mitsubishi Heavy Industries Technical Review*, vol. 50, no. 3, p. 29, 2013.

[22] P. Achten, S. Eggenkamp, and H. Potma, "Swash plate oscillation in a variable displacement floating cup pump," in *13th Scandinavian International Conference on Fluid Power*, pp. 163–176, Linköping University Electronic Press, 2013.

[23] J. R. Browning, J. G. McGowan, and J. F. Manwell, "A techno-economic analysis of a proposed 1.5 MW wind turbine with a hydrostatic drive train," in *ASME 2009 3rd International Conference on Energy Sustainability collocated with the Heat Transfer and InterPACK09 Conferences*, pp. 925–933, American Society of Mechanical Engineers, 2009.

[24] "Hydrautrans BV." http://www.hydrautrans.com. Last accessed: 2017-12-05.

[25] H. Polinder, J. A. Ferreira, B. B. Jensen, A. B. Abrahamsen, K. Atallah, and R. A. McMahon, "Trends in wind turbine generator systems," *IEEE Journal of emerging and selected topics in power electronics*, vol. 1, no. 3, pp. 174–185, 2013.

[26] D. Buhagiar, T. Sant, C. Micallef, and R. N. Farrugia, "Improving the energy yield from an open loop hydraulic offshore turbine through deep sea water extraction and alternative control schemes," *Energy*, vol. 84, pp. 344–356, 2015.

[27] T. Sant and R. N. Farrugia, "Modeling the energy yield enhancement from a wind turbine at a deep offshore low wind site through combined power and thermocline energy production," *Journal of Solar Energy Engineering*, vol. 137, no. 1, p. 011002, 2015.

[28] S. P. Mulders, N. F. B. Diepeveen, and J.-W. van Wingerden, "Control design, implementation and evaluation for an in-field 500 kW wind turbine with a fixed-displacement hydraulic drivetrain," *Wind Energy Science*, 2018.

[29] D. Buhagiar, T. Sant, and M. K. Bugeja, "Control of an open-loop hydraulic offshore wind turbine using a variable-area orifice," in *ASME 2015 34th International Conference on Ocean Offshore and Arctic Engineering, St. John's*, 2015.

[30] B. Snyder and M. J. Kaiser, "Ecological and economic cost-benefit analysis of offshore wind energy," *Renewable Energy*, vol. 34, no. 6, pp. 1567–1578, 2009.

[31] P. Silva, A. Giuffrida, N. Fergnani, E. Macchi, M. Cantù, R. Suffredini, M. Schiavetti, and G. Gigliucci, "Performance prediction of a multi-mw wind turbine adopting an advanced hydrostatic transmission," *Energy*, vol. 64, pp. 450–461, 2014.

[32] A. Jarquin-Laguna, "Simulation of an offshore wind farm using fluid power for centralized electricity generation," in *Journal of Physics: Conference Series*, no. 10 in 753, IOP Publishing, 2016.

[33] E. A. Bossanyi, "The design of closed loop controllers for wind turbines," *Wind energy*, vol. 3, no. 3, pp. 149–163, 2000.

[34] J. Jonkman, S. Butterfield, W. Musial, and G. Scott, "Definition of a 5-mw reference wind turbine for offshore system development," tech. rep., National Renewable Energy Laboratory (NREL), Golden, CO., 2009.

[35] Z. Zhang, *Pelton Turbines*. Springer International Publishing, 1 ed., 2016.

[36] D. Buhagiar, T. Sant, and M. Bugeja, "A comparison of two pressure control concepts for hydraulic offshore wind turbines," *Journal of Dynamic Systems, Measurement, and Control*, vol. 138, no. 8, p. 081007, 2016.

[37] F. M. White, *Fluid Mechanics*. New York: McGraw-Hill, 7 ed., 2011.

[38] S. Bragg, "Effect of compressibility on the discharge coefficient of orifices and convergent nozzles," *Journal of Mechanical Engineering Science*, vol. 2, no. 1, pp. 35–44, 1960.

[39] F. D. Bianchi, R. J. Mantz, and H. De Battista, *The wind and wind turbines*. Springer, 2007.

[40] G. A. Van Kuik, "The Lanchester-Betz-Joukowsky limit," *Wind Energy*, vol. 10, no. 3, pp. 289–291, 2007.

[41] J. F. Manwell, J. G. McGowan, and A. L. Rogers, *Wind energy explained: theory, design and application*. John Wiley & Sons, 2 ed., 2010.

[42] M. E. Meadows and T. M. Walski, *Computer applications in hydraulic engineering*. Haestad Methods, 2001.

[43] N. Manring, *Hydraulic control systems*. John Wiley & Sons, 2005.

[44] B. Nesbitt, *Handbook of pumps and pumping: Pumping manual international*. Elsevier, 2006.

[45] W. E. Wilson, *Positive-displacement pumps and fluid motors*. Pitman Publishing Corporation, 1950.

[46] American Institute of Chemical Engineers, *Positive Displacement Pumps: A Guide to Performance Evaluation*. AIChE Equipment Testing Procedure, John Wiley & Sons, 2010.

[47] H. H. Tackett, J. A. Cripe, and G. Dyson, "Positive displacement reciprocating pump fundamentals-power and direct acting types," in *Proceedings of the twenty-fourth international pump user symposium*, pp. 45–58, 2008.

[48] P. Beater, *Entwurf hydraulischer Maschinen: Modellbildung, Stabilitätsanalyse und Simulation hydrostatischer Antriebe und Steuerungen*. Springer-Verlag, 1 ed., 1999.

[49] J. S. Cundiff, *Fluid power circuits and controls: fundamentals and applications*. CRC Press, 2001.

[50] H. Murrenhoff, *Grundlagen der Fluidtechnik: Teil 1: Hydraulik*. Reihe Fluidtechnik, Shaker Verlag, 2016.

[51] A. Akers, M. Gassman, and R. Smith, *Hydraulic power system analysis*. CRC press, 2006.

[52] R. Oldenburger and R. Goodson, "Simplification of hydraulic line dynamics by use of infinite products," *Journal of Basic Engineering*, vol. 86, no. 1, pp. 1–8, 1964.

[53] K. G. Nayar, M. H. Sharqawy, L. D. Banchik, *et al.*, "Thermophysical properties of seawater: a review and new correlations that include pressure dependence," *Desalination*, vol. 390, pp. 1–24, 2016.

[54] L. F. Moody, "Friction factors for pipe flow," *Trans. Asme*, vol. 66, pp. 671–684, 1944.

[55] S. E. Haaland, "Simple and explicit formulas for the friction factor in turbulent pipe flow," *Journal of Fluids Engineering*, vol. 105, no. 1, pp. 89–90, 1983.

[56] S. Genić, I. Aranđelović, P. Kolendić, M. Jarić, N. Budimir, and V. Genić, "A review of explicit approximations of colebrook's equation," *FME transactions*, vol. 39, no. 2, pp. 67–71, 2011.

[57] G. Falkovich, *Fluid Mechanics: A Short Course for Physicists*. Cambridge University Press, 2011.

[58] S. L. Dixon and C. Hall, *Fluid mechanics and thermodynamics of turbomachinery*. Butterworth-Heinemann, 4 ed., 2013.

[59] A. E. Fitzgerald, C. Kingsley, S. D. Umans, and B. James, *Electric machinery*, vol. 5. McGraw-Hill New York, 2003.

[60] S. W. Fardo and D. R. Patrick, *Electrical power systems technology*. The Fairmont Press, Inc., 2009.

[61] E. Hau, *Wind turbines: fundamentals, technologies, application, economics*. Springer Science & Business Media, 2013.

[62] E. J. N. Menezes, A. M. Araújo, and N. S. B. da Silva, "A review on wind turbine control and its associated methods," *Journal of Cleaner Production*, vol. 174, pp. 945–953, 2018.

[63] J. Slootweg, S. De Haan, H. Polinder, and W. Kling, "General model for representing variable speed wind turbines in power system dynamics simulations," *IEEE Transactions on power systems*, vol. 18, no. 1, pp. 144–151, 2003.

[64] L. Y. Pao and K. E. Johnson, "A tutorial on the dynamics and control of wind turbines and wind farms," in *American Control Conference, 2009. ACC'09.*, pp. 2076–2089, IEEE, 2009.

[65] I. Munteanu, A. I. Bratcu, N.-A. Cutululis, and E. Ceanga, *Optimal control of wind energy systems: towards a global approach*. Springer Science & Business Media, 2008.

[66] "NoordzeeWind." http://www.noordzeewind.nl/kennis/rapporten-data/. Last accessed: 2019-01-04.

[67] H. Kouwenhoven, "User manual data files meteorological mast noordzeewind," *Document code: NZW-16-S-4-R03, Date*, vol. 1, 2007.

[68] J. Wagenaar and P. Eecen, "3D Turbulence at the offshore wind farm Egmond aan Zee," *ECN Wind Energy*, 2010.

[69] M. N. Soltani, T. Knudsen, M. Svenstrup, R. Wisniewski, P. Brath, R. Ortega, and K. Johnson, "Estimation of rotor effective wind speed: A comparison," *IEEE Transactions on Control Systems Technology*, vol. 21, no. 4, pp. 1155–1167, 2013.

[70] D. Schlipf, D. J. Schlipf, and M. Kühn, "Nonlinear model predictive control of wind turbines using lidar," *Wind energy*, vol. 16, no. 7, pp. 1107–1129, 2013.

[71] D. A. Smith and M. Harris, "Wind turbine control having a lidar wind speed measurement apparatus," Oct. 2007. US Patent 7,281,891.

[72] M. Vali, V. Petrović, G. Steinfeld, L. Pao, and M. Kühn, "Large-eddy simulation study of wind farm active power control with a coordinated load distribution," in *Journal of Physics: Conference Series*, vol. 1037, p. 032018, IOP Publishing, 2018.

[73] B. Maronga, M. Gryschka, R. Heinze, F. Hoffmann, F. Kanani-Sühring, M. Keck, K. Ketelsen, M. O. Letzel, M. Sühring, and S. Raasch, "The parallelized large-eddy simulation model (palm) version 4.0 for atmospheric and oceanic flows: model formulation, recent developments, and future perspectives," *Geoscientific Model Development Discussions 8 (2015), Nr. 2, S. 1539-1637*, 2015.

[74] MathWorks Benelux, "Simscape Fluids Documentation." https://nl.mathworks.com/help/physmod/hydro/index.html, 2019. Last accessed: 02-04-2019.

[75] K. J. Aström and R. M. Murray, *Feedback systems: an introduction for scientists and engineers*. Princeton University Press, 2008.

[76] G. F. Franklin, J. D. Powell, and A. Emami-Naeini, "Feedback control of dynamics systems," *Addison-Wesley, Reading, MA*, 1994.

[77] L. Freris and D. Infield, *Renewable energy in power systems*. John Wiley & Sons, 2008.

[78] D. Michailidis and N. Diepeveen, "Conceptual design of a DOT farm generator station," in *Proceedings of the EWEA Offshore 2011 Conference, Amsterdam, The Netherlands, 29 November-1 December 2011*, European Wind Energy Association, 2011.

[79] Z. Zhang, "Flow friction theorem of Pelton turbine hydraulics," *Proceedings of the Institution of Mechanical Engineers, Part A: Journal of Power and Energy*, vol. 221, no. 8, pp. 1173–1180, 2007.

[80] KTR Systems GmbH, "Drive technology." Product catalogue, 2019.

[81] R. Gasch and J. Twele, *Wind power plants: fundamentals, design, construction and operation*. Springer Science & Business Media, 2 ed., 2011.

[82] R. J. Marks II, *Handbook of Fourier analysis & its applications*. Oxford University Press, 2009.

[83] M. Verhaegen and V. Verdult, *Filtering and system identification: a least squares approach*. Cambridge University Press, 2007.

[84] MathWorks Benelux, "System Identification Toolbox Documentation." https://nl.mathworks.com/help/ident/index.html, 2019. Last accessed: 02-04-2019.

[85] S. Boersma, B. Doekemeijer, P. Gebraad, P. Fleming, J. Annoni, A. Scholbrock, J. Frederik, and J. van Wingerden, "A tutorial on control-oriented modeling and control of wind farms," in *American Control Conference (ACC), 2017*, pp. 1–18, IEEE, 2017.

Glossary

List of Acronyms

AC	alternating current
DOT	Delft Offshore Turbine
ESC	Extremum Seeking Control
FFT	Fast Fourier Transform
LCOE	Levelized Cost of Energy
LIDAR	Light Detection And Ranging of Laser Imaging Detection And Ranging
LPV	Linear Parameter Varying
MPPT	Maximum Power Point Tracking
NREL	National Renewable Energy Laboratory
OWEZ	Offshore Windpark Egmond aan Zee
OTEC	Ocean Thermal Energy Conversion
PLC	Programmable Logic Controller
PCD	Pitch Circle Diameter
PALM	Parallelized Large-eddy simulation Model
RO	Reverse Osmosis
TRL	Technology Readiness Level
TSR	Tip Speed Ratio
UPS	Uninterruptible Power Supply
VFD	Variable Frequency Drive